Modeling of ECC Materials using Numerical Formulations based on Plasticity

Dick-Nielsen, Lars; Stang, Henrik; Poulsen, Peter Noe; Li, Victor C.

Publication date:
2008

Document Version
Publisher's PDF, also known as Version of record

Citation (APA):
Dick-Nielsen, L., Stang, H., Poulsen, P. N., & Li, V. C. (2008). Modeling of ECC Materials using Numerical Formulations based on Plasticity.

Technical University of Denmark DTU

Lars Dick-Nielsen

Modeling of ECC Materials using Numerical Formulations based on Plasticity

DTU Civil Engineering
Department of Civil Engineering

PHD THESIS

Modeling of ECC Materials using Numerical Formulations based on Plasticity

Lars Dick-Nielsen

Ph.D. Thesis

Department of Civil Engineering
Technical University of Denmark

2008

Modeling of ECC Materials
using Numerical Formulations
based on Plasticity

Printed by DTU Tryk
Department of Civil Engineering
Technical University of Denmark
978-87-7877-243-5
1601-2917

Preface

This thesis is submitted as a partial fulfilment of the requirements for the Danish Ph.d. degree. The first part introduces the research field and highlights the major findings and conclusions. The second part is a collection of five papers, presenting the research in greater detail.

Lyngby the 1st of October 2007

Lars Dick-Nielsen

Preface to published version of thesis

The thesis was defended at a public defence on Friday the 18th of January 2008. Official opponents were Senior Scientist Bent F. Sørensen, Risø DTU, Professor Milan Jirásek, the Technical University of Prague, and Professor Christopher K. Y. Leung, the Hong Kong University of Science and Technology. Subsequently the Ph.D. degree was awarded from the Technical University of Denmark.

Compared to the original submitted version of the thesis a number of minor editorial corrections have been implemented and the status of one of the papers on which the thesis is based has changed from accepted to published.

Lyngby the 1st of October 2008

Lars Dick-Nielsen

Acknowledgements

I gratefully acknowledge the support and fruitful discussion with my supervising team; Professor Henrik Stang, associate professor Peter Noe Poulsen and professor Victor C. Li, Henrik and Peter both from the Department of Civil Engineering, Section for Structural Engineering at the Technical University of Denmark and Victor from the Department of Civil and Environmental Engineering at the University of Michigan, USA.

Furthermore I would like to thank John Forbes Olesen and Leif-Otto Nielsen both associate professors at the Department of Civil Engineering, at the Technical University of Denmark. Although they were not a part of the supervisor team they were available for discussions and good advice.

I really appreciate the hospitality shown to me during my stay abroad by Petr Kabele, associate professor at the Technical University of Prague and Sarah Billington, associate professor at Stanford University. They both showed a large interest in my research and we had some fruitful discussions. In that respect I would like to thank the following foundations for financial support making my stay abroad possible: The Larsen and Nielsen Foundation, The Poul V. Andersens Foundation, The Knud Højgaard Foundation, The Alexandre and Nina Haynman Foundation, The Otto Mønsted Foundation and the BYG-DTU Travel Foundation for PhD-students.

Finally I want to thank Ph.D Jesper Asferg and Ph.D. Rasmus Walter for the discussions we had concerning fracture mechanics and Finite Element computations. I would like to thank them and the rest of the Ph.D.-office for the good times I have had during my Ph.D.-study.

Abstract

Engineered Cementitious Composite (ECC), is a high performance fiber-reinforced cementitious composite. In contrast to conventional Fiber-Reinforced Concrete (FRC), ECC is characterized by its enhanced ability to undergo strain-hardening in tension. Since the introduction of ECC less than two decades ago a large amount of research has been conducted on ECC and it has been used for some large field applications. To extend the use of the material, special attention has to be given to a number of areas: the material characteristics found in laboratories has to be recreated on construction sites, the test methods should be standardized and more advanced material models are needed to utilize the special characteristic of the ECC-material.

In the present thesis a material model for ECC is derived, and implemented in a Finite Element Method (FEM) program. The model differs from existing models by combining a matrix and a fiber description to describe the behavior of the ECC-material. Using this formulation the model is able to provide information about crack orientation, opening and spacing, which is important knowledge in the multiple cracking state. The model is based on the smeared fixed, multiple cracking approach and the matrix crack is described using a plasticity damage mechanics model. The model is able to capture the dilation effect that will appear during mode II crack opening. In the thesis the model has been tested on both the material scale and the construction scale.

To derive the material model a multi scale, approach was employed. On each length scale important phenomena were investigated using numerical and analytical calculations. The mechanisms found on the small scales were then incorporated in the models on the larger scales.

On the micro scale, it was examined whether the ECC matrix was adequately described using Linear Elastic Fracture Mechanics (LEFM) or whether a cohesive approach was more appropriate. The ECC matrix is a cementitious material with small aggregate and such materials are often described using LEFM. The investigation showed that even for such brittle materials the cohesive zone was long enough to eliminate the use of LEFM. Using the cohesive approach more realistic first crack strengths could be predicted and the sensitivity toward the size of initial defects diminished.

On the meso scale numerical simulations have been used to shed light on whether or

not the existing criteria are adequate to achieve multiple cracking. Special attention was given to the steady-state, flat-crack propagation criterion. In contrast to what is stated in this criterion, it was found that the complimentary energy of the fiber-bridging curve only had little influence on the crack propagation The investigation showed that steady-state, flat-crack propagation did not occur for crack length in the investigated range up to 400 mm, when a cohesive approach was employed. Furthermore it was shown that the cracks would propagate with small crack openings, 20 μm, whether the criterion was fulfilled or not.

On the macro scale a plasticity-based damage mechanics model for ECC is derived and implemented in a finite element method program. The present model differs from existing models by combining a matrix crack and fiber bridging description to describe the behavior of the ECC-material. The model provides information about crack opening, orientation and spacing, which makes it possible to assess the condition of a structure. A simple simulation is performed on the material level to demonstrate the capability of the model. Furthermore simulations of a four point bending beam and an infill panel are performed.

Resumé

Engineered Cementitious Composite (ECC) er et fiber armeret cementbaseret komposit materiale. I modsætning til konventionelt fiber armeret beton er ECC karakteriseret ved sine forbedrede egenskaber til at udvise tøjnings-hærdning under træk. Siden ECC blev introduceret for mindre end to årtier siden, er der blev udført meget forskning inden for dette område og ECC er også blevet brugt til et mindre antal store konstruktioner. For at udbrede brugen af dette materiale skal der visse forbedringer til: de materialeegenskaber som kan frembringes i et laboratorium, skal ligeledes kunne genfindes på en byggeplads, der skal opstilles standard test metoder for at bestemme materiale egenskaberne og der er brug for mere avancerede materialemodeller, så de specielle egenskaber for ECC-materialet kan udnyttes.

I denne afhandling er der udledt en materialemodel for ECC og modellen er blevet implementeret i et *Finite Element Method* (FEM) program. Modellen adskiller sig fra eksisterende modeller ved at kombinere en matrix model og en fiber model. Denne formulering gør det muligt at få informationer om revneorientering, -åbning og -afstand. Disse informationer er vigtige at have, når der skal dimensioneres i den tilstand, hvor revnerne dannes og udbreddes. Modellen er baseret på *smeared crack*-teorien og revneubdreddelsen i matricen er modelleret ved brug af en plasticitets model indeholdende skadesparametre. Modellen er i stand til at beskrive den åbning, der forekommer i en revne når revnefladerne forskydes under tryk. I afhandlingen er modellen testet på både materialeniveau og på konstruktionsniveau.

For at udlede materialemodellen er der udført undersøgelser på mikro-, meso- og makroniveau. På disse niveauer er ECC-egenskaberne beskrevet vha. numeriske og analytiske beregninger. De egenskaber der findes på lavere niveauer bliver implementeret i modellerne på de højere niveauer.

På mikroniveauet blev det undersøgt om ECC matricen bedst blev beskrevet vha. linear elastisk brudmekanik (LEFM) eller om en kohæsiv teori beskriver matricen bedre. ECC matricen er cementbaseret og de brugte tilslag er relativt små. Opførslen af sådanne materialer beskrives ofte vha. LEFM. Undersøgelsen viste at selv for et sprødt materiale som ECC-matricen, var den kohæsive zone stor nok til at udelukke brugen af LEFM. Brugen af den kohæsive teori medførte at mere realistiske materiale styrker blev fundet og følsomheden overfor størrelsen af defekter i matricen blev mindre.

På mesoniveauet er de eksisterende kriterier for multipel revnevækst blevet testet vha. numeriske simuleringer. I undersøgelsen er der specielt lagt vægt på at teste gyldigheden af kriteriet, der medfører revneudbredelse under konstant revneåbning. Denne undersøgelse viste, at den komplementære energi af fiberkurven kun havde lille indflydelse på revne udbredelsen, i modsætning til, hvad er påstået i dette kriterium. Undersøgelsen yderligere viste, at når den kohæsive teori blev benyttet, blev konstant revneåbning under revneudbredelse ikke opnået for revnelænger op til 400 mm. Yderligere blev det vist, at revner i ECC-matricen vil udbrede sig med en lille revneåbning, 20 μm, uafhængigt af om kriteriet for konstant revneåbning var opfyldt.

På macroniveauet er en plasticitet-baseret skades mekanisk model for ECC blevet udledt og implementeret i et FEM-program. Denne model udskiller sig fra eksisterende modeller ved at kombinere en model for revneudbreddelse i ECC-matricen og fiber-*bridging*. Modellen giver informationer om revneåbning, -orientering og -afstand. Disse oplysninger gør det muligt at vurdere tilstanden af en konstruktion udført af ECC. For at demonstrere, hvad modellen kan, er der i afhandling udført en simulering af udbreddelsen af en enkelt revne. Derudover udføres simuleringer af en fire punkts bøjnings bjælke og af et panel.

Table of Contents

II Appended Papers

Paper I Semi-analytical cohesive crack model for the analysis of first crack strength of mortar,
In: *Proceedings of the 17th Nordic Seminar on Computational Mechanics, Sweden, 2004*
A. Eriksson, J. Månsson and G. Tibert (eds), page 183-186

Paper II Micro-mechanical Analysis of Fiber Reinforced Cementitious Composites using Cohesive Crack Modeling,
In: *Journal of Advanced Concrete Technology 2007*, Volume 5, Number 3, page 373-382.

Paper III Conditions for Strain-Hardening in ECC Uniaxial Test Specimens,
Submitted to: *Journal of Engineering Mechanics*

Paper IV A Plastic Damage Mechanics Model for Strain-Hardening Fiber-Reinforced Cementitious Composite, Part I: Theory
Submitted to: *Journal of Engineering Mechanics*

Paper V A Plastic Damage Mechanics Model for Strain-Hardening Fiber-Reinforced Cementitious Composite, Part II: Simulations
Submitted to: *Journal of Engineering Mechanics*

Additional work (not included in the thesis)

[1] Dick-Nielsen L., Stang H. and Poulsen P. N.: Micro-mechanical Analysis of Fiber Reinforced Cementitious Composites using Cohesive Crack Modeling, In proceedings: *Knud Højgaard Conference on Advanced Cement-Based Materials, Lyngby, Denmark, O.M. Jensen, M. Geiker and H. Stang (eds), 2005*, page 277-292.

[2] Stang H., Olesen J. F., Poulsen P. N. and Dick-Nielsen L.: On the Application of Cohesive Crack Modeling in Cementitious Materials, In proceedings: *Knud Højgaard Conference on Advanced Cement-Based Materials, Lyngby, Denmark, O.M. Jensen, M. Geiker and H. Stang (eds), 2005*, page 265-275.

[3] Dick-Nielsen L., Stang H. and Poulsen P. N.: Condition for Strain-hardening in ECC Uniaxial Test Specimen, In proceedings: *Measuring, Monitoring and Modeling Concrete Properties, Alexandroupolis, Greece, M. S. Konsta-Gdoutos (eds), 2006*, page 41-47.

[4] Dick-Nielsen L., Stang H. and Poulsen P. N.: Simulation of strain-hardening in ECC uniaxial test specimen by use of a damage mechanics formulation, In proceedings: *EURO-C 2006 Computational Modelling of Concrete Structures, Mayrhofen , Austria , G. Meschke, R D. Borst, H. Mang and N. Bicanic (eds), 2006*, page 319-328.

[5] Stang H., Olesen J. F., Poulsen P. N. and Dick-Nielsen L.: Application of the cohesive crack in cementitious material modelling, In proceedings: *EURO-C 2006 Computational Modelling of Concrete Structures, Mayrhofen , Austria , G. Meschke, R D. Borst, H. Mang and N. Bicanic (eds), 2006*, page 443-449.

[6] Dick-Nielsen L., Stang H. and Poulsen P. N.:
Modeling of ECC materials using numerical formulations based on plasticity,
In proceedings: *6th International PhD Symposium in Civil Engineering,*
Zurich , Switzerland , T. Vogel, N. Mojsilovic and P. Marti (eds),
2006, page 44-45. Full paper on CD.

[7] Stang. H, Dick-Nielsen L., Poulsen P. N. and Olesen J. F.:
Recent Developments in the modeling of matrix crack propagation in
brittle matrix composites,
In proceedings: *The 8th International Symposion on Brittle Matrix Composites,*
Warsaw , Poland , Woodhead Publishing Limited, Cambridge (pub),
2006, page 221-238.

[8] Stang H., Olesen J. F., Poulsen P. N. and Dick-Nielsen L.:
On the Application of Cohesive Crack Modeling in Cementitious Materials,
In: *Materials and Structures,*
2007, (40) page 365-374.

[9] Dick-Nielsen L., Stang H., Poulsen P. N. and Kabele P.:
A Plastic Damage Mechanics Model for Engineered Cementitious Composites,
In proceedings: *FraMCos-6: 6th International Conference on*
Fracture Mechanics of Concrete and Concrete Structures,
Book title: High-Performance Concrete, Brick-Masonry and
Environmental Aspects,
Catania , Italy , A. Carpinteri, P. Gambarova, G. Ferro and G. Plizzari (eds),
2007, page 1449-1456

[10] Fischer G., Stang H. and Dick-Nielsen L.:
Initiation and Development of Cracking in ECC materials:
Experimental Observations and Modeling,
In proceedings: *FraMCos-6: 6th International Conference on*
Fracture Mechanics of Concrete and Concrete Structures,
Book title: High-Performance Concrete, Brick-Masonry and
Environmental Aspects,
Catania , Italy , A. Carpinteri, P. Gambarova, G. Ferro and G. Plizzari (eds),
2007, page 1517-1522.

Part I

Introduction and Summary

Chapter 1

Introduction

1.1 Engineered Cementitious Composite

Fiber-reinforced cementitious materials are often classified based on their mechanical behavior when subjected to uniaxial tension, where a distinction is made between materials that exhibit tension-softening and strain-hardening (Stang 1992) and (Naaman & Reinhardt 1996). The distinction is based on the predominant behavior, since all tension-softening materials will undergo some degree of strain-hardening before softening takes over (van Mier 2004) and strain-hardening materials will eventually exhibit softening (Naaman & Reinhardt 1996), the latter materials are often named Strain-Hardening Fiber-Reinforced Cementitious Composites (SHFRCC). Strain-hardening is associated with the formation of multiple cracks, while only a few cracks will appear in tension-softening material under uniaxial tension, see figure 1.1. The two types of material behavior have a significant influence on the structural behavior of a construction (Li 2003) and (Walter, Olesen, Stang & Vejrum 2007), where strain-hardening materials often have proven superior. The two types of material behavior also have an influence on how the characteristics of the materials are best modeled. In the case of a tension-softening material a fracture mechanical approach describing the behavior of each crack is often employed, while the ductility of the strain-hardening materials often makes the use of a continuum model more suitable.

Engineered Cementitious Composite (ECC), is a high performance fiber-reinforced cementitious composite and a member of the SHFRCC family. The ECC-material is characterized by its enhanced ability to undergo strain-hardening in tension. The ECC-matrix consists of cement-paste with very fine aggregates. When the matrix is combined with the right kind of synthetic or steel fibers a highly ductile material is achieved. The ductility of ECC is illustrated in figure 1.2(a), where an ECC-plate is subjected to a four point bending (FPB) test. Among the components the fibers are typically the most expensive. It is therefore important to create a mix containing a low amount of fibers, which still

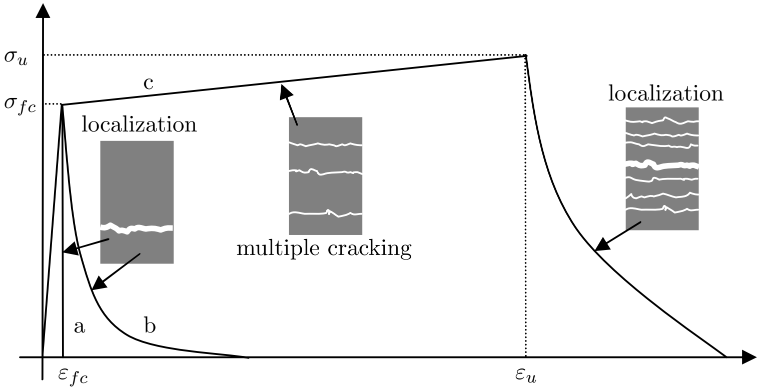

Figure 1.1 *Classification based on mechanical behavior: a) regular concrete, b) tension-softening (conventional FRC) and c) strain-hardening (SHFRCC). After (Kabele 2000).*

undergoes strain-hardening. Often 2 percent by volume of Polyvinyl alcohol (PVA) fibers with a diameter of 40 μm and a length of 8-12 mm are employed (Li 2003). Although the fiber volume concentration is low the cost of fibers in PVA-ECC still makes up approximately 50 % of the material cost. The amount of fibers is also limited by the rheological properties of the ECC-material during mixing and casting. If too high a fiber volume percent is chosen, the fibers will gather in bundles and the material loses its workability and strain-hardening capacity.

Conceptually, the ECC-matrix is assumed to contain initial flaws, which are distributed randomly over the volume. However the physical nature of these initial flaws, whether they are pores, micro-cracks or combination of both, are not generally agreed upon. When the material is loaded in tension, micro-cracks are initiated from the initial flaws due to stress concentrations around the flaws. In figure 1.3 the relationship between normal strain, normal stress and average crack opening for a specimen subjected to uniaxial tension is illustrated. The first crack initiates in a weak plane as the tensile strength of this plane is reached. This crack is then bridged by fibers, allowing the stress to be carried across the crack and back into the matrix. As the crack opens an increasing load is carried by the fibers and a new crack is initiated in an adjacent weak plane. This mechanism continues until the load carrying capacity of the fibers is reached in one of the cracks. The state where no new cracks will initiate is referred to as the saturated state. As shown in figure 1.3 the formation of new cracks under increasing normal strain leads to an almost constant average crack opening. Without the use of rebars the crack openings in PVA-ECC in the strain-hardening phase will be in the range of 60-80 μm (Wang & Li 2006) or 100-200 μm (Fischer, Stang & Dick-Nielsen 2007). The cracks in the saturated state can have spacings down to approximately 2 mm as shown in figure 1.2(b). If the strain is increased further, localization will occur in the crack where the load carrying capacity of

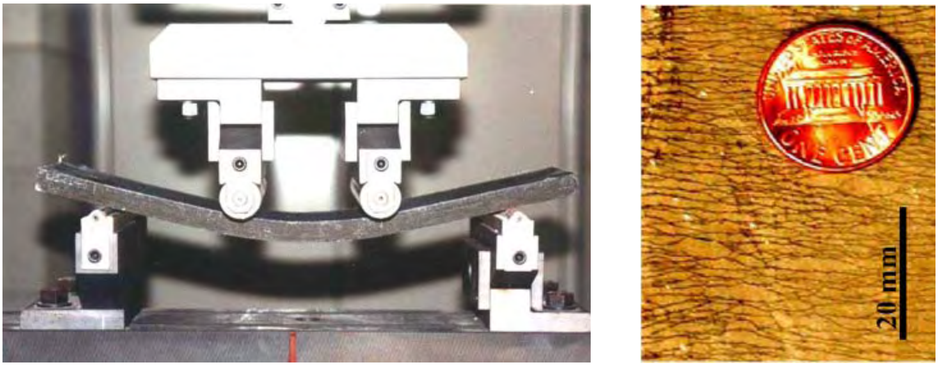

(a) FPB test of ECC-plate (www.engineeredcomposites.com).

(b) Multiple cracks in ECC-specimen (Li & Wang 2005).

Figure 1.2 *Characteristics of the ECC-material.*

the fibers is reached and the material will exhibit a softening behavior.

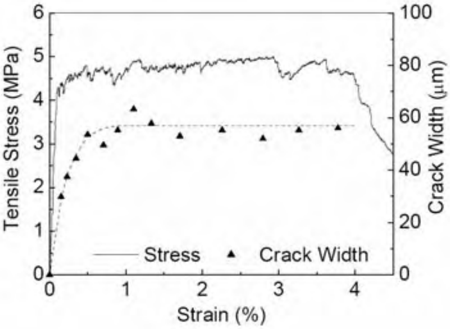

Figure 1.3 *Relationship between normal strain, normal stress and average crack opening for PVA-ECC (Wang & Li 2006).*

1.2 Test Methods and Applications

Only a few design-guidelines and standardized tests exist for the ECC-material at the present time. This increases the responsibility of the design-engineers and makes most engineers reluctant to use the material. Attempts to develop standardized tests have indicated that several important material characteristics are dependent on specimen geometry and test method (Kanakubo, Shimizu, Katagiri, Kanda, Fukuyama & Rokugo 2006) and

(Mechtcherine & Schulze 2006). This dependance can partly be explained by fiber distribution and orientation. Fibers in a thin specimen will be orientated primarily in two dimensions in contrast to fibers in a thick specimen, which will be orientated in three dimensions. The two dimensional fiber orientation gives rise to a higher degree of strain-hardening, because a higher number of fibers will then bridge the cracks. The preferred test method should therefore reflect the structural use of the material. To set up design-guidelines for the use of strain-hardening cement based materials, a committee under RILEM was formed in 2005 and will give their recommendations in 2008.

The ECC-material is not meant as a replacement for regular concrete, due to the high cost of fibers. The ECC-material should be employed in constructions, where controlled crack growth can enhance the resistance against spalling and corrosion of rebars and where the enhanced ductility can be utilized. A large marked for the ECC-material is the infrastructure in areas with seismic activity. In 1995 Kobe, Japan was the center of a major earthquake with more than 5,500 people killed and 26,000 wounded. The economic loss has been estimated at about $ 147 billion (EQE International 1995). The use of the ECC-material is not limited to infrastructure in areas with seismic activity, as the dynamic load from the traffic induces similar problems. In 2005 ASCE estimated that $ 1.6 trillion was needed over a five-year period in order to bring the nation's infrastructure to a viable condition (ASCE 2005), and the maintenance of infrastructure is not a problem confined to USA. This creates an economical incentive to develop materials that can perform well under dynamic loading. Tests performed by Fischer & Li (2002) showed that constructions made from the ECC-material performed better than constructions made from regular reinforced concrete under dynamic load. In these experiments the regular concrete beams were exposed to serious spalling, while this was prevented in the ECC-beams. The tests also showed that the ECC-beams performed well without the use of shear-reinforcement. The ECC-material can also be used in the construction of pipelines, where a special extruding technic (Stang & Li 1999) makes the ECC-material competitive with plastic.

ECC has all ready been used for large field applications, although it is a relatively new material. The Mihara Bridge in Hokkaido, Japan, is a cable-stayed bridge which opened for traffic in 2005 (see figure 1.4(a)). Here ECC was used to construct a composites steel/ECC bridge deck, where the layer of ECC is only 5 cm thick. Thanks to the characteristics of the material it has contributed to a 40 % reduction in weight compared to a regular concrete construction.

There are several examples of the ECC-materials being used to retrofit existing constructions. In 2003 the material was used in the repair work of the Mitaka Dam in Hiroshima-Prefecture (see figure 1.4(b)). The 60 years old dam suffered from cracks and spalling. Here a 20 mm thick ECC-cover was sprayed on the surface covering an area of 600 m^2. The ECC-material has also been suggested for use in the retrofitting of existing steel bridges that suffer from fatigue damage due to increasing traffic volumes and higher wheel loads. Walter et al. (2007) investigated the possibility of strengthening of an existing bridge deck by applying an ECC-layer on the deck to increase the stiffness.

(a) Mihara. (b) Mitaka.

Figure 1.4 *Field applications (from www.engineeredcomposites.com).*

Furthermore the ECC-material can been used to construct jointless bridge decks (Kim, Fischer & Li 2004). Thanks to the ductile behavior of the ECC-material an ECC link slab is able to absorb deformations in the longitudinal direction as well as deformation due to bending of the bridge and the service life of the deck can therefore be extended.

1.3 Design and Modeling of Engineered Cementitious Composite

Cement, mortar and concrete are usually characterized as brittle or quasi-brittle materials. For the last 40 years a debate has existed as to how modeling of these materials is best performed. A broad view of the employed fracture mechanical models from this period is given by Karihaloo (1995). By now it is generally agreed upon that the *Fictitious Crack Model* (FCM) attributed to Hillerborg, Modeer & Petersson (1976) best captures the material characteristics of concrete. To what extend FCM can be applied to cement and mortar however is still under debate, and Linear Elastic Fracture Mechanics (LEFM) is often used for the modeling of these brittle materials. The fictitious crack model differs from the cohesive crack model of Barenblatt (1962) and Dugdale (1960) by having the cohesive stress which bridges the cracks depending on the crack opening. In the cohesive models by Hillerborg et al. (1976), Barenblatt (1962) and Dugdale (1960) the cohesive stresses insure a smooth crack closure, and thanks to this there is no energy dissipation at the crack tip. When implementing the FCM in FEM codes smooth crack closure is not necessarily insured thanks to discretization errors, however as shown by Stang, Olesen, Poulsen & Dick-Nielsen (2007) this has little influence on the results. The FCM was originally developed for mode I cracks only, but it can be extended to mode II and mixed mode crack propagation. However the propagation of cracks under mixed mode is a research area that is currently undergoing progressive development, see eg. Carol, Prat

& López (1997) and Walter, Olesen & Stang (2005). The FCM is a special case of the bridge crack models (Cox & Marshall 1994) and in FCM smooth crack closure is insured.

Comparing concrete, the ECC-matrix and cement paste, cement paste is the most brittle followed by the ECC-matrix. This is usually explained by the toughening effect of the aggregate at various scales linked to mechanisms like micro-crack shielding, crack deflection, crack trapping and aggregate/ligament bridging, see (Li & Maalej 1996). Each of these mechanisms lends itself to bridged crack modeling, while fine mortar and cement paste alone are often considered as materials which can adequately be described by LEFM. Unfortunately employing the LEFM approach the first crack strength of the ECC-matrix becomes very sensitive to the sizes of the initial defects, which is in contrast to what is usually observed in experiments, see eg. (Wang & Li 2004).

A lot of effort has been put into developing strain-hardening materials and a large number of different cementitious strain-hardening materials have been developed over the years. Li (1992) has suggested a micro-mechanic based approach in the effort of developing a material with enhanced strain-hardening capability. Based on micro-mechanics two criteria were set up to achieve strain-hardening (Li & Leung 1992); (1) the tensile strength of the ECC-matrix has to be lower than the stress carrying capacity of the fibers in a crack, the so-called peak fiber-bridging stress and (2) the cracks have to propagate under constant crack opening, except near the crack tip, the so-called steady-state flat-crack propagation criterion. Both criteria for multiple cracking (Li & Leung 1992) are simplified and do not take into account the finite size of a test specimen, the geometry and boundary conditions of the specimen, and the interaction between cracks and initial defects (localization). Furthermore, it should be noted that the criterion related to steady-state crack propagation is based on a LEFM description of the ECC-matrix. These criteria were intended as guidelines for achieving strain-hardening and have been used for material development and optimization, see e.g. (Li 1998), (Li, Wu, Wang, Ogawa & Saito 2002) and (Walter et al. 2007).

Both criteria can be expressed in terms of cohesive laws for the fibers and the matrix. Thus, to engineer ECC-materials it is essential to be able to predict these cohesive laws. The cohesive law for the matrix can be found e.g. from a wedge splitting test and an inverse analysis (Østergaard 2003) and a closed form solution for the total response of the fibers has been derived (Maalej, Li & Hashida 1995), (Lin, Kanda & Li 1999) and (Zhang, Stang & Li 2001).

The criteria for multiple cracking insure that multiple cracking and subsequently strain-hardening will occur in a infinite sheet loaded in uniaxial tension. Apart from this the criteria do not give any information about the material behavior. Therefore to predict the behavior of an ECC-material in a construction a set of constitutive equations is needed. Due to the ductile behavior of the ECC-material its characteristics are best captured by a continuum model. During the last 50 years a wide range of continuum models have been derived for both brittle and ductile cementitious materials. Kachanov (1958) was the first to include damage parameters in a model for a cementitious material. In this model the elastic material parameters degrade as the damage-parameters increase. Another type of continuum model is the so-called smeared crack model, see eg. Bazant & Oh (1983) and Rashid (1968). The smeared crack model was original intended for tension-softening material, but the concept can be extended to strain-hardening materials. In the smeared crack model the strain is split into an inelastic part related to the cracks and an elastic part related to the material between the cracks. Han, Feenstra & Billington (2003) has developed a model to capture the unique features of the ECC-material under cyclic loading. This model is a total strain, rotating smeared crack model. The model is characterized by its detailed description of the unloading phase, which makes it suitable for cyclic loading simulations. Kabele (2002) has also derived a material-model for the ECC-material. This model is based on the smeared fixed crack approach, and differs from Han's model in its scheme to describe the tangential stiffness of the cracks. Here the fibers are described as randomly orientated elastic Timoshenko beams. In the model by Kabele the behavior of the cracks after initiation is described solely through the fibers.

The existing models for the ECC-material only takes in to consideration the behavior of the fibers when modeling the crack behavior and ignore the behavior of the ECC-matrix. Also the existing models give no information on crack opening and spacing associated with material points. Dick-Nielsen, Poulsen, Stang & Olesen (2004) found that cracks in the ECC-matrix reach significant lengths before the matrix becomes stress free. A realistic description of the ECC-material in the state, where the multiple cracking initiates should therefore include both the matrix and the fiber behavior as shown in (Dick-Nielsen, Stang & Poulsen 2005) and (Dick-Nielsen, Stang & Poulsen 2006*a*).

1.4 Overview of the Thesis

In the present thesis a material model for ECC will be derived through a multi scale approach. As suggested by Kabele (2004) three different length scales are used in this approach (see figure 1.5). On each length scale important phenomena are investigated using numerical and analytical calculations. The aim is to develop a material model that can be implemented on the structural scale. To do that an investigation of the mechanisms that appear on the lower scales has to be performed, because these mechanisms have an effect on the mechanisms on the higher scales. On the lowest scale investigated, an investigation is performed on the adequateness of the LEFM approach when modeling crack propagation in the ECC-matrix. Furthermore the phenomena that appear during crack propagation and fiber debonding are investigated on the single fiber level. On the second level the conditions for strain-hardening are investigated by simulating crack propagation for different ECC-materials. These simulations are performed for single cracks as well as multiple cracks, where we have interactions between micro cracks and initial defects. Finally a material model for the ECC-material is developed on the highest scale. Thanks to the ductile behavior of the ECC-material induced by the fibers a continuum model will be employed to model the material behavior. The present model differs from existing models by having a separate matrix and fiber description and by providing detailed information about crack spacing and opening. A smeared fixed cracking model will be used to capture the overall behavior of the ECC-material, where the matrix crack will be modeled by an elasto-plastic material model including damage parameters. The model will be implemented in a commercial finite element code and the capability of the model will be demonstrated through simulations.

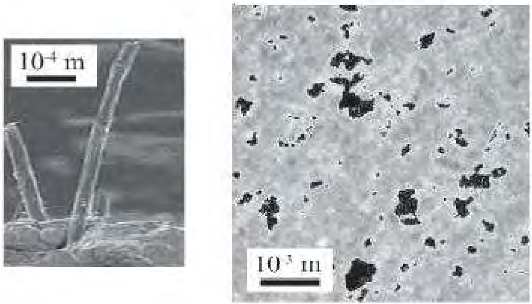

(a) Micro.

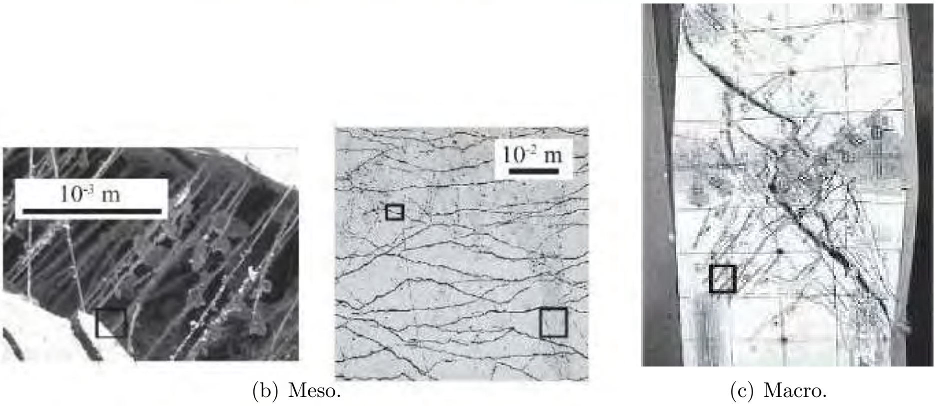

(b) Meso. (c) Macro.

Figure 1.5 *Scales in the modeling phase (Kabele 2004).*

In **Chapter 2** basic concepts are introduced.

The lowest scale discussed in this thesis is the micro scale (**Chapter 3**). The dimensions on this scale are 10^{-5} m. One phenomenon dealt with on this scale is initial flaws in the matrix and how micro cracks are initiated from these due to stress concentrations, see e.g. (Wang & Li 2004) and (Dick-Nielsen et al. 2004)(*Paper I*). Another set of phenomena are the debonding, bridging and pull-out of a single fiber, these phenomena have earlier been investigated by a large group of researchers both numerically and experimentally, see e.g. (Shao, Li & Shah 1993), (Li & Stang 1997) and (Lin et al. 1999) and (Dick-Nielsen, Stang

& Poulsen 2007*b*)(*Paper II*).

The next scale is the meso scale (**Chapter 4**). This scale can be divided into two scales. On meso scale I phenomena involving the propagation of a single crack bridged by many randomly oriented fibers are looked upon. On this scale experimental, numerical and analytical investigations have been performed by a number of researchers, see e.g. (Fischer et al. 2007), (Li & Liang 1986), (Stang et al. 2007) and (Dick-Nielsen, Stang & Poulsen 2007*a*)(*Paper III*). On meso scale II a part of the material that undergoes multiple cracking is investigated. In this part, interaction between initials flaws and micro cracks takes places and opening, closing and sliding of cracks are important phenomena. The meso scale II is the smallest part of a material that possesses the same characteristics as a material point on the structural scale. An element like this is called a Representative Volume Element (RVE). The dimensions on the meso scale is 10^{-3} m. Simulations of the interaction between the cracks in a specimen undergoing multiple cracking have been carried out by e.g. (Kabele & Stemberk 2005), (Dick-Nielsen, Stang & Poulsen 2006*b*) and (Fischer et al. 2007).

The macro scale is the structural scale and the material model will be employed on this scale (**Chapter 5**). The material behavior observed on this scale is the transition from a linear material behavior to a non-linear behavior where the material will undergo strain-hardening and later softening. The dimensions on this scale range from 0.1 m. The model, which is intended for the state, where the multiple cracks evolve, gives information about crack opening and spacing. The material model is based on smeared cracking and combined with generalized plasticity. To obtain information about the crack opening, spacing and number of cracks, concepts from continuum damage mechanics are implemented. This material model will effectively introduce multi-scale modeling and save computational time. Simulations on the macro scale on constructions made of SHFRCC-material has been carried out by, e.g. Han et al. (2003), Walter et al. (2007), Dick-Nielsen, Stang & Poulsen (2007*c*)(*Paper IV*), Dick-Nielsen, Stang & Poulsen (2007*d*)(*Paper V*) and Kabele & Kanakubo (2007).

Chapter 2

Fundamental Concepts of Localized and Multiple Cracking

In the present chapter, a brief introduction to the concepts of localized and multiple cracking employed in the thesis, will be given.

2.1 The Fictitious Crack Model

In the *fictitious crack model* (FCM) (Hillerborg et al. 1976) a crack in concrete is conceptually divided in two parts, a fictitious crack that transfers stresses and a part that is stress free (see figure 2.1). At the tip of the crack, a process zone, consisting of a number of micro cracks which weaken the material, exists. In continuation of the process zone a localized crack is formed. This localized crack can transfer stress thanks to aggregate interlock. After a certain crack opening is reached no more aggregate interlocking takes place and the crack becomes stress free. The FCM models the entire crack including the process-zone in one model. In the crack tip the cohesive stress is equal to the tensile strength, f_t, and as the crack opens, the cohesive stresses, $\sigma = \sigma_w(w)$, decrease as a function of the opening, w. The relationship between crack opening and stress is described through a cohesive law, where the area under the curve is defined as the fracture energy, G_F (see figure 2.1(b)). The brittleness of a cohesive material can be described using the characteristic length, l_{ch}:

$$l_{ch} = \frac{EG_F}{f_t^2} \tag{2.1}$$

where E is the elastic modulus. Stang et al. (2007) performed a numerical investigation on crack propagation in an infinite sheet for a material with a linear cohesive law. They found that a crack propagates stably as long as the crack length is smaller than the characteristic

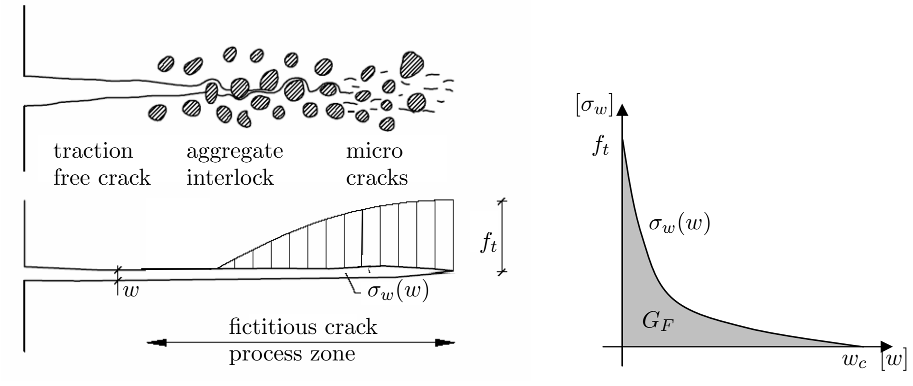

(a) Concept of the FCM. After (Stang 2005). (b) Cohesive law for pure concrete.

Figure 2.1 *Concept of the fictitious crack model (FCM).*

length. For larger crack lengths the applied far-field stress decreases and the crack growth becomes unstable. Apart from modeling of crack propagation in pure concrete material, the FCM model has also successfully been applied to model crack propagation in FRC materials, see e.g. (Löfgren, Stang & Olesen 2003) and (Østergaard & Olesen 2006).

In the present thesis the cracks investigated are primarily micro cracks with crack opening of the same magnitude as the micro cracks in the process zone in regular concrete. The FCM in this thesis is employed for crack openings of the same magnitude as the micro cracks traditionally associated with the process zone in pure concrete. In the terminology employed in the present thesis the process zone will refer to the entire fictitious crack.

2.2 The Criteria for Multiple Cracking

The fiber-bridging associated with cementitious materials is a combination of fiber debonding and fiber pull-out (see figure 2.2). This phenomenon has been investigated analytically by, e.g. Li, Stang & Krenchel (1993) and Lin et al. (1999) and numerically by, e.g. Dick-Nielsen et al. (2005). At first the fiber is embedded in the matrix and the interface between fiber and matrix is intact. Applying a load, P, will initially lead to an elastic elongation of the fiber part outside the matrix. As the load is increased the debonding phase begins and the stress-transfer capacity of the fiber-matrix interface begins to degrade. After complete debonding the fiber is pulled out.

For strain-hardening to occur in an ECC-material it is required, that the criteria for multiple cracking are satisfied. The second criterion requires that the cracks propagate

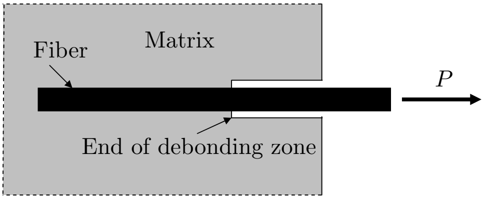

Figure 2.2 *Debonding of fiber.*

in a steady-state flat-crack mode. In contrast, if the crack opening is not confined during crack propagation the crack opening could lead to fiber rupture or pull-out. According to Griffith (1920) the crack opening in a linear elastic material as a function of the distance x from the center of the crack can be found from eq. (2.2) and matching values of the crack length, $2a$, and the applied far-field stress, σ, can be found from eq. (2.3), (where K_{IC} is the critical mode I stress intensity factor).

$$w(x) = \frac{2\sigma}{E}\sqrt{a^2 - x^2} \tag{2.2}$$

$$\sigma = \frac{K_{IC}}{\sqrt{\pi a}} \tag{2.3}$$

The Griffith crack mode results in a crack opening shaped as an ellipse, where the opening at crack middle increases as the crack propagates. To avoid fiber rupture and pull-out during crack propagation it is more favorable to have the crack propagate in a flat crack mode. The flat crack propagation was first analyzed by Marshall & Cox (1988) applying the J-integral approach. According to Marshall and Cox the complementary energy, J_b', of the fiber bridging curve has to be larger than the matrix toughness, J_{tip}, as illustrated in figure 2.3 and stated in equation 2.4:

$$G_F \approx J_{tip} \leq \delta_0\sigma_0 - \int_0^{\delta_0} \sigma(\delta)d\delta = J_b' \tag{2.4}$$

where δ_0 and σ_0 are the crack opening and fiber bridging stress at peak and the matrix toughness, J_{tip}, approaches the fracture energy for the matrix, G_F, for low fiber content. This criterion for steady-state crack propagation will be reevaluated in the present thesis applying a cohesive crack approach. According to the criterion a high complementary energy, J_b', is desirable. This can be achieved by raising the peak crack opening, δ_0, and bridging stress, σ_0, or decreasing the fracture energy of the matrix. The shape of the fiber bridging curve is controlled by the fiber-matrix interface and the fiber properties like fiber strength, length, diameter etc., where the strength of the interface can be controlled by coating of the fiber (Li et al. 2002).

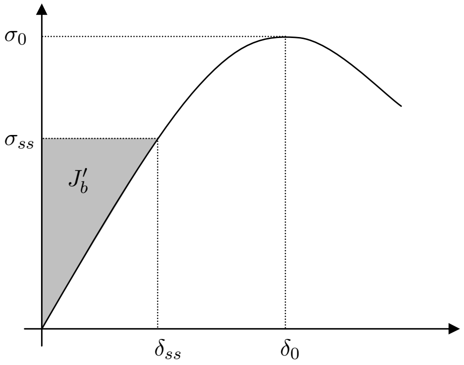

Figure 2.3 *Complementary energy, J_b', of the fiber bridging curve. Index "ss" refers to the current steady state load and index "0" refers to the peak values.*

Chapter 3

Material Properties on the Micro Scale

The ECC-matrix is a fine mortar or a cement paste with aggregates in the magnitude of 100 μm. Cementitious materials with that small aggregates are often considered as materials which can adequately be described by linear elastic fracture mechanics, LEFM. Unfortunately the LEFM approach to neat cement paste or fine mortar presents discrepancy with respect to the size of defects and their influence on apparent tensile strength of the bulk matrix. In *Paper I* a semi-analytical cohesive crack model was introduced to describe the influence of initial defects on the tensile strength of the ECC-matrix. Using the cohesive crack model the cohesive zone was predicted to be so long, that the LEFM does not apply.

The special characteristics of the ECC-material arise when the ECC-matrix is combined with the right kind of fibers, which will then bridge the cracks. The fiber-bridging, is a fundamental mechanism governing the nonlinear behavior of ECC and therefore important to understand when modeling the characteristics of the ECC-material. The cohesive stresses carried across the crack by the bridging fibers are often described with an (average) cohesive law. When a cohesive law is applied for the matrix crack as well, an average cohesive law emerges describing the crack in the composite. This average cohesive law for the composite is essential in order to model the behavior of the cracks in the ECC-material. The cohesive law for the matrix can be found e.g. from a wedge splitting test and an inverse analysis (Østergaard 2003), and a closed form solution for the total response of the fibers has been derived (Lin et al. 1999). Having arrived at the cohesive laws for the matrix and the fibers respectively, the remaining question is now: can the cohesive law for the ECC-material be found through a simple superposition of the two fundamental laws or will there be effects that make superposition invalid?

In *Paper II* the validity of the superposition scheme of the fundamental cohesive laws, to obtain the average cohesive law for a typical ECC-composite, was investigated. This investigation was based on three dimensional FEM calculations. The three basic cases: debonding and pull-out of a straight fiber perpendicular to the crack face, crack propagation in pure mortar and crack propagation in a Representative Volume Element (RVE) with mortar and fiber, were analyzed and a parameter study was carried out. Finally, a comparison of the numerical model and an analytical model for fiber debonding and pull-out was carried out.

3.1 Semi-Analytical Cohesive Crack Model

3.1.1 Semi-Analytical Cohesive Matrix Crack Model

In *Paper I* a semi-analytical cohesive crack model was derived to simulate crack propagation in the ECC-matrix. The cohesive law applied to the matrix was simplified by a bilinear cohesive law (see figure 3.1), which has proven adequate for mortar materials (Østergaard 2003). The material was assumed to be linear elastic until the tensile strength, f_t, was reached. After crack initiation the material softened and followed the cohesive law.

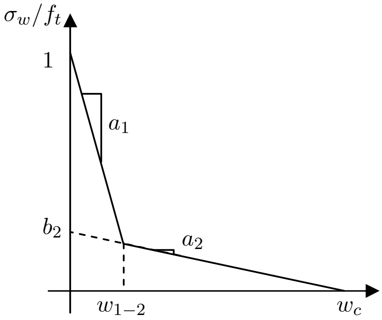

Figure 3.1 *Bilinear cohesive law.*

The semi-analytical model deals with crack propagation in an infinite sheet containing a center crack loaded in uniaxial tension (see figure 3.2). Concrete contains pores with irregular shapes and small defects along the edge. In this model these pores are replaced by a stress free penny shaped crack with the length, $2a_0$, corresponding the sum of the pore diameter and the length of the defects. The total length of the propagated crack is $2a$ and the total opening of the crack is denoted $w(x)$. The crack is assumed to be stable when the stress intensity factor, K_I, is equal to zero, which corresponds to smooth crack closure. The model is derived by integration of an exact solution for a pair of opposite point loads. A validation of the model has been made in *Paper III* where the results have been compared to the corresponding results from a FEM analysis.

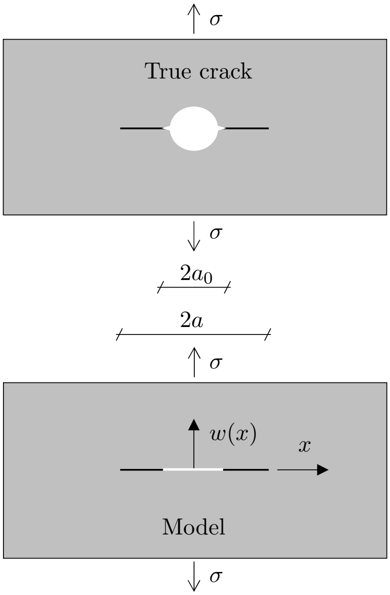

Figure 3.2 *Geometry for the semi-analytical model. A pore is simplified with a stress free slit-like crack with the length,* $2a_0$*, and the total length of the crack is* $2a$*. The sheet is loaded with the far-field stress,* σ*. The total opening of the crack is denoted* w*.*

According to exact solutions in Tada (1985) it is found that the stress intensity factor, K_I, only is weakly influenced by the shape of the initial flaw. The stress intensity factor changes less than 1 % when altering the shape of the initial flaw from a slit-like crack to a circle, for crack lengths at peak stress. This indicates that the shape of the original stress free crack is not that important for the first crack strength. Therefore, the present analysis is expected to give a reasonable result, regardless of the initial shape of the stress free crack.

3.1.2 Fundamentals

Crack initiation and propagations in the ECC-matrix are important phenomena in the effort to achieve strain-hardening in ECC. The cracks in ECC are initiated from micro defects. If there are too few micro cracks or they are too small, only a few cracks will be present in the saturated state (Wang & Li 2004). The influence of the initial crack length, a_0, as well as the shape of the cohesive law on the first crack strength, σ_{fc}, has been investigated in *Paper I*. For a mortar with the same mixing as mix 3 in (Wang & Li 2004), material data have been obtained from a wedge splitting test (WST) carried out by Wang at The Technical University of Denmark and an inverse analysis (Østergaard 2003).

The following material data were found: the tensile strength, $f_t = 2.8$ MPa, the cohesive law constants, $a_1 = -1.56 \cdot 10^5$ m^{-1}, $a_2 = -9.74 \cdot 10^3$ m^{-1} and $b_2 = 0.24$, the fracture energy $G_F = 14.1$ N/m and the elastic modulus, $E = 31$ GPa.

These material data are specific for one ECC-matrix under certain conditions and thus only meant as an example. Suitable parametric variations to these material data are performed.

3.1.3 Crack Initiation and Propagation in the Matrix

The material data derived from the wedge splitting test and the inverse analysis are typical for a ECC-matrix. However some uncertainty is associated with the determination of the tensile strength in the inverse analysis. Therefore in the investigation, the fracture energy, G_F, and the second part of the cohesive law a_2, b_2 are held constant, while the tensile strength, f_t, and thereby the slope of the first part of the cohesive law, a_1, will be varied. The first crack strength of ECC, σ_{fc}, is mainly controlled by matrix properties. Typically values of the first crack strength of ECC, observed in experiments, are in the range of 3-6 MPa (Li et al. 2002) and (Wang & Li 2004). The matrix tensile strength, f_t, in the present investigation is therefore varied in this range.

The size distribution of the initial flaws in the matrix, has a large influence on whether the ECC-material will undergo strain-hardening as described by Wang & Li (2004). The simulations will therefore be performed for the initial stress free flaws with radius, a_0, in the range from 0.5 mm to 2 mm. The variations of the radius will show the matrix sensitivity to flaw sizes.

In figure 3.3 the relationship between the half crack length, a, and the far-field stress, σ, is shown for a tensile strength of 3 and 5 MPa. To enable comparison the solution according to LEFM is plotted as well ($\sigma\sqrt{\pi a} = K_{IC} = \sqrt{EG_F}$).

To achieve strain-hardening in ECC-material, cracks have to run through the material at a far-field stress lower than the peak fiber-bridging stress. An easy way to achieve this is to increase the size of the initial flaws or to employ a matrix with a low tensile strength, f_t (see figure 3.3). The simulations showed that keeping the fracture energy, G_F, fixed while decreasing the tensile strength, f_t, leads to more stable crack growth. Furthermore all curves independent of the tensile strength, approach the LEFM curve asymptotically for large cracks. This fits well into the theory of LEFM where the fracture process zone is regarded as a point.

All simulations showed the same tendency regarding the devolvement of the crack opening profile. Figure 3.4 illustrates the development of the opening profile and the cohesive stresses in the process zone for an initial crack length, a_0, of 1 mm.

In figure 3.4(a) the opening profiles for a crack length, a, of 7 mm, 12.5 mm and 25 mm

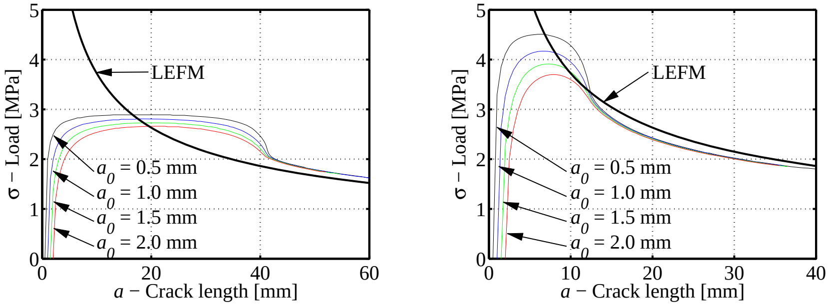

(a) Tensile strength $f_t = 3$ MPa. (b) Tensile strength $f_t = 5$ MPa.

Figure 3.3 *Far-field stress, σ and matching crack length, a.*

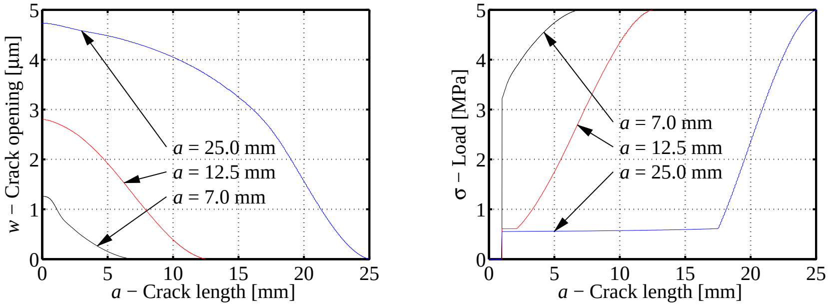

(a) Total crack opening. (b) Cohesive stress.

Figure 3.4 *Crack opening profiles and matching cohesive stresses for the matrix with a tensile strength, $f_t = 5$ MPa and initial crack length, $a_0 = 1$ mm*

are plotted ($f_t = 5$ MPa). At a crack length, a, of 7 mm the first crack strength, σ_{fc}, (peak stress) is reached (see figure 3.3(b)). The crack opening reaches the opening w_{1-2} at which the second part of the cohesive law is activated at a crack length of 12.5 mm. The slope of the cohesive law for this material changes at an opening, w_{1-2}, of 2.59 μm (see figure 3.1). At a crack length, a, of 25 mm most of the crack is related to the second part of the cohesive law. For this material the crack growth becomes unstable for a crack length, a, of approximately 10 mm, as shown in figure 3.3(b). The characteristic length, l_{ch}, (eq. (2.1)) can according to Stang et al. (2007) be used to predict when the crack growth becomes unstable. As shown in figure 3.4 only the first part of the cohesive law has influence on the stable crack growth. Therefore when calculating the characteristic length only the fracture energy related to the slope, a_1, is employed. For the material with a tensile strength, f_t, of 3 MPa and 5 MPa the characteristic lengths are then calculated to 35 mm and 9 mm respectively. This fits well with the results in figure 3.3 where the far-field stress decreases and the crack growth becomes unstable after the characteristic lengths are reached.

In figure 3.5 the first crack strength, σ_{fc}, is plotted as a function of the initial stress free crack length, a_0. The results show that for a matrix with a low tensile strength, f_t, the first crack strength dependence on the size of the initial flaw, a_0, is very weak. As the tensile strength increases the dependence becomes more pronounced, thanks to the fact that the fracture energy, G_F, is kept constant, while the matrix becomes more brittle as the tensile strength increases. The tensile strength, f_t, of the ECC-matrix is often kept low (below 4 MPa) to insure many cracks in the saturated state. For these matrices the size of the initial flaws only have a weak influence on the first crack strength. As the initial flaw size, a_0, increases the first crack strength predicted by the cohesive model approaches that predicted by LEFM. The initial flaws found in a typical ECC-matrix often have a radius, a_0, in the range of 1 mm. This means that although the ECC-matrix is often regarded as brittle, LEFM can not be used to calculate the first crack strength, σ_{fc}, when reasonable initial flaw sizes are considered. The ECC-matrix will therefore be regarded as a cohesive material in the remaining part of the thesis.

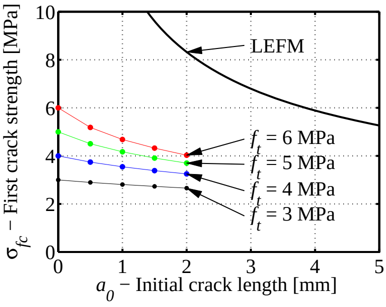

Figure 3.5 *Relation between first crack strength, σ_{fc} and initial crack length, a_0.*

3.2 Superposition of Cohesive Laws

When a crack propagates in a cementitious material a tensile stress field in front of the crack is formed as described by Cook, Gordon, Evans & Marsh (1964). The direction of these tensile stresses are parallel to the crack surface. This stress field can lead to debonding of the fiber before the crack reaches the fiber, and pull-out occurs. In the present thesis this effect will be denoted as the Cook/Gordon effect. The relationship between crack opening and the total fiber-bridging stress derived by Lin et al. (1999) is based on integration of an analytical solution for a single fiber undergoing debonding and pull-out. If significant fiber-matrix debonding takes place before the crack tip reaches the fiber, the fiber pull-out case with an initially perfect fiber-matrix interface, would not be representative of the fiber-bridging case and a direct superposition would not be valid. In the present section it will be examined whether superposition of the cohesive laws holds true or if the Cook/Gorden effect makes it invalid. Another effect possibly invalidating superposition could be matrix spalling ((Leung & Li 1992), (Leung & Chi 1995)) taking place at the crack surface during inclined fiber debonding and pull-out. However, here matrix spalling is assumed to be a phenomenon primarily associated with fiber pull-out and thus not associated with the initial matrix crack propagation and fiber-matrix debonding. In the present investigation only initial matrix crack propagation and the associated fiber-matrix debonding is investigated and thus matrix spalling is not included and only a fiber oriented perpendicular to the matrix crack surface is modeled.

An investigation of the significance of the Cook/Gorden effect in ECC is carried out in *Paper II.* In an initial investigation the stress field ahead of the crack, in a cohesive model, was compared with that presented in the paper by Cook et al. (1964). The investigation showed that the Cook/Gordon effect was more pronounced in the cohesive approach. The primary analysis was based on the concept of a Representative Volume Element (RVE). Traditionally an RVE can be thought of as an element containing a sufficient number of microstructural inhomogeneities in order for it to be considered macroscopically homogeneous. Alternatively, it can be thought of as a (small) repetitive element from which a true RVE can be constructed. In both cases the element is subjected to boundary conditions which would introduce a homogeneous stress and strain state in the element, if the element was homogeneous, thus allowing for simple interpretation of the behavior of the inhomogeneous element in terms of average properties such as e.g. stiffness. In the investigation the latter approach was taken. A three dimensional FEM model of a RVE was set up employing the commercial FEM package DIANA (see figure 3.6). The matrix was modeled using 20 node, cubic shaped, solid elements, the fiber using 15 node, wedge shaped, solid elements, while 8+8 node interface elements were used to model the debonding of the fiber and the crack propagation in mortar. The displacements perpendicular to the end planes in the (x, y)-plane were constrained. This caused the load to be applied as a displacement load. The nodes in each side of the RVE in the (z, x)- and (z, y)-plane were tied together in the direction perpendicular to the plane. This caused the edges in the (x, z)- and (y, z)-planes to remain plane and resulted in a stress state throughout the RVE, on average equal to plane stress.

During fiber debonding, the interface between the mortar and the fiber was exposed to stresses in the normal direction as well as the tangential directions, i.e. mixed mode crack propagation and opening. To simulate this, a user defined incremental mixed mode interface model was employed (Walter et al. 2005). In this model the normal stress, $\sigma = \sigma(\delta_t, \delta_n)$, and the shear stress, $\tau = \tau(\delta_t, \delta_n)$, were described as functions of both the displacement in the tangential, δ_t, and the normal, δ_n, direction. The three basic cases: debonding and pull-out of a straight fiber perpendicular to the crack face, crack propagation in pure mortar and crack propagation in a RVE with mortar and fiber were analyzed.

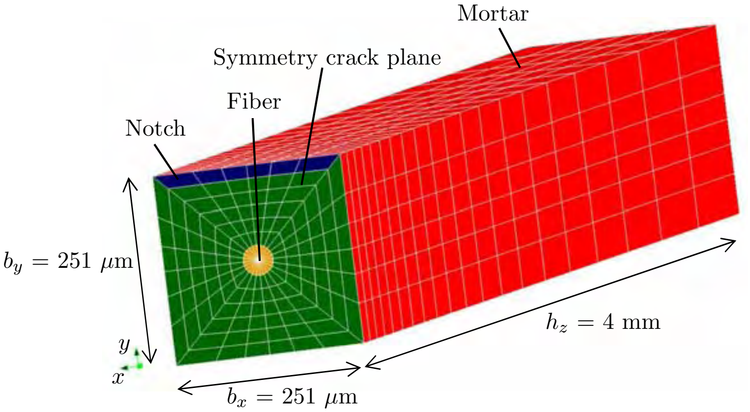

Figure 3.6 *The mesh applied in the total model.*

The Cook/Gorden effect would only have influence on the first part of the debonding and pull-out phase. The dimensions of the model were therefore chosen as: fiber diameter 40 μm, length of the sides in the (x, y)-plane, b, is 251 μm and model height, h_z, is 4 mm. This gives a fiber volume percent of 2, which is typical for ECC. Symmetry was assumed and therefore only half a crack plane was modeled. The model contained a notch from which the crack was initiated.

The model containing the fiber as well as the mortar crack (in the symmetry crack plane) is referred to as the total model. When the mortar crack is replaced with a free surface, the model can be used to simulate fiber debonding and pull-out. For the sake of convenience this model is referred to as the fiber pull-out model. Replacing the fiber with mortar and letting the mortar crack interface cover the entire bottom surface, the model can simulate crack propagation in pure mortar.

3.2.1 Deriving the Average Cohesive Law from the RVE

An average cohesive law (σ_w, w) can be derived from the FEM simulations, identifying σ_w with the applied load and w is the average crack opening (see figure 3.7). The average crack opening, w, can be found by taking the total elongation, δ, and subtracting the elastic elongation:

$$\begin{aligned} &\delta = \varepsilon L + w/2 \\ &\delta = \sigma/(E_f V_f + (1 - V_f)E_m)L + w/2 \end{aligned} \tag{3.1}$$

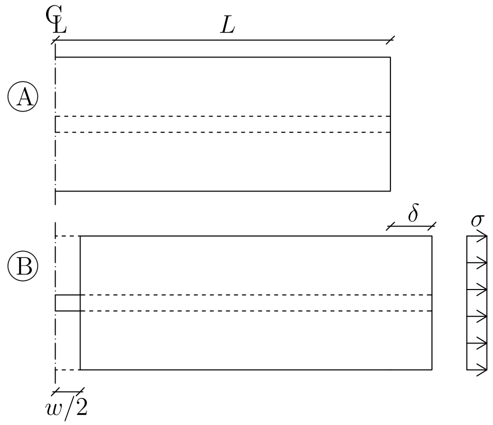

Figure 3.7 *Relationship between average crack opening, $w/2$ and applied stress, σ.*

$$w/2 = \delta - \sigma/(E_f V_f + (1 - V_f)E_m)L \qquad (3.2)$$

Here E_f and E_m are the plane stress elastic moduli for the fiber and the mortar respectively, V_f is the fiber volume concentration, σ is the average stress applied by the prescribed displacement and the elastic strain, ε, can be found from the applied stress and the composite stiffness. Using this equation all effects from non-uniform crack opening and initial debonding will be included in the average crack opening. Furthermore this formulation enables the determination of an average crack opening without integrating over the actual crack opening profile. Eq. (3.2) can be used for the total model, the fiber pull-out model and the pure matrix model. This makes comparison between the obtained (σ_w, w)-relations from the different models consistent.

3.2.2 Material Parameters

The cohesive law for the matrix is based on experimental investigations on a typical ECC-matrix (obtained by S. Wang, University of Michigan) where a bi-linear cohesive law is determined from wedge splitting tests and inverse analysis. The mode I cohesive law for the mortar is assumed to be bi-linear as shown in figure 3.1. The following parameters were determined: the tensile strength f_t = 2.8 MPa, the cohesive law constants a_1 = -156 mm^{-1}, a_2 = -9.74 mm-1 and b_2 = 0.24, the fracture energy G_F = 14.1 N/m, the elastic modulus E = 31.0 GPa and the Poisson's ratio ν = 0.2.

The cohesive law for the interface between the mortar and the fiber is difficult to measure and therefore a parameter study was carried out. Values determined by Shao et al. (1993) are taken as a basis for the mode II cohesive law, while the mode I cohesive law is estimated. The Young's modulus for the PVA fibers is E_f = 42.8 GPa and the Poisson's ratio is chosen to $\nu = 0.2$. This Poisson's ratio is chosen to isolate the Cook/Gordon effect from any influence of a possible Poisson's effect. In the parameter study the effect of the Poisson's ratio was investigated separately. The cohesive mode II law for the fiber-matrix interface is also bi-linear and has the following values: The shear strength τ_{max} = 3 MPa, constants a_1 = -222 mm^{-1}, a_2 = -19.6 mm^{-1} and b_2 = 0.392. The mode I cohesive law for the fiber-matrix interface is estimated to vary linearly with a tensile strength of 0.5 MPa and a constant a_1 of -1000 mm^{-1}.

3.2.3 Cohesive Laws

In figure 3.8 average cohesive laws for the total model, the pure matrix model and the fiber pull-out model are shown. The curves are plotted based on the FEM results and eq. (3.2). In addition to the three curves a superposition of the fiber pull-out curve and the pure matrix curve is plotted. As shown in the figure superposition is valid for the chosen material parameters. This means that the Cook/Gorden effect is not significant in this case. In the next section the mechanisms appearing during crack propagation and fiber debonding will be examined, to get an understanding of why superposition is valid.

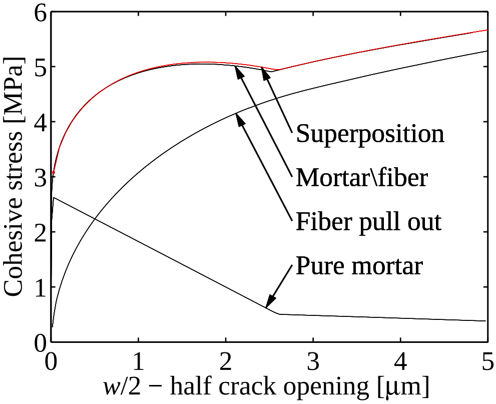

Figure 3.8 *Average cohesive laws.*

3.2.4 Matrix Crack Propagation vs. Fiber Debonding

The crack front is plotted as a function of the load level in figure 5.23(a). At an applied load of 2.32 MPa the crack front is located close to the notch. As the crack starts to propagate the front is arrested in front of the fiber, forcing the crack to propagate around the fiber and then open the rest of the crack from behind. After the crack is opened around the fiber the crack opening is less than 10 nm.

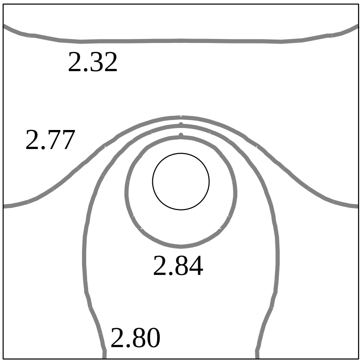

Figure 3.9 *Crack front for different loading stages (Load in MPa).*

Figure 3.10(b) illustrates crack propagation in the matrix vs. the debonding of the fiber at an applied load of 2.80 MPa. Figure 3.10(a) shows a cut in the FEM model and two thick black lines marks the matrix crack and fiber front illustrated in figure 3.10(b). The opened interface nodes are marked with circles and the deformations are scaled with a factor 100. The first debonding of the fiber begins at an applied load of 2.80 MPa. At this load level only the interface node at the bottom of the fiber is opened, which indicate that debonding has progressed 22 μm along the front of the fiber. As shown in figure 5.23(a) the crack has passed the fiber at this load level. This means that the Cook/Gordon effect is present but insignificant for the present choice of material parameters.

The investigation shows that the matrix crack propagation and the subsequent fiber debonding and pull-out are essentially two separate mechanisms in the sense that the matrix crack propagated through the RVE without initiating any significant debonding: the matrix crack grows past the fiber and then gradually back towards the fiber before significant debonding begins.

3.2.5 Stresses Along the Fiber-Matrix Interface

The applied load, σ, and the stresses along the fiber-matrix interface are shown for the total model and the fiber pull-out model in figure 3.11 and 3.12 respectively. The stresses are taken from the fiber front marked on figure 3.10(a).

The maximum normal and tangential stresses in the mixed mode cohesive laws for

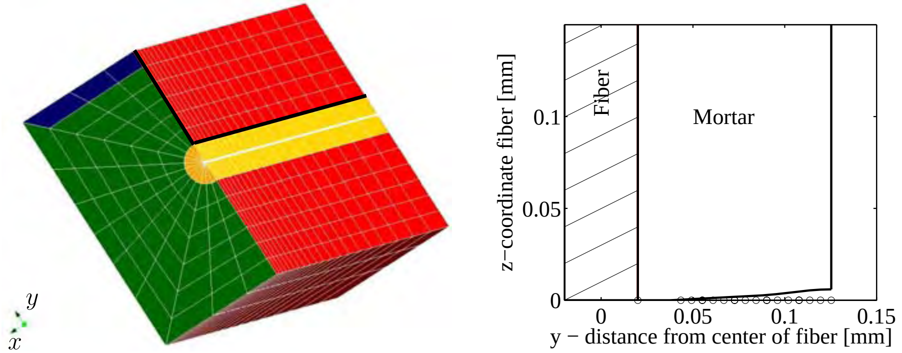

(a) Cut in model. (b) Debonding versus crack propagation.

Figure 3.10 *Debonding versus crack propagation.*

the matrix-fiber interface are 0.5 MPa and 3.0 MPa, respectively. In figure 3.11(b) and 3.11(c) it is seen that neither of these maximum values are reached, which means that the crack propagates in mixed mode in the total model. It is characteristic for the entire debonding process that a normal stress field is build up in front of the shear stress field. After the normal stress field is build up at the matrix crack, it then propagates along the fiber followed by the tangential stress field.

The results from the fiber pull-out model (3.12) are very similar to the results obtained from the total model. A normal tensile stress field is present in front of the debonding zone, even without the presence of a matrix crack. This tensile stress field is not accounted for in the analytical fiber model, which is the foundation for the derivation of the cohesive fiber-bridging law by Lin et al. (1999).

The debonding process in the two basic cases were very similar, which explains why superposition of the cohesive laws were valid. Apart from that the Cook/Gorden effect was found to be very week, which separated the matrix crack propagation and the fiber debonding in two separate processes.

3.2.6 Parameter Study of the Cohesive Laws

A parameter study of the mixed mode cohesive law was carried out in *Paper II*. The tensile strength in the cohesive normal law was varied in the range from 0.125-0.5 MPa, while the shear strength was varied in the range from 1.5-3 MPa. The results obtained in this study were very similar to those obtained in the previous sections. And the conclusion remained that superposition was valid.

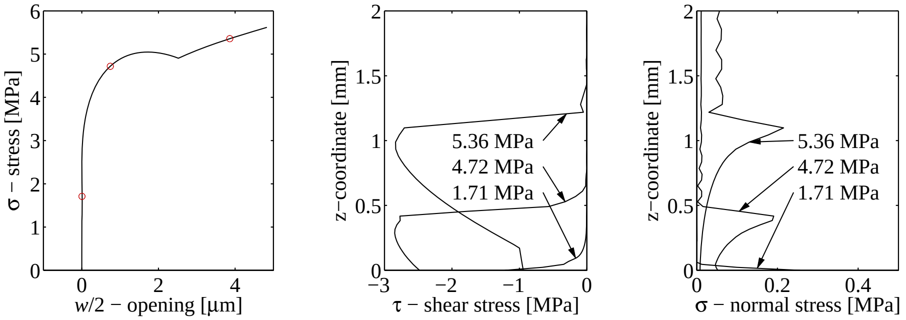

(a) Applied total stress. (b) Shear stresses on fiber front. (c) Normal stresses on fiber.

Figure 3.11 *Stresses on fiber front - Total model.*

Identical Poisson ratio's for the matrix and the fiber has so far been employed to separate the Cook/Gorden effect from a possible Poisson effect. In *Paper II* an investigation on the Poisson effect was carried out. Here the fiber was given a Poisson ratio of 0.35 which is more realistic for a PVA-fiber. The increase in the Poisson ratio did cause the normal stresses on the front of the fiber to increase as expected. However the superposition scheme was still valid because the Poisson effect had the same effect on the total model as it did in the fiber pull-out model.

3.2.7 Comparison of the Analytical and Numerical Model for Fiber Pull-Out

Four basic assumptions were made by Lin et al. (1999) to derive an analytical model to predict the bridging law for the fibers: (1) a ratio between fiber length and diameter larger than 100, (2) the slip between matrix and fiber during debonding is negligible hence the shear stresses are constant, τ_0, (3) the Poisson ratio has only little effect on the result and (4) the elastic elongation of the fiber is small compared with pull out after complete debonding. Assumption (4) is not of interest in this investigation because the computation is stopped before the debonding is completed. Assumption (1) and (3) are valid in this investigation as well, while assumption (2) thanks to the use of cohesive laws is not valid here. Apart from the four assumptions mentioned above, the analytical model does not take into account the tensile stress field in front of the debonding zone. This means that the fiber in the analytical model debonds under pure mode II conditions. The relationship between the pull-out force, P, and the relative displacement, δ, between the fiber and the matrix in the analytical model, is given by the expression below:

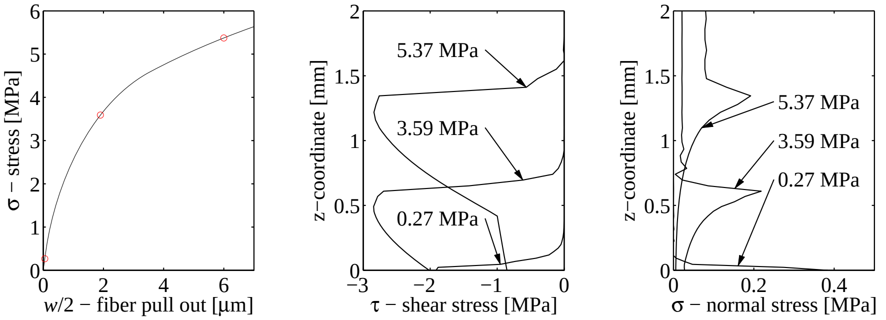

(a) Applied load. (b) Shear stresses on fiber front. (c) Normal stresses on fiber.

Figure 3.12 *Stresses on fiber front - Pull out model.*

$$P = \sqrt{\frac{\pi^2 \tau_0 E_f d_f^3 (1+\eta)}{2}\delta + \frac{\pi^2 G_d E_f d_f^3}{2}} \tag{3.3}$$

where E_f is Young's modulus, d_f the fiber diameter, G_d the chemical bond strength and $\xi_f = V_m E_m / V_f E_f$ where V_m and V_f is the volume fraction of mortar and fiber respectively. The chemical bond strength G_d is related to the fracture energy, G_F, of the mode II cohesive law, however in the analytical model, G_d is assumed to be dissipated in a point. A direct comparison of the numerical and the analytical model was not made due to the fact that constant shear stress is assumed in the analytical model. Therefore an investigation on the effect of the cohesive mode I law in the numerical model was carried out. In the investigation the shear strength of the mode II cohesive law was set to 3 MPa, while the strength of the mode I cohesive law was varied. The results from this investigation are shown in figure 3.13. The Poisson's ratio for the fiber in this investigation was set to 0.35.

The results show that the pull-out load decreases with a decreasing tensile strength in the mode I cohesive law. When employing the analytical model the material constants will be calibrated by a pull-out test. The influence of leaving out the mode I part is probably not that significant, because the constants will be affected by the mixed mode conditions.

3.3 Concluding Remarks

In *Paper I* a comparison between LEFM and the cohesive approach for modeling crack propagation in the bulk matrix was carried out. Using the cohesive crack model the cohesive zone was predicted to be so long that the LEFM does not apply, although the

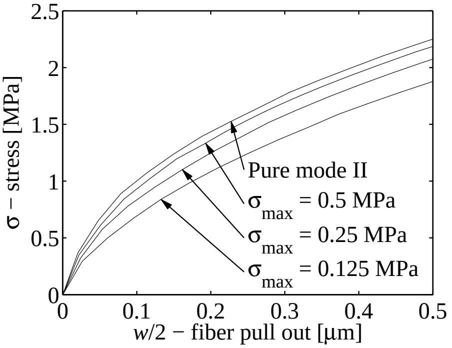

Figure 3.13 *Fiber pull-out curves for different mode I cohesive laws and a fixed mode II law using the numerical model with a Poisson's ratio in the fiber of 0.35*

bulk matrix is commonly regarded as brittle. In the remaining part of this thesis the cohesive approach will be applied for crack propagation in the matrix. Furthermore the investigation showed that for a fixed fracture energy, G_F, decreasing the tensile strength, f_t, leads to a more stable crack growth. Finally this investigation showed that, as the tensile strength was decreased, the size of the initial flaw, a_0, had only a weak influence on the first crack strength, σ_{fc}.

In *Paper II* it has been examined whether superposition of average cohesive laws is valid in order to arrive at an average cohesive law for the ECC-material. Special attention was given to the Cook/Gorden effect which proved to be insignificant in this connection. While the investigations were limited to the case of straight fibers arranged perpendicular to the crack surface, the present investigation showed that for small crack openings, superposition is valid. This was mainly due to the fact that matrix crack propagation and subsequent fiber debonding and pull-out essentially were found to be two separate mechanisms. First the crack propagated around and past the fiber after which the fiber debonded.

Chapter 4

Crack Propagation on the Meso Scale

The criteria for multiple cracking, introduced in chapter 1 and 2 are based on LEFM and fiber-bridging. These criteria have served well for creating an overall understanding of the influence of various parameters, and furthermore they have served as guidelines for material optimization, see e.g. (Li et al. 2002) and (Walter et al. 2007). In *Paper III* a cohesive crack model was employed, and the stability of crack propagation of a single crack was investigated. When ECC undergoes strain-hardening, an interaction between the cracks takes place, but this was not taken into consideration in the analysis. However the analysis relied on the implicit assumption that the fiber-bridging stress was eventually able to produce more cracks adjacent to the first crack and thus create multiple cracking and strain-hardening; if 1) the first crack strength (peak far-field stress) was smaller than the peak fiber-bridging stress and 2) the first crack propagated at crack openings smaller than the deformation associated with the peak on the fiber-bridging curve. In the investigation, simulations were carried out for uniaxial tensile tests containing one predefined flaw. The simulations dealt with matrix and fiber properties, specimen size, boundary conditions and the position and size of the initial flaw. The semi-analytical model derived in *Paper I* was employed for infinite sheets containing a center crack, while FEM models were employed for sheets containing edge cracks and sheets with finite geometry.

On the meso scale II simulations on a sheet loaded in uniaxial stress were performed (Dick-Nielsen et al. 2006*b*). In these simulations the interaction between initial stress free flaws and micro cracks are investigated in the initial stage of multiple cracking.

4.1 Geometry and Material Parameters

At the present time only a few standard specimen and test setups exist for testing the strain-hardening capacity in ECC. To arrive at some general conclusion, a number of simulations on crack propagation has been carried out in *Paper III* for infinite sheets, to obtain some general results. Simulations on finite sheets has been performed as well to relate the general results to finite geometry. All the simulations were for sheets loaded in uniaxial tension.

The ECC-matrix employed in these simulations was the same as used in section 3.1.2: the tensile strength, $f_t = 2.8$ MPa, the stress-separations constants, $a_1 = 156$ mm^{-1}, $a_2 = 9.7$ mm^{-1} and $b_2 = 0.24$, the fracture energy, $G_F = 14.1$ N/m and the elastic modulus, $E = 31$ GPa.

A closed-form solution derived by Lin et al. (1999) was employed to calculate the fiber-bridging curve. For the fibers, following material constants were used: the slip-hardening coefficient, $\beta = 2.21$, the fiber volume fraction $v_f = 0.02$, the snubbing coefficient, $f = 0.3$, the fiber strength reduction coefficient, $f' = 0.3$, the fiber length, $L_f = 12$ mm, the frictional stress, $\tau_0 = 0.3$ MPa, the elastic modulus of the fiber, $E_f = 42.8$ GPa, the chemical bond strength, $G_d = 4.71$ N/m, the fiber diameter, $d_f = 39.6$ μm and the in-situ fiber strength, $\sigma_{fu} = 1400$ MPa.

The resulting cohesive law for the ECC-material could then be found, using superposition as discussed in chapter 3. The cohesive laws for the matrix, the fibers and the ECC-material are shown in figure 4.1.

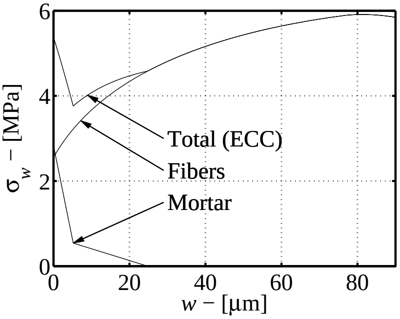

Figure 4.1 *Average cohesive laws.*

4.2 LEFM Versus the Cohesive Crack Approach

In *Paper II* a comparison between LEFM and the cohesive approach has been made to assess the difference between the approaches. To simulate crack propagation in the matrix, the Griffith approach (LEFM: eq. (2.2)-(2.3)) and the semi-analytical model were employed. In the semi-analytical model the cohesive law was employed while the LEFM approach was for a matrix with a fracture energy equal to that in the cohesive approach ($K_{IC} = \sqrt{EG_F}$). A simulation of crack propagation in the ECC-material was carried out as well, using the semi-analytical model to assess the influence of fibers. All the simulations were for infinite sheets containing a center crack and loaded in uniaxial tension. The length of the initial stress free flaw, $2a_0$, is 4 mm. The results from the simulations are shown in figure 4.2.

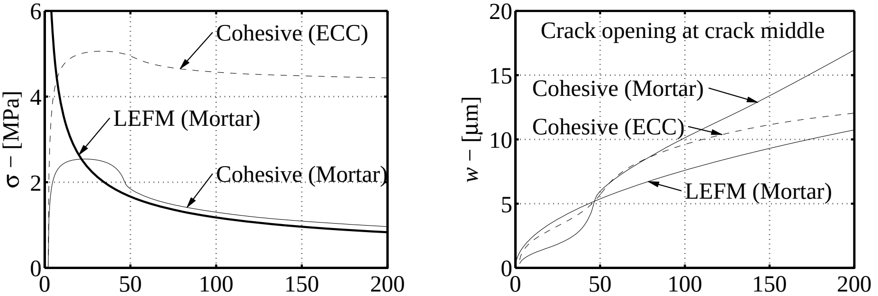

(a) Half crack length, a, and matching far-field stress, σ.

(b) Crack opening at crack middle.

Figure 4.2 *Comparison of the cohesive crack approach and LEFM.*

The investigation showed that both approaches predict crack openings of the same magnitude. For crack openings, a, up to 47 mm the Griffith approach predicts the largest openings, while the cohesive approach predicts the largest openings for larger crack lengths. For a crack length, a, of 200 mm both approaches predict crack openings smaller than 20 μm. This indicates that even without the representation of fibers, cracks will propagate with small crack openings, as long as the crack has not propagated through the specimen.

The relationship between crack length, a, and applied load, σ, for the ECC-material has a remarkable resemblance with the corresponding relationship to the matrix. This is not surprising, because the first part of the cohesive law for the ECC-material resembles the first part of the cohesive law for the matrix. For large crack lengths the force needed to drive the crack in the ECC-material is higher than the corresponding force needed for the matrix. For the matrix as well as for the ECC-material, the second branch of the cohesive law is reached at an opening, w_{1-2}, of 5 μm. For openings larger than this, the increase in opening is reduced (see figure 4.2(b)). The second branch of the cohesive law for the ECC-material is a hardening branch, while for the matrix it is a softening branch. This is why the openings for large cracks are largest in the matrix without fibers.

According to the criterion for steady-state flat-crack propagation (eq. (2.4)), cracks will propagate in a steady-state manner, if the complementary energy of the fibers is larger than the fracture energy of the matrix. The total complementary energy for the fibers is 81.2 N/m, while the matrix has a fracture energy, G_F, of 14.1 N/m. The peak load for the ECC-material is 5.1 MPa and occurs at a crack length, a, of 33.5 mm (see figure 4.2(a)). The crack opening in the center is 3.9 μm at peak load as shown in figure 4.2(b) and 3.3 μm in the beginning of the process zone ($x = 2$ mm). The utilized complementary energy for an opening of 3.3 μm is 0.75 N/m, which only corresponds to 5 % of the fracture energy. In order to utilize complementary energy in a point larger than the fracture energy, the opening has to be larger than 19 μm. For a total crack length, $2a$, of 400 mm, the crack opening in the crack middle is less than 15 μm.

4.3 Conditions under which Matrix Cracks Propagate in ECC

4.3.1 Influence of Initial Flaw Size

An investigation was carried out to assess the influence of initial flaw sizes in an ECC-material. The investigation was carried out for infinite sheets containing a center crack, as well as sheets containing an edge crack. The simulations for the center cracks were performed with the semi-analytical model, while the simulations for the edge cracks were performed using a FEM model. The employed FEM model contained an interface in which the crack could propagate. The model had a height of 1000 mm and a width of 1200 mm and contained an initial slit-like center flaw with the length, $2a_0$, of 4 mm. The model consisted of 30 x 206 (height x width) quadrilateral, 8 nodes plane stress elements. The element size increased by a factor of 1.03 from the flaw tip towards the edge along the width, and by a factor of 1.55 from the flaw towards the loaded edges along the height. In the FEM simulations, the boundary conditions along the two loaded edges, resulted in a uniform displacement in the load direction along the width. In order to make the results for sheets directly comparable, the total length of the edge flaw is denoted, a_0, while the total length of the center flaw is denoted, $2a_0$. The results from the simulations are shown in figure 4.3 and 4.4.

As it was also the case for the matrix, increasing the length of the initial flaw, a_0, leads to a decrease in first crack strength, σ_{fc}. As shown in figure 4.3 the sheets containing an edge crack are most sensitive to the size of the initial flaw. For crack lengths, a, smaller than 200 mm the crack opening is confined to 20 μm, independent of the position of the flaw. Thanks to the confined crack opening, the process zone never becomes fully evolved. Do to the considerable length of the process zone compared to the length of the initial flaw, LEFM can not be applied for modeling of crack propagation in cementitious

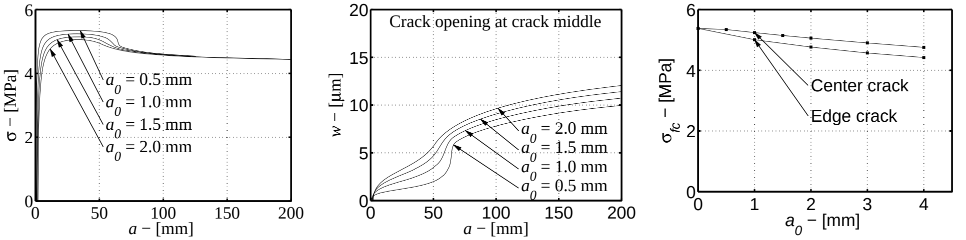

(a) Half crack length, a, and matching far-field stress, σ.

(b) Opening at crack middle, w, and matching half crack length, a.

(c) Relation between first crack strength, σ_{fc}, and the initial flaw length, a_0.

Figure 4.3 *Influence of initial flaw length, a_0 - center crack.*

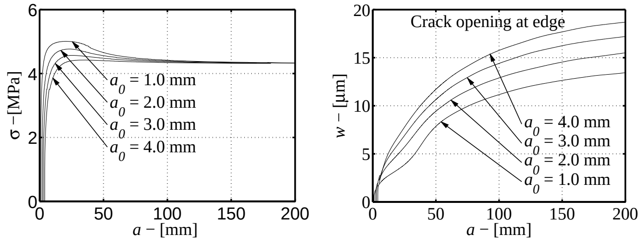

(a) Total crack length, a, and matching far-field stress, σ.

(b) Crack opening at the edge, w, and matching total crack length, a.

Figure 4.4 *Influence of initial flaw length, a_0 - edge crack.*

materials containing fibers.

4.3.2 Influence of the Matrix Tensile Strength

For strain-hardening to occur in ECC-materials, the tensile strength of the matrix has to be lower than the peak fiber-bridging stress. A series of simulations has been carried out to investigate the influence of the matrix tensile strength on the crack propagation in ECC-materials. In the simulations, the slope of the second part of the cohesive law, a_2, was held constant together with the fracture energy, G_F, while the slope of the first part of the cohesive law, a_1, and the tensile strength, f_t, were varied. The employed cohesive laws are shown in figure 4.5. The fracture energy, G_F, plays a role in determining whether steady-state cracking will prevail, while the tensile strength, f_t, is insignificant according to the criterion for steady-state flat-crack propagation (eq. (2.4)). According to the criteria this means that the four cohesive laws will have an equal change in achieving steady-state cracking. The results from the simulations are shown in figure 4.6 and 4.7.

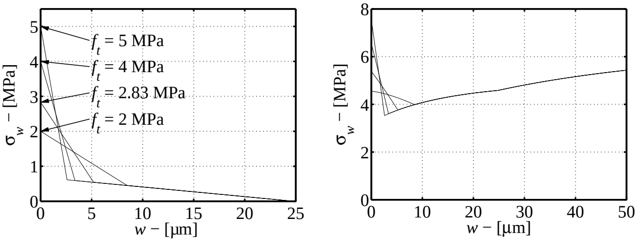

(a) Matrix. (b) ECC.

Figure 4.5 *Average cohesive laws for different tensile strengths, f_t, of the matrix.*

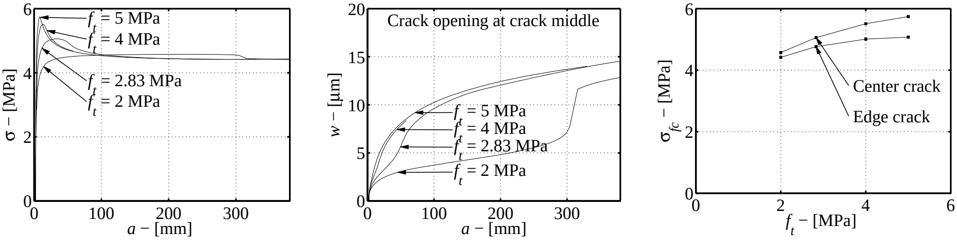

(a) Half crack length, a, and matching far-field stress, σ.

(b) Opening at crack middle, w, and matching half crack length, a.

(c) Relation between first crack strength, σ_{fc}, and the matrix tensile strength, f_t.

Figure 4.6 *Influence of the tensile strength of the matrix, f_t - center crack.*

As shown in figure 4.6(c) an increase in tensile strength, f_t, results in an increase in first crack strength, σ_{fc}, where the increase is most pronounced for center cracks. A small tensile strength results in a small crack opening, w, for small crack lengths (see figure 4.6(b) and 4.7(b)), while the crack openings approach the same level, independent of tensile strength, as the crack length increases. This is due to the fact that the fracture energy, G_F, is fixed and an increase in tensile strength results in a larger part of the fracture energy being associated with the first, very small crack opening (see figure 4.5(a)).

As shown in figure 4.6(b) and 4.7(b), the effect of the tensile strength vanishes for large crack lengths. For crack lengths smaller than 300 mm, the tensile strength of the matrix, and thereby the shape of the cohesive law, has a large influence on the crack opening during crack propagation. The conventional steady-state, flat-crack criterion deals only

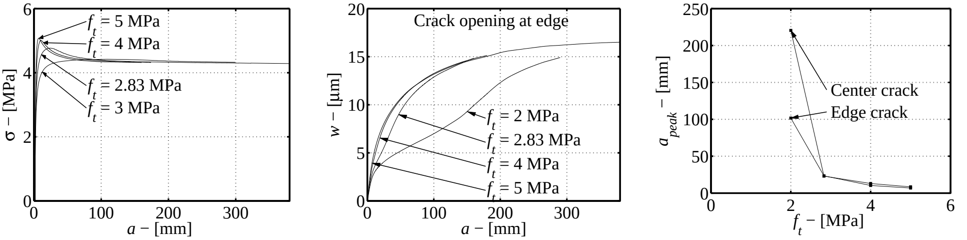

(a) Total crack length, a, and matching far-field stress, σ.

(b) Opening at crack edge, w, and matching total crack length, a.

(c) Relation between the crack length at first crack strength, a_{peak}, and the tensile strength of the matrix, f_t.

Figure 4.7 *Influence of the tensile strength of the matrix, f_t - edge crack.*

with fracture energy and not the shape of the cohesive law, because the criterion is based on LEFM, in which the entire amount of energy is dissipated in a point. This criterion is therefore valid for brittle materials, but because the process zone in this analysis reaches lengths of over 300 mm, the shape of the cohesive law becomes important.

The crack length at peak stress, a_{peak}, is plotted as a function of the matrix tensile strength, f_t, in figure 4.7(c). For an edge crack a_{peak} is defined as the entire crack length while, for a center crack, it is the half crack length. For a matrix with fixed fracture energy, G_F, a low tensile strength, f_t, results in stable crack growth.

4.3.3 Influence of Fiber Type

The complementary energy of the fibers play an important role in the aim of achieving steady-state flat-crack propagation according to the criteria for such propagation (eq. (2.4)). An investigation of the influence that the complimentary energy has on the crack propagation, was carried out in *Paper III.* Here a simulation with a new fiber curve was made. The new fiber curve was derived by scaling the w-axis with a factor 0.5 (see Figure 4.8(a)). The new fiber type will be denoted fiber type 2. In figure 4.8 the applied cohesive laws and the results from the investigation are shown.

Reducing the complementary energy in fiber type 2 leads to a higher first crack strength, σ_{fc}, and smaller crack openings. This can be explained as a cause of the shape of the new fiber curve. The total amount of complementary energy has been reduced for fiber type 2, but for small crack openings the utilized complementary energy is highest for type 2. The increase in first crack strength as a result a reduction of complementary energy is also observed in a test carried out by Li et al. (2002). For neither of the fiber types a direct connection between complementary energy, fracture energy and steady-state

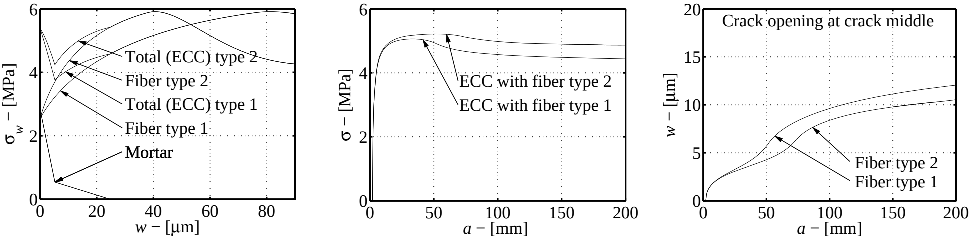

(a) Cohesive laws for fibers and ECC.

(b) Half crack length, a, and matching far-field stress, σ.

(c) Opening at crack middle, w, and matching half crack length, a.

Figure 4.8 *Influence of the fibers. The simulations are for center cracks only.*

flat-crack propagation was found. For fiber type 2 the crack opening has to be higher than 16 μm to utilize complementary in the same amount as the fracture energy. In the simulated interval the crack opening, w, was found to be smaller than 11 μm. Reducing the complementary energy leads to an increase in crack propagation stability according to figure 4.8(b).

4.3.4 Influence of Specimen Geometry

In the previous sections the geometry of the sheets have been infinite. To investigate the influence of finite specimen geometry, six new FEM-models with finite geometries were employed. The material properties in all models were the standard properties (see section 4.1). Similar to the previous FEM simulations, the boundary conditions along both loaded edges resulted in a uniform displacement in the load direction along the breadth. When investigating the influence of the specimen geometry, a finite sheet with the dimensions 30 mm x 80 mm (breadth x height) was taken as a point of reference. These dimensions were chosen to match the dimensions of the instrumented part of test specimens in the JSCE test specimen (JSCE-TC 2005). In figure 4.9(a) and 4.9(b) results for different geometries are shown for a center crack and an edge crack respectively. The center flaws all have a total length, $2a_0$, of 4 mm, while the edge flaws have a total length, a_0, of 2 mm. In figure 4.9(c) the opening at the crack middle is shown for various crack lengths, for both finite and infinite geometries.

As shown in figure 4.9(a) and 4.9(b) the force needed to propagate the crack in the sheet with dimensions 30 mm x 80 mm is smaller than the corresponding force in the sheet with "infinite" geometry (1200 mm x 1000 mm). This observation is true for both center and edge cracks and can be explained by the reduced stiffness, caused by the small breadth in the finite sheet. For center cracks the results are unaffected by increasing the height to 1000 mm and keeping the breadth unchanged. For the edge crack increasing the

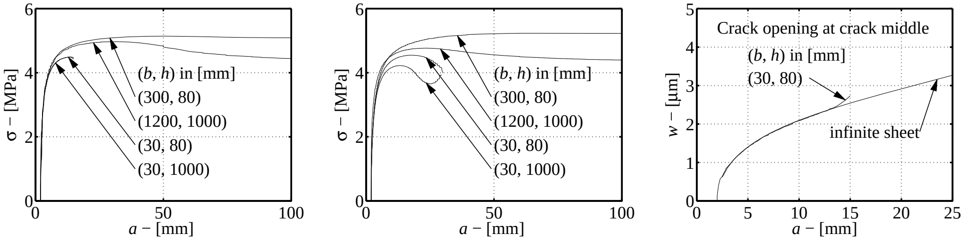

(a) Center crack - Half crack length, a, and matching far-field stress, σ.

(b) Edge crack - Total crack length, a, and matching far-field stress, σ.

(c) Center crack - Opening at crack middle, w, and matching half crack length, a.

Figure 4.9 *Influence of geometry.*

height causes the first crack stress, σ_{fc}, to decrease 7 %. Increasing the distance to the fixed boundaries reduces the stiffness of the model. Due to symmetry in the center crack model it is not sensitive to the change in stiffness. Keeping the height fixed at 80 mm and increasing the breadth to 300 mm, the first crack strength in both models increases, compared to that obtained for a breadth of 30 mm. This is due to the fact that the stiffness is increased and for these dimensions the center crack model is affected as well. In all cases the crack propagation stability increases with increasing first crack strength.

The opening in the crack middle during crack propagation is shown in figure 4.9(c) for an infinite sheet containing a center crack and for a sheet with the dimensions 30 mm x 80 mm. The opening in the crack middle in the finite sheet is identical to the opening in the infinite sheet up to a crack length, a, of 13 mm. After this crack length the opening in the finite sheet becomes larger than the one in the infinite sheet. This was expected due to the stiff boundary conditions and small breadth in the finite specimen. At a crack length, a, of 15 mm in the finite sheet the crack has run through the sheet.

4.3.5 Influence of Boundary Conditions

To investigate the influence of the boundary conditions, a series of FEM simulations have been conducted. Figure 4.10 shows a sketch of the test setup, where the basis is taken from the setup employed by the JSCE-TC (2005). At the end of each bar a hinge is placed (A and B), the rotations of these hinges can be free or fixed. The employed FEM mesh is shown in figure 4.11 (due to symmetry only half the model is shown). The part of the specimen locked in the steel jaws is assumed to be rigid. In the FEM model this part is modeled by a series of rigid bars. From the jaws to the hinges the steel bars have a diameter of d_b. The ECC specimen is modeled with plane stress elements. The employed model has 16 elements along the width in the coarse part and 128 elements in fine part. The fine mesh consists of 10 elements along the height on each side of the symmetry line and each of these elements has a height of 0.63 mm. The model contains a row of cohesive interface elements in the symmetry line, in which the crack can propagate.

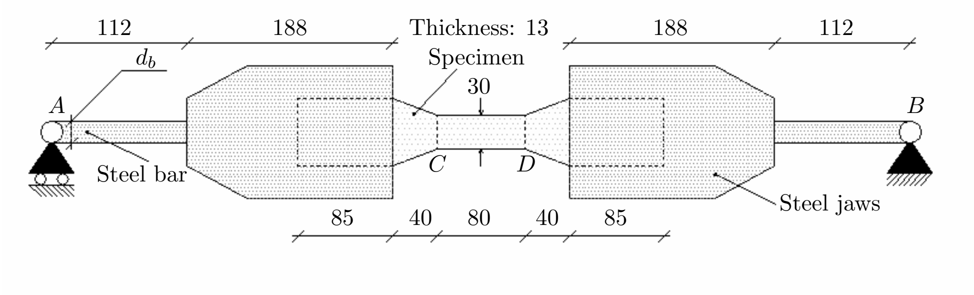

Figure 4.10 *Test setup - all dimensions in [mm].*

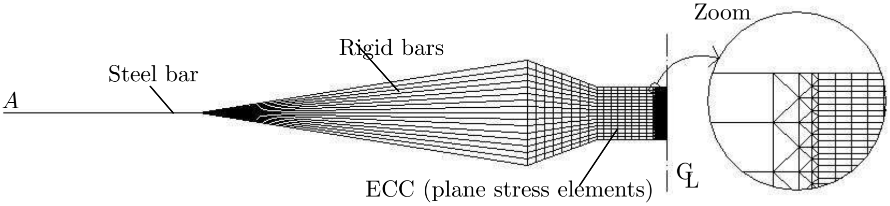

Figure 4.11 *The employed FEM mesh for the dog-bone-specimen.*

The simulations were only made for edge cracks. If a center crack was introduced the model would contain a double symmetry and it would therefore be insensitive to the hinges being free or fixed. In Figure 4.12 matching values for the total crack length, a, and the far-field stress, σ, are plotted. In these plots the far-field stress is the average stress in the section C or D. The results from the rectangular sheet with a width of 30 mm and a height of 80 mm and 1000 mm are plotted for comparison (from the previous section).

As shown in figure 4.12(a) similar results are obtained for the sheet with the dimensions 30 mm x 1000 mm and the fixed boundaries and the dog-bone specimen with the hinges free-free and a bar diameter, d_b, of 20 mm. This can be explained by the reduction of stiffness given by the increased height. As shown in the figure, fixing the rotation in one or both hinges, increases the stiffness and the first crack strength. The first crack strength for the sheet with the fixed boundary conditions is about 8 % higher than the corresponding for the test setup with the hinges free-free. Fixed boundaries is the stiffest setup one can obtain, for a sheet with these dimensions. It was therefore expected that the first crack strength here would be the highest. As shown in the figure, increasing the stiffness of the boundaries, increases the stability of the crack propagation as well.

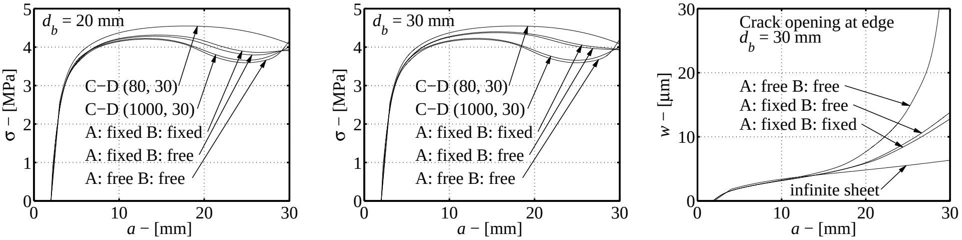

(a) Steel bar diameter, $d_b = 20$ mm.

(b) Steel bar diameter, $d_b = 30$ mm.

(c) Crack opening at the specimen edge, w, and matching total crack length, a. - steel bar diameter, $d_b = 30$ mm.

Figure 4.12 *Total crack length, a, and matching far-field stress, σ. There are 5 simulations for each diameter, d_b: 3 simulations for different adjustments of the hinges (dog-bone-specimens) and 2 simulations where only the part between C and D (see figure 4.11) is modeled and here the loaded boundaries are rigid (these results are taken from Figure 4.9(b))*

In figure 4.12(b) results are shown for simulations employing a bar diameter of 30 mm. As shown in figure 4.12(a) and 4.12(b) the results are unaffected by the diameter of the bars as long as the rotations of the hinges are free-free. Increasing the bar diameter from 20 mm to 30 mm increases the first crack strength approximately 2 % when the hinges are fixed-free or fixed-fixed. As the bar diameter increases, the results get closer to those obtain for the rectangular sheet with the dimensions 30 mm x 80 mm (width x height). In figure 4.12(c) the crack opening, w, at the edge is plotted as a function of the crack length, a, for a bar diameter of 30 mm. The openings are compared to the corresponding opening for an infinite sheet (taken from Figure 4.9(c))). For a crack length up to 13 mm the crack openings in the four simulations are almost identical. For larger crack lengths, the opening at the edges in the dog-bone specimens becomes significantly larger than the corresponding opening in the infinite sheet, thanks to the smaller stiffness in the dog-bone test setup. When at least one hinge is fixed the opening increases with a factor 2.2 compared with the corresponding opening for the infinite sheet for a crack length of 30 mm. When both hinges are free the opening for a crack length of 30 mm increases with a factor 7.7 compared with the opening in the infinite sheet.

4.4 Simulation of Multiple Cracking

On the meso scale II two simulations on a sheet loaded in uniaxial stress were performed in (Dick-Nielsen et al. 2006*b*). Each sheet had a length of 80 mm and a width of 30 mm and the load was applied as a displacement load. Each sheet contained 40 initial stress free flaws with a length of 4 mm. The initial flaws were randomly distributed over the width with a fixed spacing in the load direction (see figure 4.13(a) - an identical distribution was applied in both models). Both models consisted of 8 node quadrilateral plane stress elements. The applied cohesive law for the ECC was identical to that employed in section 4.1 (see figure 4.1). These simulations were very similar to the experimental tests carried out by Wang & Li (2004). In these tests Wang tested an ECC-material with similar properties and added artificial ellipsoidal shaped flaws, where the largest axis had a length of 4 mm, to measure the influence on the strain-hardening capacity. After the test a spacing of approximately 2 mm was measured between the cracks.

The applied mesh in the models can be seen in figure 4.14. In the first model the cracks could propagate in interfaces placed in continuation of the initial flaws. All the plane stress elements were given elastic properties. In the second model smeared cracking was applied. To simplify the simulations, only elements in the middle part of the models were given non-linear material properties (see figure 4.13(a)).

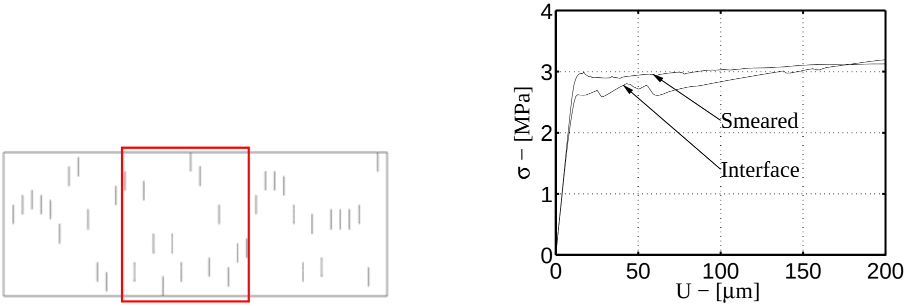

(a) Position of the initial flaws - the box frames the non-linear material area.

(b) Specimen elongation, U, and matching load, σ.

Figure 4.13 *Positions of initial flaws and results.*

In figure 4.13(b) corresponding values to the applied load, σ, and the total deformation, U, are shown and in figure 4.14 a contour plot of the largest principal strains is plotted for the two simulations at a total deformation of 50 μm. The relationship between the applied load and the total deformation of the sheet, obtained from both models, is similar to those Wang observed in his test. First we have a linear elastic branch, and after the first crack strength has been reached, a strain-hardening branch emerges with a low positive slope.

The interface model and the smeared model both have some advantages and some limitations. A comparison between the semi-analytical model and crack growth in interfaces showed, that interface models describe discrete crack growth in cohesive material very well (Stang et al. 2007). The limitation of the interface model is that the crack can only propagate in the interfaces and therefore the cracks can not merge. Merging of cracks is possible in the smeared model. The limitation in this model is that cracks tend to introduce softening in two rows of elements during localization. This causes the smeared

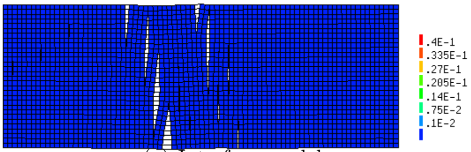

(a) Interface model.

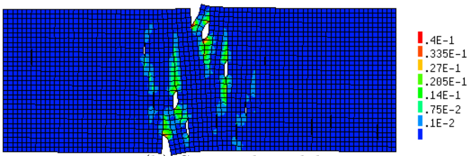

(b) Smeared model.

Figure 4.14 *Principal strains at a total deformation of 50 μm (scale factor 50).*

model to become a little stiffer than intended and that is why the first crack strength for the smeared model is a little higher than the one for the interface model (see figure 4.13(b)). Although identical cohesive laws were given as material data in both models in the non-linear part, the emerged crack patterns are not the same. The two models give two different results, but they both still show an interesting tendency. Although both models were given the uniform material and the initial flaws all had the identical length, the micro cracks were not formed simultaneously and they did not run through the specimen at once. In both models interaction between initial flaws and micro cracks was observed in areas, where the concentration of initial flaws weakened the strength of the material.

4.5 Concluding Remarks

In the present investigation conditions for strain-hardening in ECC-materials have been investigated. The investigation is based on the assumption that matrix crack propagation is adequately described by cohesive fracture mechanics in the form of the FCM, and that a cohesive law for the composite can be constructed through superposition of the matrix cohesive law and the fiber-bridging curve. In the present analysis considering a single crack as well as in the derivation of the steady-state, flat-crack propagation criterion, only the propagation of a single crack is studied.

Through a comparison of the cohesive approach and the theory of LEFM, it was found that the crack openings predicted by both approaches were of the same magnitude. However the far field stress and the sensitivity to initial flaw size were significantly different in the two approaches. For crack length, a, up to 200 mm the crack openings found were less than 20 μm.

The investigation showed that the crack opening alters when changing the dimension of the sheet from infinite to finite, but the magnitude remains unchanged. The Boundary conditions applied to the test specimen, on the other hand, has a larger influence on the crack openings observed during crack propagation, and potentially strain-hardening may be hindered by flexible boundary conditions, thanks to the large crack openings experienced during crack propagation. Still the conclusion is that crack propagation and the maximum fiber-bridging stress are found to be two separate issues, because in most practical cases, the cracks will propagate long before crack openings which are relevant for the maximum fiber bridging are found. Thus care should just be taken in adjusting the first crack strength to be lower than the bridging stress. However it is not possible to predict first crack strength in a simple manner, because it is a complicated function of the parameters involved. Furthermore the few multiple crack simulations carried out, suggest that interacting effects during crack propagation play a major role in the strain-hardening process. It has not been possible to describe these interaction effects in a simple fashion.

The influence of initial flaw sizes, the tensile strength of the matrix and the fiber type have been investigated in a parameter study. It was found that the first crack strength and the evolution of the opening at crack middle are influenced primarily by the cohesive law of the matrix and the fiber-bridging curve, and only weakly by the initial flaw size. Reducing the tensile strength (keeping the fracture energy constant) will promote multiple cracking, since the first crack strength for the ECC-material is reduced. The complementary energy of the fiber-bringing curve was found to have little influence on the multiple cracking potential, as long as the deformation at peak stress on the fiber-bridging curve was kept larger than the maximum crack opening during propagation.

The investigated parameters all had an influence on the stability of crack propagation in the ECC-material. In particular the tensile strength had a pronounced influence on the crack length at first crack strength (peak far field stress). However, the significance of the stability of crack growth and its influence on multiple cracking is not clear and cannot be assessed with the present models.

Chapter 5

Continuum Model on the Macro Scale

The SHFRCC material is characterized by its ability to undergo strain-hardening. This characteristic makes smeared models generally suitable to simulate the material behavior (Dick-Nielsen et al. 2006*b*), and a few smeared models has been derived especially to capture this phenomenon. Han et al. (2003) has derived a total strain, rotating smeared crack model. This model is characterized by its detailed description of the unloading phase, which makes it suitable for cyclic loading simulations. In the SHFRCC model proposed by Kabele (2002), the cracks are fixed when initiated. The model is characterized by the scheme used to describe resistance against relative sliding of crack surfaces. This resistance is assumed to occur solely due to fiber bridging, while fibers are described as randomly oriented Timoshenko beams.

In *Paper IV* and *Paper V* a plasticity-based damage mechanics model for SHFRCC is presented. The present model is based on the smeared fixed, multiple cracking approach. The model differs from existing models by combining a matrix and a fiber description in order to simulate the behavior of the cracks in the SHFRCC-material. The model is meant to be used in the state, where the multiple cracks evolve. In this state the crack openings in PVA-ECC have a magnitude of 100 μm (Fischer et al. 2007). Due to the small openings, the matrix will have an influence on the crack behavior, especially under mode II openings, where dilation effects will appear.

5.1 The Continuum Model

The constitutive equations for the model can be found in *Paper IV*. Here the strain, $\boldsymbol{\varepsilon}$, is split into two parts, one related to the uncracked elastic material, $\boldsymbol{\varepsilon}_e$, and one related to the additional deformations due to opening of cracks, $\boldsymbol{\varepsilon}_{cr}$:

$$\boldsymbol{\varepsilon} = \boldsymbol{\varepsilon}_e + \boldsymbol{\varepsilon}_{cr} \tag{5.1}$$

In this model the behavior of a crack is split into a matrix part and a fiber part (see figure 5.1), where the matrix crack is described through a plasticity model. In general a crack is initiated as the stress reaches the yield-surface according to the plasticity theory. In the current investigations the cohesion is chosen sufficient high, in order for the first crack to be initiated under pure mode I conditions. Due to this the first crack will be perpendicular to the direction of the first principal stress and after initiation the crack direction remains fixed. In figure 5.2 a local coordinate system is shown for a crack.

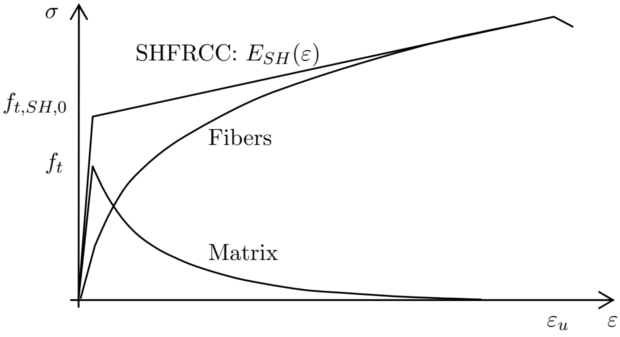

Figure 5.1 *The normal stress in the composite, the normal stress in a matrix crack and the normal fiber-bridging stress as a function of the normal strain in the composite.*

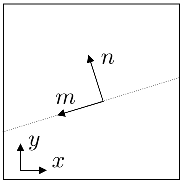

Figure 5.2 *Local coordinate system in crack.*

On the composite-level, the following data are needed for the model (see figure 5.1): the initial E-modulus, E_0, Poisson's ratio, ν, the tensile strength, $f_{t,SH,0}$, a constant, b, that describes the crack opening, at which the crack becomes stress free during unloading, and the threshold angle, ϕ, which limits the angle between two crack systems. This threshold angle should be related to physical observations. In figure 5.1 the uniaxial tensile response for the SHFRCC-material is shown up to localization. In the figure the normal stress in the matrix crack and the fiber-bridging stress on a crack surface are plotted as a function of the normal strain. It is assumed that all cracks in one direction associated with a material point have identical crack opening. Simulations by Dick-Nielsen et al. (2006*b*) have shown that interaction between micro cracks and initial defects leads to a jagged strain-stress relationship, which also is observed in test (Wang & Li 2004). To avoid numerical problems during computations, an idealized smooth curve is employed as shown in figure 5.1. Finally, information about the number of cracks per length, l, in the RVE as a function of the normal strain is needed (see figure 5.3). This relationship will be denoted the crack evolution law and is assumed to be continuous. The length of the RVE, l, should be chosen sufficiently high in order to represent the behavior of the material. The crack evolution law creates a link between the behavior of a single crack, the (δ, σ)-relationship, and the behavior of the continuum, the (ε, σ)-relationship:

$$\boldsymbol{\varepsilon}_{cr} = \boldsymbol{\delta} n \tag{5.2}$$

In the current version the crack evolution law is calibrated through experiments. Examples of micro-mechanical models for the crack evolution law can be found in the literature, see e.g. (Aveston, Cooper & Kelly 1971) and (Wu & Li 1995).

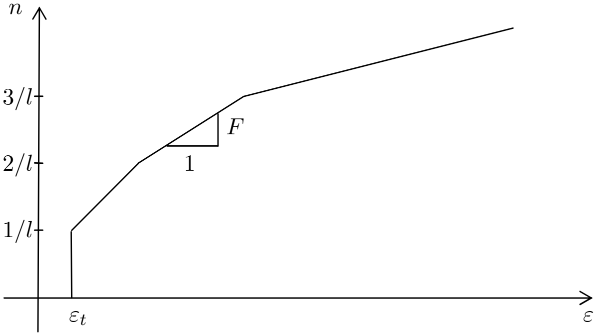

Figure 5.3 *Crack evolution law: strain vs. crack number per length, n.*

For the fibers, only a shear stiffness constant, k, giving the relationship between crack opening tangential fiber-bridging stresses, is needed. This constant depends on the fiber volume fraction, V_f, the shear modulus for the fibers, G_f, and the shape of the fibers (Kabele 2002). The shear stiffness constant can be calibrated through experiments.

The material parameters required for the matrix are the tensile strength, $f_{t,0}$, the cohesion, c_0, two friction coefficients for the yield-surface, μ_f and μ_0, a friction coefficient for the plastic potential, $\mu_{g,0}$, and the mode I and II fracture energy, $G_{F,I}$ and $G_{F,II}$. The mode I fracture energy can be found through a wedge splitting test and inverse analysis (Østergaard, Walter & Olesen 2006) and (Østergaard & Olesen 2006), while the mode II fracture energy is a fitting parameter.

5.2 Matrix Model

A modified version of the concrete model developed by Carol et al. (1997) is employed for the matrix crack. The model is an elasto-plastic material model for damage initiation and propagation. A modified Mohr-Coulomb yield-surface, f, is employed and the cracks are bridged by cohesive stresses. This model is able to capture the dilation effect during sliding of cracks, and therefore it allows the cracks to propagate under mixed mode condition. The dilatation phenomenon is essential, when modeling crack propagation in cementitious materials. If a crack during sliding is confined in the normal direction, large compression stress will be build up. Omitting this phenomenon in a cementitious material model can lead to a wrong estimation of the load carrying capacity of a structural member. The model includes damage parameters and as the damage increases, the shape of the yield-surface will gradually tend towards a point, after which the crack becomes traction free. The matrix stress, $\boldsymbol{s}_m$, can be split up in a normal and a tangential component (s^m_{nn}, s^m_{mn}) and the crack opening, $\boldsymbol{\delta}$, can be split up in the same manner (δ_{nn}, δ_{mn}).

5.2.1 Yield-Surface

In the matrix model, a modified Mohr-Coulomb yield-surfaces closed by a circular yield-surface is employed (see figure 5.4). The modified Mohr-Coulomb yield-surface, f_1, can be written as:

$$f_1 = (s^m_{mn})^2 - (c - s^m_{nn}\mu)^2 + (c - f_t\mu)^2 \tag{5.3}$$

where c is the cohesion, μ is the friction coefficient and f_t is the tensile strength of the matrix. The Mohr-Coulomb yield-surface is closed in compression by a circular yield-surface, to make sure that the crack becomes stress free for large crack openings and to ensure that too large stresses are not build up in compression. The expression for the circle is given as:

$$f_2 = (s^m_{nn} - s_c)^2 + (s^m_{mn})^2 - r^2 \tag{5.4}$$

where s_c is the normal stress in the center of the yield-surface and r is the radius of the yield-surface. The uniaxial compression strength, f_c, can be found, when knowing the normal stress in the center and the radius of the yield-surface. The two yield-surfaces intersect at the normal stress, s', and as shown in figure 5.4 a smooth transition is ensured. This is achieved by letting the center of the circle, s_c, as well as the radius, r, be a function of the material parameters, c, μ, f_t and s'.

The material softens as the crack opens. In the present model the yield-surface can only contract and the contraction will occur as the cracks open and slide. The model

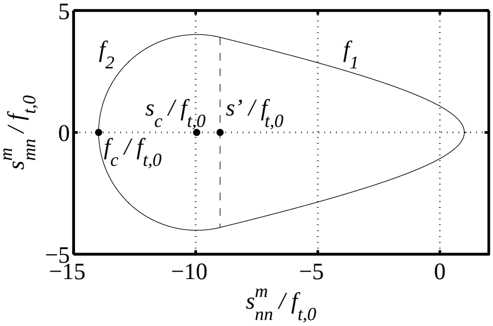

Figure 5.4 *Modified Mohr-Coulomb yield-surface. The transition between the Coulomb surface, f, and the circle surface, f', is marked by a dashed line.*

can be extended by allowing the yield-surface to reestablish partly as a crack closes, and thereby partly reestablish the compression and friction capacity.

5.3 Fiber Model

The mode I fiber-bridging stiffness, e_b, is found through an inverse analysis, based on information about the global stiffness, E_{SH}, for a given normal strain (see figure 5.1), the initial E-modulus for plane stress, $E = E_0/(1-\nu^2)$, the number of parallel cracks per length, n, and the pure mode I stiffness for a given crack opening, $e^m_{nn,I}$. The inverse analysis scheme can be replaced by an analytical fiber-bridging model, giving the relationship between bridging stress and crack opening. The shear stiffness of the fibers is modeled as randomly orientated Timoshenko beam Kabele (2002). The relationship between crack deformations and shear stresses are found from standard solutions:

$$s^b_{nm} = k\frac{\delta_{nm}}{\delta_{nn}} \tag{5.5}$$

where k is a constant calibrated by test, and δ_{nn} and δ_{nm} are the mode I and II opening of the crack.

5.4 Un- and Reloading

In experiments carried out by Kesner & Billington (1998) it was found, that the elastic E-modulus tends to degrade as a function of the largest crack opening obtained. During un- and reloading of the matrix the simple scheme with this degrading of normal stiffness taken into consideration, is employed. The scheme is illustrated in figure 5.5 and written in eq. (5.6):

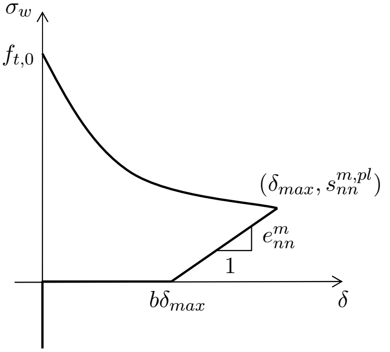

Figure 5.5 *Un- and reloading of matrix.*

$$e_{nn,un}^m = \begin{cases} s_{nn}^{m,pl}/((1-b)\delta_{max}) & \delta_{nn} > b\delta_{max} \\ 0 & b\delta_{max} > \delta_{nn} > 0 \\ \infty & \delta = 0 \end{cases} \tag{5.6}$$

where b, is a constant calibrated by experiments, $s_{nn}^{m,pl}$ is the normal stress before unloading and δ_{max} is the maximal normal crack opening before unloading. During unloading the number of cracks remains constant.

A similar scheme is employed for the fibers in the normal direction. The fibers become elastic, when the normal crack opening decreases:

$$e_{nn,un}^b = \begin{cases} s_{nn}^{b,pl}/((1-b)\delta_{max}) & \delta_{nn} > b\delta_{max} \\ 0 & b\delta_{max} > \delta_{nn} > 0 \end{cases} \tag{5.7}$$

where $e_{nn,un}^b$, is the fiber normal stiffness during unloading and $s_{nn}^{b,pl}$ is the fiber normal stress before unloading. When the crack is closed the normal stress is transferred entirely through the matrix. In the tangential direction the fiber stiffness is modeled as elastic Timoshenko, and eq. (5.5) is therefore still valid during un- and reloading.

5.5 Initiation of Second Crack Direction

The first crack is initiated, when the first principal stress reaches the tensile strength of the SHFRCC-material, $f_{t,SH,0}$. The normal to the crack surface is parallel with the first principal stress and after crack initiation the crack direction remains fixed. An angle threshold limits the angle between two crack systems, and the size of the angle threshold is determined through experiments. A second crack system is initiated, when the stress state in the matrix outside the angle threshold reaches the yield-surface. The normal to the second crack system is parallel to the normal to the yield-surface.

5.6 Simulation of Mixed Mode Crack Opening

The capability of the material model is demonstrated considering the opening of a single crack at a material point (see figure 5.6). The dimension of the RVE associated with the material point is 10 mm x 10 mm (l x l). The load is applied along the upper boundary in two steps. In the first step, a displacement, u_I, perpendicular to the crack surface is applied. This displacement is kept constant in the second load step, while a displacement, u_{II}, in the direction parallel to the crack surface is applied. In figure 5.7 the displacement load as a function of the time increment, t, is shown.

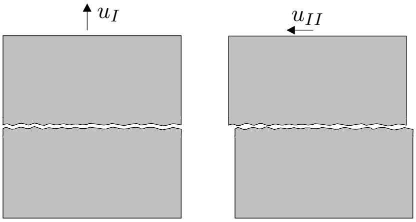

(a) Load I: Pure mode I crack propagation.

(b) Load II: Mixed mode crack propagation.

Figure 5.6 *Opening of a single crack in a RVE.*

5.6.1 Model Input

The material data for the composite-level applied for this simulation are found from a FPB test and an inverse analysis (Østergaard et al. 2006), where the mix proportions are given in table 5.1. The material is an ECC-material, with 2 volume percent PVA-fibers, further detail can be found in *Paper IV.*

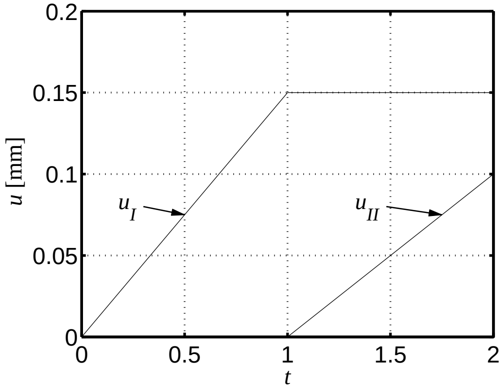

Figure 5.7 *Prescribed displacement, u, as a function of the time increment, t.*

Table 5.1 *Mix proportions of SHFRCC by weight (Østergaard et al. 2006).*

Cement	Sand	Quarts	FA (milled)	FA	Water	SP	Fibers
1.00	0.40	0.40	0.36	0.84	0.54	0.014	0.045

The material data for the matrix were not measured in the experiment and are therefore assumed. Detailed can be found in *Paper IV*.

5.6.2 Simulation Results

In figure 5.8 it is illustrated how the yield-surface tends towards a point, as the material softens. The distribution of normal and tangential stresses in the crack throughout load step I and II is plotted in figure 5.8. In load step I the crack is initiated and opens in pure mode I. In this step, the matrix is only bridged by normal stress and the normal stress is reduced to 39 % of the initial tensile strength, $f_{t,0}$. After the tangential displacement is applied in load step II, compression stresses are builded up in the matrix crack thanks to the dilation effect. After a certain amount of sliding, the dilatation effect wears off and the stresses in the matrix are reduced towards zero.

The crack opening as a function of the time increment, t, is shown in figure 5.9(a). In load step I, only mode I opening occurs in the crack. In load step II, normal as well as tangential opening occurs, where the normal opening is due to the dilatation effect. The normal opening keeps increasing until it becomes smaller than the normal stress at the center of the circle, s_c. Hereafter the dilatation effect wears off and the crack begins to

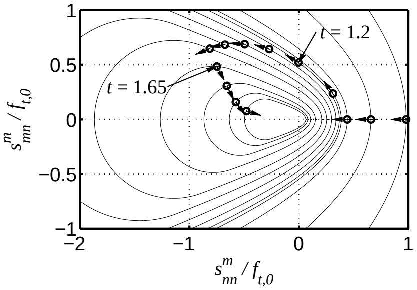

Figure 5.8 *A selection of stress points through the load history are plotted together with the matching yield-surface. The arrows indicate the direction of the stress evolution.*

close.

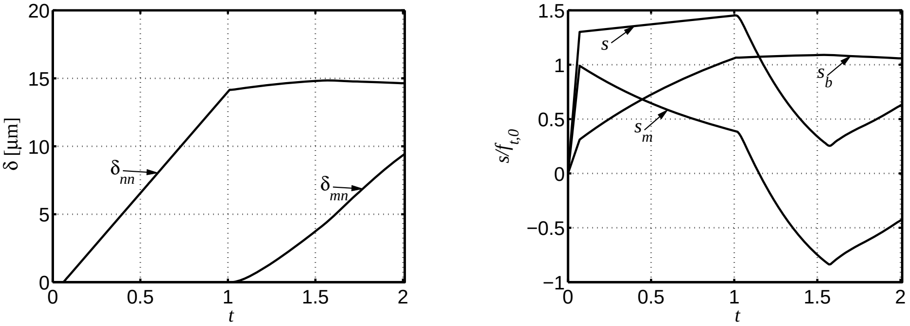

(a) Crack opening as function of the time increment, t.

(b) Normal stress history in the crack as a function of the time increment, t.

Figure 5.9 *Results from the simulation of the crack opening in a RVE.*

The stress history in the crack is plotted in figure 5.9(b) as a function of the time increment, t. In load step I, the crack opens in pure mode I. The difference between the normal stress in the matrix, s_m, and in the composites, s, that is observed at crack initiation, is in good agrement with numerical observations (Dick-Nielsen et al. 2005). In the numerical observations it was found that a crack with an opening of only a few nanometers, runs through the matrix before debonding of the fibers takes place. Similar experimental observations has been made by (Wang & Li 2004). Here a tensile strength of 4 MPa was found for an SHFRCC-material, while experiments carried out by Wang at the Technical University of Denmark, showed that the matrix tensile strength of the SHFRCC-material was 2.8 MPa. After crack initiation in the RVE, the matrix stress,

s_m, decreases, the fiber-bridging, s_b, increases and the normal stresses in the composite have the slope E_{SH}. In the beginning of load step II, the matrix stress decreases thanks to dilatation. As the dilatation effect wears off, the total stress, s, converges towards the fiber stress. The fiber-bridging remains almost constant during sliding, while the matrix stress and thereby the total stress decreases significantly thanks to the dilatation effect. This example demonstrates the importance of having a separate matrix crack and fiber descriptions.

5.7 Four Point Bending Beam Simulation

Østergaard et al. (2006) have carried out FPB experiments with an SHFRCC beam and subsequently have performed an inverse analysis to obtain the strain-hardening curve of the material, where the inverse analysis was based on the hinge model. The dimensions of the beam were: length 500 mm, height 60 mm and width 100 mm as shown in figure 5.10. The beam was simply supported and loaded as shown in the figure. Point A and B were used for measuring of vertical displacement, u, and point C to evaluate the state of the material. In *Paper V*, a simulation of this FPB beam was carried out. The material model was implemented in a user supplied routine in the commercial FEM package 'DIANA'. In contrast to the simulation of the crack opening in a RVE, multiple cracking did occur in the beam. For the simulation only half of the beam was modeled, due to symmetry, and here a 70 by 17 element mesh was employed. The elements employed were 8 node, quadrilateral isoparametric plane stress elements. The elements were based on quadratic interpolation and Gauss integration. The simulation was stopped as the ultimate strain, ε_u, was reached and localization was about to occur.

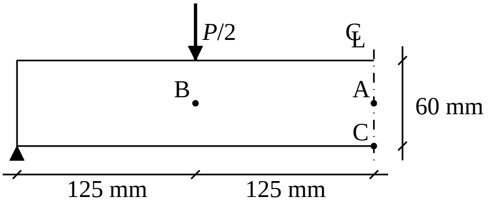

Figure 5.10 *Four point bending beam. Due to symmetry only half the beam was modeled. Point A and B were used to measure a relative deflection, while point C was used to evaluate the state of the material.*

5.7.1 Model Input

The beam was made of the same material as the RVE in the simulation of a single crack (see section 5.6.1). To obtain information about crack opening and spacing from the simulation, information about the number of cracks per length, n, as a function of the total normal strain in the crack normal direction, ε_{nn}, was required (see figure 5.3). Because these data were not measured in the experiment, the following reasonable results were assumed: (ε_{nn}; n [mm^{-1}]), (7.9·10^{-5}; 0.02), (1·10^{-4}; 0.04), (1·10^{-3}; 0.06), (3·10^{-3}; 0.08) and (6·10^{-3}; 0.1). The cracks in the beam mainly opened in mode I, and therefore the matrix parameters only had little influence on the global response like e.g. the displacement.

5.7.2 Simulation Results

In figure 5.11(a) the load-deflection curve from the simulation is plotted, together with the upper and lower bound from the experiments. In contrast with the experiments, a partial unloading was performed in the simulation to demonstrate the capability of the model. The load was applied in three steps: first the load was increased until a deflection of approximately 0.7 mm was reached (load point I), then a partial unloading was performed to load point II and finally the load was increased in the remaining part of the simulation. As shown in the figure, the model was able to reproduce the experimental results very well.

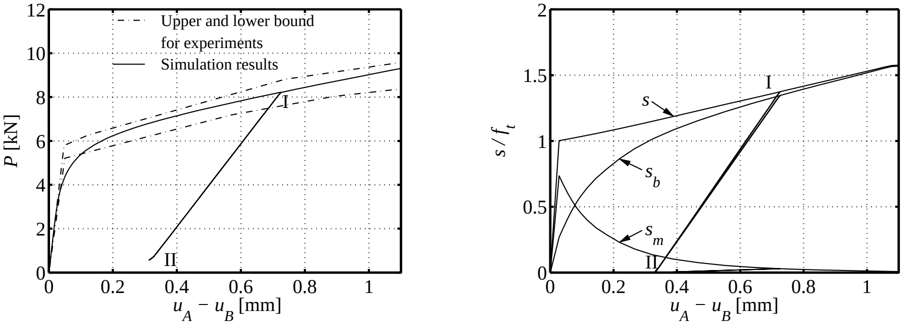

(a) Load deflection curve. The displacement is measured a differential displacement between point A and B.

(b) Total stress, s, fiber-bridging stress, s_b, and matrix stress, s_m, in the normal crack direction at point C vs. deflection.

Figure 5.11 *Results from the FPB simulation.*

In figure 5.11(b) the normal stress, s, at point C is plotted as a function of the relative deflection. The total stress, s, reaches a peak at a relative deflection of approximately 1.1 mm. The unloading scheme works as intended, leaving a permanent plastic deformation after unloading. At a deflection of 1 mm, the matrix has become stress free and the crack is therefore mainly bridged by the fibers.

Figure 5.12 shows the crack pattern at a deflection of approximately 0.9 mm before localization takes place at the bottom of the beam. The line thickness corresponds to the crack opening. Due to the constant bending moment in the middle section, the cracks in this section are almost parallel. The constant bending moment in this section also causes the cracks along the bottom of the section to localize at the same time.

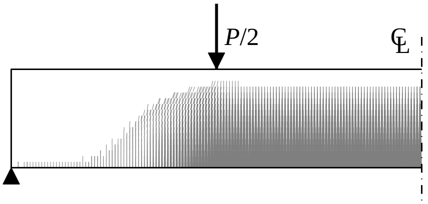

Figure 5.12 *Crack pattern in the beam at a deflection of 0.9 mm. The line thickness corresponds to the crack opening.*

The relationship between the relative deflection and the average normal crack opening, δ_{nn}, at point C is plotted in figure 5.13(a). During unloading from load point I to point II, the average crack opening associated with point C decreases linearly towards zero. At a relative deflection of 1.1 mm, the average crack opening associated with point C is 70 μm, which is a typical magnitude for a SHFRCC specimen before localization takes place (Fischer et al. 2007).

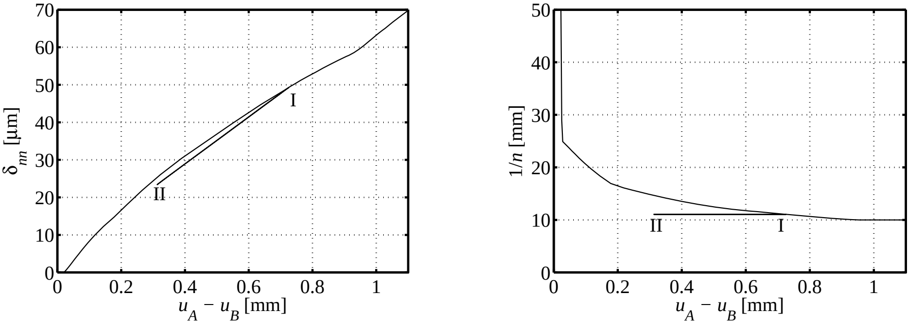

(a) Average crack opening at point C vs. deflection.

(b) Average crack spacing at point C vs. deflection.

Figure 5.13 *Results from the FPB simulation.*

The average crack spacing at point C is plotted as a function of the relative deflection in figure 5.13(b). After the first crack is initiated, the average crack spacing is 50 mm. The spacing decreases until load point I is reached. During unloading from load point I to load point II the deflection decreases, but the crack spacing remains constant. After reloading to load point II the crack spacing decreases until a spacing of 10 mm is reached, after which the spacing remains constant.

5.8 Infill Panels

5.8.1 Introduction

In the United States, steel moment-frame constructions are an often-used construction type. However, brittle failure has been detected in beam-column welded connections during earthquakes. To avoid these brittle failures, it has been suggested by Kesner & Billington (2005) and Olsen & Billington (2007) that constructions should be retrofitted by inserting precast infill panels to increase the stiffness and energy dissipation during seismic loading. The infill panels are bolted into the steel frames, which makes the system highly replaceable if damaged (see figure 5.14). The infill panels are made of SHFRCC; one proposed mix is shown in table 5.2 (Olsen & Billington 2007). The fibers are made of steel, have a length of 30 mm, a diameter of 0.38 mm, and they have a twist at the end to improve pull-out behavior.

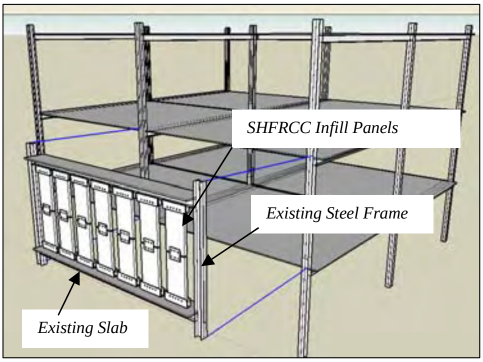

Figure 5.14 *Retrofit schematic (Olsen & Billington 2007).*

Table 5.2 *Mix proportions of SHFRCC by weight (Olsen & Billington 2007).*

Cement	Water	Sand	Fly Ash	Stones 13 mm	SP	Viscous Agent	Steel Fibers
1	0.6	1.7	0.5	1	0.003	0.0095	0.244

Experiments have been performed on a single panel (Olsen & Billington 2007) with a test setup as shown in figure 5.15(a), in which the dimensions of the panel were 914 x 457 x 70 mm (36 x 18 x 2.75 inches). In the construction two panels were bolted together and then bolted to the steel frame, using bolts with a diameter of 25.4 mm. The panel contained a reinforcement web with a bar spacing of 76 mm (3 inches), a bar diameter of 3.3 mm and a perimeter reinforcement with a diameter of 9.5 mm. The U-profiles employed at the top and bottom boundaries of the panel were the two halves of HSS14x4x1/2 (h_1xh_2xt in inches) tube. In the experiments the panel was loaded through a loading arrangement at the top of the panel, which dictated a horizontal displacement, u. The displacement was increased 8 times, starting with a displacement, u_{cycle}, of 0.92 mm and ending with a 27.4 mm displacement. Each load step consisted of three load cycles, where the load was reversed from positive to negative, $\pm u_{cycle}$.

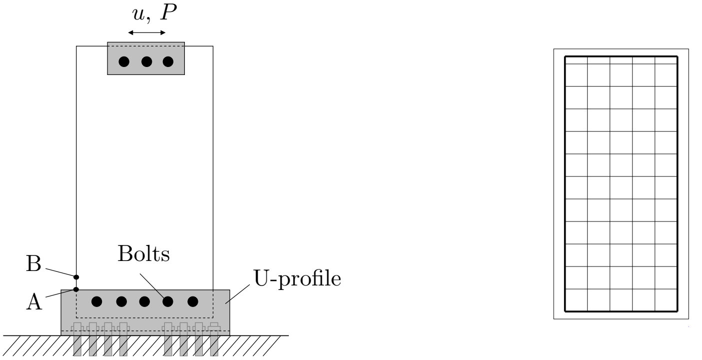

(a) Test setup for infill panel experiments. A and B were points from which the state of the material was analyzed. Point B is located 50 mm above point A.

(b) Reinforcement arrangement.

Figure 5.15 *Infill panel: test-setup and reinforcement arrangement*

A number of uniaxial tensile tests have also been carried out (Olsen & Billington 2007). The specimens in these tests were shaped like a dog-bone, where the center part had the dimensions 203 x 51 x 25 mm (8 x 2 x 1 inches) and the deformations were measured over a length of 175 mm. Figure 5.16(a) shows the results from the uniaxial tensile tests. The same SHFRCC mix was used for all the tensile specimens, but the large scatter can have been caused by a variation in the distribution of fibers. The curve emphasized with the thick line is here used as a reference curve in simulations of the panel behavior. This curve is chosen, because it is located in the lower part of the results. Since the dog-bone specimen was 25 mm thick and the length of the fibers was 30 mm, the fibers are mostly distributed in two dimensions. The panel was 70 mm thick, which results in a fiber distribution close to three dimensions. Three-dimensional fiber distribution results in lower bridging stress than two-dimensional fiber distribution, as has been shown by Lin et al. (1999). Figure 5.16(b) illustrates how the crack evolution law can be found from the uniaxial tensile curve. The crack evolution law gives the relationship between the normal strain, ε_{nn}, and the number of cracks per length, n. In this case the length, l, is the length over which the elongation was measured in the dog-bone specimen (175 mm). It is assumed that a crack is formed each time the stress in the tensile test drops. This is indicated with vertical dashed lines in figure 5.16(b).

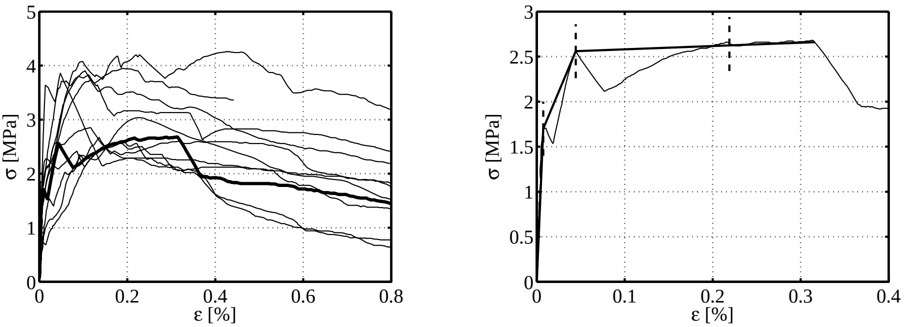

(a) Data from uniaxial tensile curves (Olsen & Billington 2007). The thick one was selected as the reference curve in this investigation.

(b) The uniaxial reference curve from the experiment and the corresponding smooth curve used in the simulation. The dashed lines indicate the points where new cracks are assumed to be initiated.

Figure 5.16 *Relationship between uniaxial tension and normal strain.*

The material model presented here is intended as a tool for the design engineer in the design phase. Once the material parameters are known, information about the behavior of a construction and information about crack opening, orientation and spacing can also be obtained. It is also possible to investigate the effects of material modifications on the structural scale as well as on the material scale (the crack pattern). In the next section, a simulation of the infill panel with the reference material parameters and a parameter study of the influence of matrix and fiber properties will be described. Since the yield surface cannot be reestablished once it has softened, it is not recommended to let the material undergo compression once the cracks are initiated. Therefore the simulations stop, when the cracks close.

5.8.2 FEM model

The FEM model employed is shown in figure 5.17. The elements in gray are the part of the panel that is fixed in the U-profile. The elements employed were 8-node, quadrilateral isoparametric plane stress elements, based on quadratic interpolation and Gauss integration. The reinforcement was modeled using embedded reinforcement elements positioned as shown in figure 5.15(b). The simulations were performed using the commercial finite-element package, DIANA.

The bolts and the bottom of the U-profile act as springs along the lower support when loaded in tension. So four springs were employed to transfer the tensile stresses and a fixed support was employed to transfer the compression stresses as shown in figure 5.17(b).

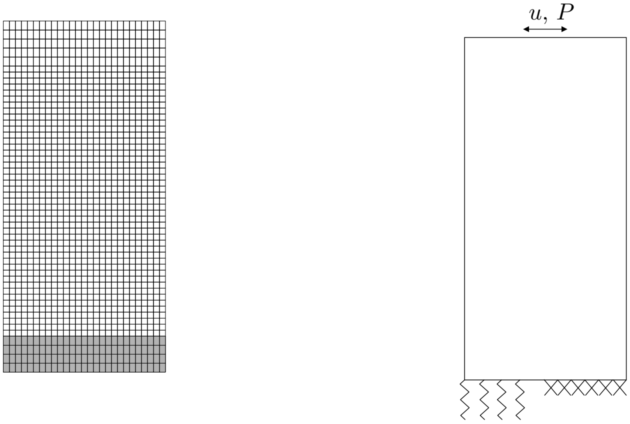

(a) Mesh applied for the FEM model.

(b) Supports applied for the FEM-model. Spring support to the left and fixed support to the right, to simulate bolts and contact pressure.

Figure 5.17 *The mesh and supports applied for the FEM model of the infill panel.*

The four springs were positioned with a spacing, b, of 51 mm (2 inches), which coincides with the distance from bolt center to bolt center. The bottom of the U-profile could be modeled as a series of plates as shown in figure 5.18. The vertical spring stiffness, k, can then be estimated when disregarding the bolt holes and the bolts:

$$k = 192EI/L^3 = 16Ebt^3/L^3 = 300MN/m \tag{5.8}$$

where t is the thickness of the profile, L, the length of the beam and E is Young's modulus for steel. Due to the bolt holes, which reduce the cross-section and the axial stiffness of the bolts, the spring stiffness was set at 200 MN/m.

5.8.3 Material data

The tensile curve employed for the SHFRCC material is shown in figure 5.16(b), where the curve is simplified as a multi-linear strain-stress relationship. The tensile strength, $f_{t,SH,0}$, is 1.7 MPa, Young's modulus, E, is 23 GPa, the ultimate stress, σ_u, is 2.66 MPa, and Poission's ratio ν is set to 0.15. The relationship between normal strain, ε_{nn}, and the number of cracks per length, n, is shown in figure 5.19(b). The unloading parameter, b, is assumed to be 0.5.

The material data for the matrix were not measured in the experiments. To perform

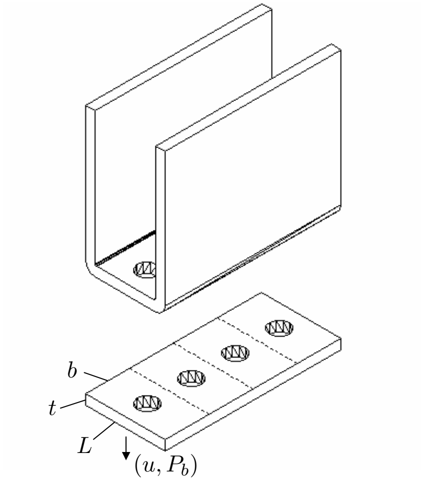

Figure 5.18 *A section of the U-profile and an interpretation of how the bottom of the U-profile can be modeled as a series of parallel beams with the length, L width b and thickness t. Here u and P_b are matching values of the midspan deflection and load transferred through a bolt.*

the simulations the reference material data for the matrix were assumed as follows: the tensile strength, $f_{t,0}$, is 1.6 MPa, the cohesion, c_0, is 5 MPa, the mode I and II fracture energy, $G_{F,I}$ and $G_{F,II}$, are 50 N/m, the friction coefficients, μ_f, μ_0 and μ_g, are 0.2, 0.4 and 0.3, the initial normal stress at the intersection between the Coulomb and the circular yield surface, s_c, is -20 MPa and the constant related to the rate at which the yield circle subtract, a, is -1.

A parameter study investigating the influence of fiber distribution, fiber amount and matrix properties was performed. In the parameter study three variations were made in relation to the reference material parameters. The strain-hardening and evolution curves employed are shown in figure 5.19. The material model is only valid up to the point where localization occurs, so only the part of the strain-hardening curves up to localization is shown. Figure 5.20 shows the relationships between the mode I crack opening and the normal bridging stress.

In variation 1, the reference fiber-bridging curve and matrix properties were kept unchanged (see figure 5.20), while the crack evolution law was modified. The modification gave rise to a larger number of cracks for a given normal strain. The change of crack evolution law could represent better fiber distribution. The larger number of cracks results in a larger normal strain at localization. The stress level of the strain-hardening curve remains unchanged compared with the reference parameters, because only the number of cracks is changed.

In variation 2 the tensile strength, $f_{t,SH,0}$, was increased from 1.7 MPa to 2.0 MPa and the ultimate stress, σ_u, was increased from 2.66 MPa to 5.32 MPa, while the crack evolution law and the matrix properties were kept constant. These changes could represent an increased amount of fibers

In variation 3, the tensile strength, $f_{t,SH,0}$, and the matrix tensile strength, $f_{t,0}$, and fracture energy were all increased compared with the reference parameters, while the crack evolution law was kept unchanged. The fiber-bridging curve in variation 3 was very close to that used in variation 2 (see figure 5.20). The fracture energy of the matrix, G_F, was increased from 50 N/m to 75 N/m, the tensile strength, $f_{t,0}$, from 1.6 MPa to 3.2 MPa, and the resulting tensile strength from 1.7 MPa to 3.5 MPa.

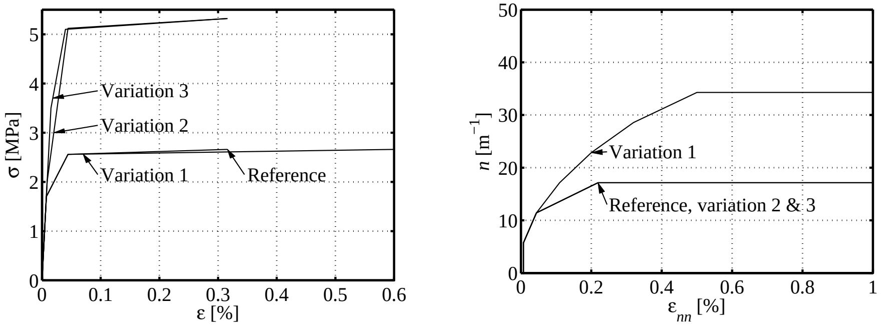

(a) Strain-hardening curves.

(b) Crack evolution laws: number of cracks per length, n, as a function of the normal strain, ϵ_{nn}.

Figure 5.19 *Material curves for the parameter study.*

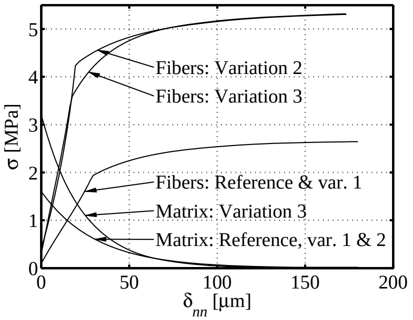

Figure 5.20 *Stress separation curves for matrix and fiber-bridging curves.*

5.8.4 Results and discussions

The load-deformation curves for the four simulations are shown in figure 5.21. The load-deformation curves for the reference material parameters and for material variation 1 are all most identical due to the very similar strain-hardening curves. Since the stress level is increased in the strain-hardening curves in variation 2 and 3 the load, P, is increased as well.

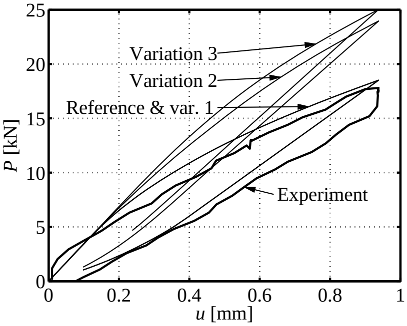

Figure 5.21 *Comparison of one loop for experiment and simulation. The experimental results are from (Olsen & Billington 2007).*

Figure 5.22 shows the crack pattern for the four simulations, and figure 5.23 shows contour plots of the crack openings at a deformation, u, of 0.92 mm. Each element contains four integration points at which information about average crack opening, orientation and spacing was calculated. In the figure, only the crack with the largest opening in each element is plotted. Figure 5.24 illustrates the crack pattern observed in the experiment during the different load stages. The simulations only cover a drift of 0.1 %, where the drift is measured as the displacement, u, divided with the height of the specimen. At this drift, no visible cracks were observed in the experiment. In the simulation with the reference material parameters, most crack openings are less than 50 μm and therefore not visible for the naked eye. The crack pattern observed in the simulation matches that found in the experiment in the final load step, where the localization occurs at the bottom left-hand corner. The crack pattern found in the simulation with material variation 1 resembles the pattern found with the reference material parameters. The size of the damaged area and the orientation of the cracks resemble the reference pattern, due to a similar stress level of the strain-hardening curve and a matching tensile strength, $f_{t,SH,0}$. The crack openings differ due to the difference in the crack evolution laws. Figure 5.22(c) shows the crack pattern for the simulation with material variation 2. The size of the damaged area here is a little larger than the reference. The increase in the stress level in the strain-hardening curve results in a larger crack opening at the bottom of the panel and smaller crack openings in the rest of the panel. Finally figure 5.22(d) shows the crack pattern for the panel employing material variation 3. Compared to the reference material parameters the tensile strength, $f_{t,SH,0}$, is increased from 1.7 MPa to 3.5 MPa. Due to this increase the size of the damaged area is considerably reduced. The crack openings in the damaged area are similar to those observed for variation 2.

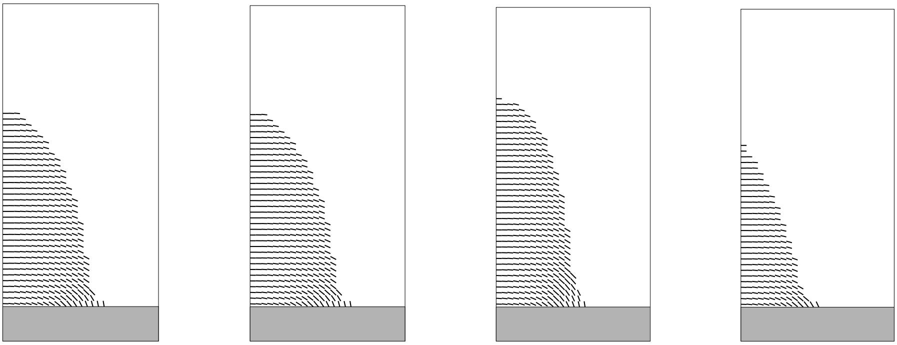

(a) Cracks in the reference panel.

(b) Cracks in the panel: parameter variation 1.

(c) Cracks in the panel: parameter variation 2.

(d) Cracks in the panel: parameter variation 3.

Figure 5.22 *Crack orientation in the simulations of the infill panels.*

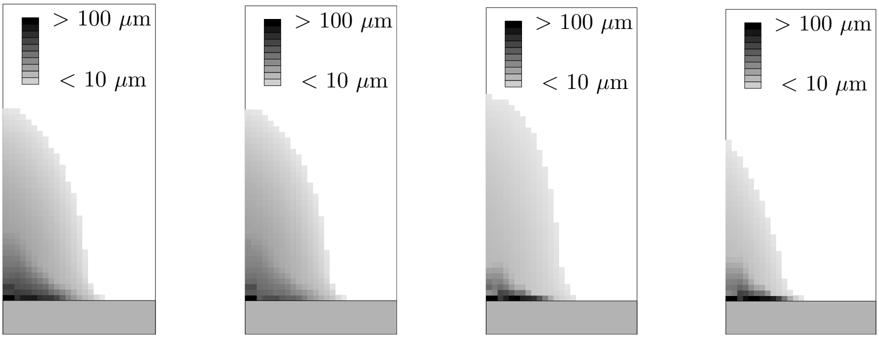

(a) Cracks in the reference panel.

(b) Cracks in the panel: parameter variation 1.

(c) Cracks in the panel: parameter variation 2.

(d) Cracks in the panel: parameter variation 3.

Figure 5.23 *Crack opening in the simulations of the infill panels.*

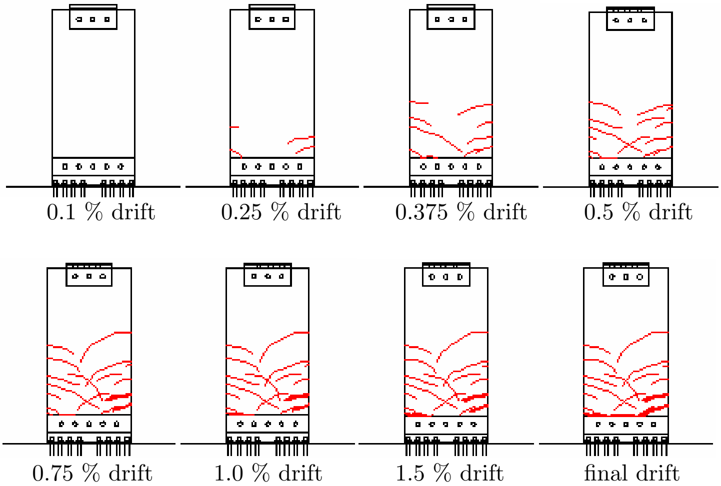
0.1 % drift 0.25 % drift 0.375 % drift 0.5 % drift

0.75 % drift 1.0 % drift 1.5 % drift final drift

Figure 5.24 *Observed cracks in the experiment (Olsen & Billington 2007).*

Figure 5.25 illustrates the normal stresses in the matrix and fibers as a function of the normal crack opening at points A and B respectively (see figure 5.15(a)) for the four simulations. For the panel with the reference material parameters, the average crack opening at points A and B is 185 μm and 61 μm respectively at a horizontal displacement, u, of 0.92 mm. Variation 1 has a better fiber distribution, but maintains the same material data results in a reduced crack opening at point A from 185 μm to 115 μm and at point B the crack opening is reduced from 61 μm to 53 μm. A better distribution of fibers and therefore the appearance of more cracks, results in a larger strain capacity and less visible cracks. In variations 2 and 3, the fiber-volume ratio is increased, which results in an increased stress level in the strain-hardening curve. The increased fiber volume ratio results in crack openings of the same magnitude as was the case for material variation 1 at point A, while the crack openings at point B are reduced by a factor of 2.

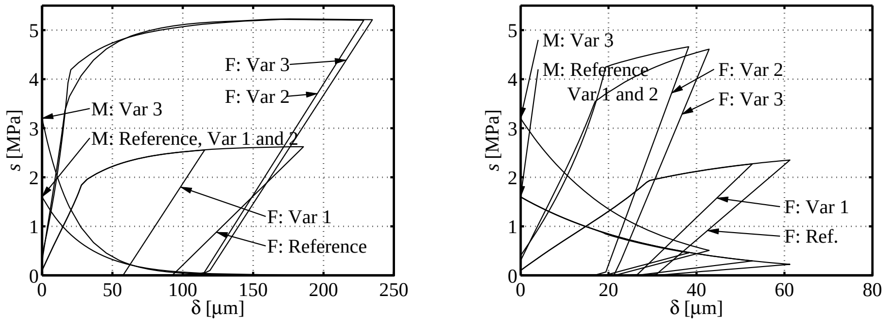

(a) Normal stresses at point A.

(b) Normal stresses at point B.

Figure 5.25 *Normal stresses in the matrix (M) and the fiber-bridging (F) stresses.*

Figure 5.26 shows the average crack spacing at points A and B respectively for the four simulations. The crack evolution law shown in figure 5.19(b) for the reference material was derived using the data from the uniaxial tensile test for the dog-bone specimen (see figure 5.16(b)). The elongation of the dog-bone specimen was measured over a length of 175 mm. At the instance the tensile strength is reached in the panel, it is assumed that the average crack distance is 175 mm. The next cracks are then initiated continuously until a normal strain of 0.22 % is reached (see figure 5.16(b)), and for increasing normal strain the number of cracks associated with one integration point remains constant. Figure 5.26(a) shows that the number of cracks in the panel with the reference material parameters remains constant after a displacement, u, of 0.59 mm. At this displacement, the average crack spacing is 58 mm. In the experiments a crack spacing of approximately 30-50 mm was measured at the final drift. At point B in the simulation, the maximal number of cracks has not yet been reached at a displacement of 0.92 mm. The average crack distance at this point is 77 mm. In variation 1, the average crack distance is reduced from 58 mm to 34 mm at point A, and before unloading the number of cracks has not yet reached a constant level. In variation 2 the tensile strength, $f_{t,SH,0}$, is increased from 1.7 MPa to 2 MPa. This increases the displacement, u, at which the first crack is initiated compared to the panel with the reference material parameters. The higher stress level in the strain-hardening curve results in reduced crack spacing due to an unchanged crack evolution law. At a displacement, u, of 0.62 mm, the number of cracks associated with one integration point reaches a constant level. In variation 3 the tensile strength, $f_{t,SH,0}$, is increased from 1.7 MPa to 3.5 MPa, which is why the first crack at point A is initiated at a displacement, u, of 0.22 mm compared to a displacement of 0.12 mm in the panel with the reference material parameters. The crack spacing reaches a level similar to that obtained for variation 2 and the reference case at a deformation, u, of 0.92 mm. Common for all the simulations is that the crack spacing has not yet become constant at point B before unloading.

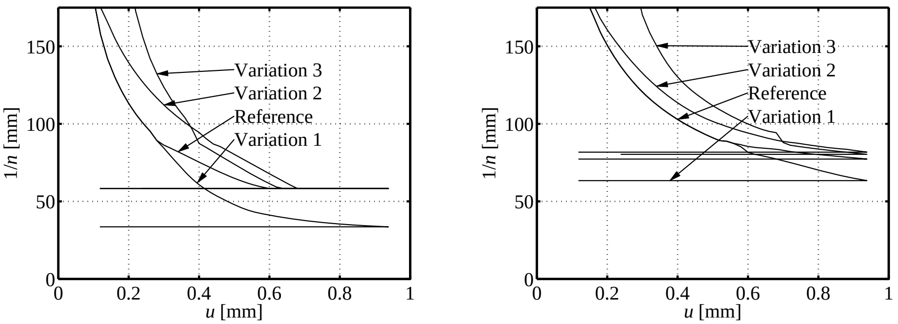

(a) Point A. (b) Point B.

Figure 5.26 *Average displacement between cracks.*

5.9 Concluding Remarks

In *Paper IV* a plasticity-based damage mechanics model for Strain-Hardening Fiber Reinforced Cementitious Composites (SHFRCC) has been introduced. The present model differs from existing models by combining a matrix crack model and a fiber-bridging model to describe the behavior of the SHFRCC material. Apart from information about the stress and deformation state, the model provides information about crack orientation, opening and spacing. The information provided by the model makes it possible to assess the state of an SHFRCC-structure in the state where the multiple cracks evolve.

A demonstration of the model has been performed, by simulating the behavior of a single crack in a RVE made of SHFRCC. This simulation demonstrated the need to separate the matrix crack and fiber-bridging behavior very well. During sliding of a crack the change in fiber stresses was insignificant, but thanks to the dilatation effect, the matrix and thereby the overall stresses were significantly decreased.

The capability of the model is demonstrated on the structural level in *Paper V*, by simulating the behavior of a FPB beam and an infill panel. The results obtained from the FPB beam simulation agreed to a large extent with the experimental results, and detailed information of the crack pattern was obtained.

In the simulation of the infill panel with the reference material parameters, good agreement between the simulation results and experimental observation was reached. A parameter study of the fiber and matrix properties showed that with relatively moderate changes it is possible to design the crack pattern as desired.

The present version of the model is limited to handling the initial crack system, where no cracks localize. Furthermore, the yield surface is not allowed to reestablish as the crack closes. This means that if a stress-free crack closes, then it is not able to transfer compression or friction stresses.

Chapter 6

Conclusion

The main aim of the present thesis has been to derive an ECC-material model and implement it in a Finite Element Method (FEM) program. The work is divided into three scales: On the micro scale it has been investigated whether crack propagation was best described by Linear Elastic Fracture Mechanics (LEFM) or a cohesive approach. Furthermore the fiber debonding process was analyzed. On the meso scale, the conditions leading to multiple cracking were studied and on the macro scale a material model for the ECC-material was derived.

The investigation of the micro scale showed that, when using a cohesive approach the size of the process zone proved large compared with the initial flaws. For this reason LEFM could not be used to simulate crack propagation in the ECC-matrix and the cohesive approach: the *fictitious crack model* was adopted in the remaining part of the thesis. Furthermore the investigation showed that the first crack strength was only weakly influenced by the sizes of the initial flaws, when employing the cohesive approach, which complies to experimental observations and is in contrast with what was predicted by LEFM.

Furthermore on the micro scale, it was examined whether superposition of average cohesive laws was valid in order to arrive at a cohesive law for the ECC-material. Special attention was given to the Cook/Gordon effect, where the fiber-matrix interface could start debonding, thanks to a tensile stress-field in front of a matrix crack. The investigation was limited to matrix-crack propagation perpendicular to the fiber. With this limitation it was found that superposition was valid for small crack openings. This was mainly due to the matrix-crack propagating around the fiber, before significant debonding in the fiber-matrix interface took place.

On the meso scale, conditions under which matrix cracks propagate have been investigated. In the present investigation as well as in the derivation for the steady-state, flat-crack criterion, only one crack was studied. It was found that the crack opening during crack propagation was less than 20 μm for crack lengths up to 400 mm. Thus the crack propagation in ECC and the maximum fiber-bridging stress were found to be two separate issues. Insuring that the first crack strength is lower than the maximum fiber-bridging stress is therefore important if strain-hardening is desired. However there is no simple way to predict the first crack strength, because it depends on many coupled parameters. The few simulations with specimens containing multiple cracks indicated, that the interaction between micro cracks played a major role on the strain-hardening. However a simple description of this can not be found thanks to the many phenomena involved. A parameter study showed that the first crack strength and the evolution of the opening in the crack middle were influenced primarily by the cohesive law of the matrix and the fiber bridging curve, and only weakly by the initial flaw size. Multiple cracking could be promoted, reducing the matrix tensile strength (keeping the fracture energy) since the first crack strength for the ECC-material was then reduced. Furthermore it was found that reducing the tensile strength lead to a more stable crack growth. In contrast to what was stated in the steady-state, flat-crack criterion, it was found that the complementary energy of the fiber-bridging curve only had a weak influence on the crack propagation of a single crack.

A material model for the ECC-material was derived on the macro scale. The model differs from existing models by combining a matrix and a fiber description. The model is based on smeared cracking and the matrix is described using a plasticity model including damage parameters. Where existing models provide information about the stress level, deformations and crack orientation, this model provides additional information about crack opening and spacing. These additional pieces of information are important for engineers when assessing the state of a construction in the state, where the multiple cracks evolve. The capability of the material model was demonstrated in three examples, where the need to separate the model in a fiber part and a matrix part was neatly demonstrated in the simulation of a single crack. During sliding, the change in fiber stresses remained constant, while the matrix stresses decreased significantly, thanks to dilatation in the crack. The results obtained from the four point bending beam simulation, agreed very well with the experimental results. This example demonstrated how information about crack spacing and opening can be extracted from the simulation.

Finally a demonstration of the ECC-model was performed on the construction level by simulating the behavior of a Four Point Bending (FPB) beam and an infill panel both made of ECC-material. The results obtained from the simulation of the FPB beam agreed well with the experimental results. In addition to global stresses and deformations, information about crack traction, opening, orientation and spacing was obtained. In the simulation of the infill panel good agreement between the simulation results and the experimental observation was reached as well. A parameter study of the fiber and matrix properties for the infill panel showed, that with relative moderate changes it was possible to design the crack pattern as desired.

6.1 Recommendations for Future Work

The study of superposition of average cohesive laws on the micro scale was limited to crack propagation in the matrix perpendicular to the fiber, and the model only contained a single fiber. An interesting extension of this analysis would be to have multiple fibers in one model. Furthermore an expanded analysis should cover fibers inclined to the matrix crack. If the model contains inclined fiber, it is important that it is able to capture spalling as well, because this phenomenon is often observed in connection with inclined fibers.

On the meso scale, the conditions for strain-hardening were investigated. The investigation was mainly limited to specimens containing a single crack. Only two simulations contained multiple cracking. The preliminary results from the multiple cracking simulations encourage a further investigation of the interaction between cracks and micro defects during strain-hardening.

The material model for the ECC-material, developed for the macro scale, is capable of handling crack initiation and opening and sliding of the cracks. As the cracks open, the yield-surface tends towards a Mohr-Coulomb yield-surface. If unloading occurs and the cracks close, the yield-surface remains unchanged. A more realistic behavior would be achieved if the yield-surface was allowed to expand and thereby partly reestablishing the frictional behavior of the cracks. Another extension of the model would be to incorporate the behavior of the cracks, as localization occurs. The current version is limited to the state, where the multiple cracks evolve.

Bibliography

ASCE (2005), 'Us infrastructure report card', *www.asce.org/reportcard/2005/index.cfm* .

Aveston, J., Cooper, G. A. & Kelly, A. (1971), *Single and multiple fracture - The Properties of Fibre Composites*, National Physical Laboratory (IPC Science and Technology Press Ltd), pp. 15–24.

Barenblatt, G. I. (1962), 'The mathematical theory of equilibrium cracks in brittle fracture', *Adv. Appl. Mech.* (7), 56–129.

Bazant, Z. P. & Oh, B. H. (1983), 'Crack band theory for fracture of concrete', *Materials and Structures* **16**(93), 155–177.

Carol, I., Prat, P. C. & López, C. M. (1997), 'Normal/shear cracking model: Application to discrete crack analysis', *Journal of Engineering Mechanics* **123**(8), 765–773.

Cook, J., Gordon, J. E., Evans, C. C. & Marsh, D. M. (1964), 'A mechanism for the control of crack propagation in all-brittle systems', *Proc. Roy. Soc* **2282 A**, 508–520.

Cox, B. & Marshall, D. (1994), 'Concepts in the fracture and fatigue of bridged cracks', *Acta Metallurgica et Meterialia* **42**, 341–363.

Dick-Nielsen, L., Poulsen, P. N., Stang, H. & Olesen, J. F. (2004), Semi-analytical cohesive crack model for the analysis of first crack strength of mortar, *in* A. Eriksson, J. Månsson & G. Tibert, eds, 'Proc. of the 17^{th} Nordic Seminar on Computational Mechanics', pp. 183–186.

Dick-Nielsen, L., Stang, H. & Poulsen, P. N. (2005), Micro-mechanical analysis of fiber reinforced cementitious composites using cohesive crack modeling, *in* O. M. Jensen, M. Geiker & H. Stang, eds, 'Knud Hojgaard Conference on Advanced Cement-Based Materials', pp. 277–292.

Dick-Nielsen, L., Stang, H. & Poulsen, P. N. (2006*a*), Condition for strain-hardening in ECC uniaxial test specimen, *in* M. S. Konsta-Gdoutos, ed., 'Measuring, Monitoring and Modeling Concrete Properties', Springer, Alexandroupolis, Greece, pp. 41–47.

Dick-Nielsen, L., Stang, H. & Poulsen, P. N. (2006*b*), Simulation of strain-hardening in ECC uniaxial test specimen by use of a damage mechanics formulation, *in* H. M.

G. Meschke, R D. Borst & N. Bicanic, eds, 'EURO-C 2006 Computational Modelling of Concrete Structures', pp. 319–328.

Dick-Nielsen, L., Stang, H. & Poulsen, P. N. (2007*a*), 'Conditions for strain-hardening in ECC uniaxial test specimen', *Journal of Engineering Mechanics* p. submitted.

Dick-Nielsen, L., Stang, H. & Poulsen, P. N. (2007*b*), 'Micro-mechanical analysis of fiber reinforced cementitious composites using cohesive crack modeling', *Journal of Advanced Concrete Technology* p. accepted.

Dick-Nielsen, L., Stang, H. & Poulsen, P. N. (2007*c*), 'A plastic damage mechanics model for strain-hardening fiber reinforced cementitious composite, part i: Theory', *Journal of Engineering Mechanics* p. submitted.

Dick-Nielsen, L., Stang, H. & Poulsen, P. N. (2007*d*), 'A plastic damage mechanics model for strain-hardening fiber reinforced cementitious composite, part ii: Simulations', *Journal of Engineering Mechanics* p. submitted.

Dugdale, D. S. (1960), 'Yielding of steel sheets containing slits', *J. Mech. Phys. Solids* (8), 100–104.

Fischer, G. & Li, V. C. (2002), 'Effect of matrix ductility on deformation behavior of steel-reinforced ECC flexural members under reversed cyclic loading conditions', *ACI Strucstural Journal* (99), 781–790.

Fischer, G., Stang, H. & Dick-Nielsen, L. (2007), Initiation and development of cracking in ECC materials: Experimental observations and modeling, *in* G. F. A. Carpinteri, P. Gambarova & G. P. (eds), eds, 'High Performance Concrete, Brick-Masonry and Environmental Aspects', Vol. 3, Ia-FraMCos, Taylor & Francis, pp. 1517–1522.

Griffith, A. A. (1920), 'The phenomena of rupture and flow in solids', *Phil Trans Roy Soc London* (A221), 163–198.

Han, T. S., Feenstra, P. H. & Billington, S. L. (2003), 'Simulation of highly ductile fiber-reinforced cement-based composite components under cyclic loading', *ACI Structural Journal* **100**(6), 749–757.

Hillerborg, A., Modeer, M. & Petersson, P. E. (1976), 'Analysis of crack formation and crack growth in concrete by means of fracture mechanics and finite elements', *Cem. Concr. Res.* (6), 773–782.

JSCE-TC, . (2005), *Tentative Guideline for Design and Constructions of Engineering Cementitious Composites-ECC. (Draft)*, Concrete Engineering Series 64.

Kabele, P. (2000), Assesment of structural proformance of engineered cementitious composite by computer simulations, Technical report, Czech University in Prague.

Kabele, P. (2002), 'Equivalent continuum model of multiple cracking', *Engineering Mechanics (Association for Engineering Mechanics, Czech Republic)* **9 (1/2)**, 75–90.

Kabele, P. (2004), 'Linking scales in modeling of fracture in high performance fiber reinforced cementitious composites', *Fracture Mechanics of Concrete Structures, IaFraMCos* .

Kabele, P. & Kanakubo, T. (2007), Experimental and numerical investigation of shear behavior of PVA-ECC in structural elements, *in* 'HPFRCC 5 - High Performance Fiber Reinforced Cementitious Composites'.

Kabele, P. & Stemberk, M. (2005), Stochastic model of multiple cracking process in fiber reinforced cementitious composites, *in* V. C. L. H. M. S. P. S. B.I.G Barr, G. Ferro & J. G. M. van Mier, eds, '11th International Conference on Fracture', Vol. Topic 07 - Full paper on CD, ICF, p. 289.

Kachanov, L. M. (1958), 'Time of the rupture process under creep conditions', *Izvestija Akademii Nauk SSR, Otdelenie Techniceskich Nauk* **8**, 26–31.

Kanakubo, T., Shimizu, K., Katagiri, M., Kanda, T., Fukuyama, H. & Rokugo, K. (2006), Tensile characteristics evaluation of DFRCC round robin test results by JCI-TC, *in* G. Fisher & V. C. Li, eds, 'International Rilem Workshop on High Performance Fiber-Reinforced Cementitious Composites (HPFRCC) in Structural Applications', RILEM Publications S.A.R.L., pp. 27–36.

Karihaloo, B. L. (1995), *Fracture Mechanics and Structural Concrete*, Concrete Design and Construction Series, Longman Scientific and Technical, Harlow, Essex, England.

Kesner, K. E. & Billington, S. L. (1998), 'Investigation of ductile cement based composites for seismic strengthening and retrofit', *Concrete Research and Technology* pp. 19–33.

Kesner, K. E. & Billington, S. L. (2005), 'Investigation of infill panels made from engineered cementitious composites for seismic strengthening and retrofit', *Journal of Structural Engineering - ASCE* **131**(11), 1712–1720.

Kim, Y. Y., Fischer, G. & Li, V. C. (2004), 'Performance of bridge deck link slabs designed with ductile engineered cementitious composite', *ACI Structural Journal* **101**(6), 792–801.

Leung, C. K. Y. & Chi, J. (1995), 'Crack-bridging force in random ductile fiber brittle matrix composites', *Journal of Engineering Mechanics* **121**(12), 1315–1324.

Leung, C. K. Y. & Li, V. C. (1992), 'Effect of fiber inclination on crack bridging stress in brittle fiber reinforced brittle matrix composites', *Journal Mech. Phys. Solids* **40**, 1333–1362.

Li, V. C. (1992), Performance driven design of fiber reinforced cementitious composites, *in* R. N. Swamy, ed., 'Proc. of 4th RILEM International Symposium on Fiber Reinforced Concrete', Chapman and Hall, pp. 12 – 30.

Li, V. C. (1998), Engineered cementitious composites - tailored composites through micromechanical modeling, *in* A. N. Banthia, A. Bentur & A. Mufti, eds, 'Fiber Reinforced Concrete: Present and the Future', Canadian Society for Civil Engineering, Montreal, pp. 64–97.

Li, V. C. (2003), 'On engineered cementitious composites (ECC) - a review of the material and its applications', *Journal of Advanced Concrete Technology* **1**(3), 215–230.

Li, V. C. & Leung, C. K. Y. (1992), 'Steady state and multiple cracking of short random fiber composites', *ASCE Journal of Engineering Mechanics* **188**, 2246–2264.

Li, V. C. & Liang, E. (1986), 'Fracture processes in concrete and fiber reinforced cementitious composites', *Journal of Engineering Mechanics* **112**, 566–586.

Li, V. C. & Maalej, M. (1996), 'Toughening in cement based composites. part i: Cement, mortar and concrete', *Cement and Concrete Composites* **18**, 223–237.

Li, V. C. & Stang, H. (1997), 'Interface property characterization and strengthenng mechanisms in fiber reinforced cement based composites', *Advn Cem Bas Mat* **6**, 1–20.

Li, V. C., Stang, H. & Krenchel, H. (1993), 'Micromechanics of crack bridging in fiber reinforced concrete', *Materials and Structures* **26**, 486–494.

Li, V. C. & Wang, S. (2005), Supression of fracture failure of structures by composites design based on fracture mechanics, *in* V. C. L. H. M. S. P. S. B.I.G Barr, G. Ferro & J. G. M. van Mier, eds, '11th International Conference on Fracture', Vol. Topic 07 - Full paper on CD, ICF, p. 295.

Li, V. C., Wu, C., Wang, S., Ogawa, A. & Saito, T. (2002), 'Interface tailoring for strain-hardening polyvinyl alcohol-engineered cementitios composite (PVA-ECC)', *ACI Materials Journal* **99**(5), 463–472.

Lin, Z., Kanda, T. & Li, V. C. (1999), 'On interface property characterization and performance of fiber-reinforced cementitious composites', *Concrete Science and Engineering* **1**, 173–184.

Löfgren, I., Stang, H. & Olesen, J. F. (2003), 'Fracture properties of FRC determined throug inverse analysis of wedge splitting and three-point bending test', *Journal of Advanced Concrete Technology* **1**(3), 423–434.

Maalej, M., Li, V. C. & Hashida, T. (1995), 'Design and structural applications of stress-crack width relations', *Journal OF Engineering MEchanics* **8**, 903–913.

Marshall, D. B. & Cox, B. N. (1988), 'A j-integral method for calculating steady-state matrix cracking stresses in composites', *Mech. Mat.* **8**, 127–133.

Mechtcherine, V. & Schulze, J. (2006), Testing the behavior of strain hardening cementitious composites in tension, *in* G. Fisher & V. C. Li, eds, 'International Rilem Workshop on High Performance Fiber-Reinforced Cementitious Composites (HPFRCC) in Structural Applications', RILEM Publications S.A.R.L., pp. 37–46.

Naaman, A. E. & Reinhardt, H. W. (1996), Characterization of high performance fiber reinforced cement composites, *in* A. Naaman & H. Reinhardt, eds, 'High Performance Fiber Reinforced Cement Composites 2 (HPFRCC 2)', The Second International RILEM Workshop, E and FN Spon, pp. 1–24.

Olsen, C. E. & Billington, S. L. (2007), Energy-absorbent infill panels for seismic retrofit of steel frame buildings using self-compacting, high-performance fiber-reinforced cementitious composites - phase 1: Single panel cyclic experiments, Technical Report 158, John E. Blume Center for Earthquake Engineering, Stanford University.

Østergaard, L. (2003), *Early-Age Fracture Mechanics and Cracking of Concrete*, DTU-Tryk.

Østergaard, L. & Olesen, J. F. (2006), Method for determination of tensile properties for ECC I: Formulation and parameter variation, *in* G. Fisher & V. C. Li, eds, 'International Rilem Workshop on High Performance Fiber-Reinforced Cementitious Composites (HPFRCC) in Structural Applications', RILEM Publications S.A.R.L., pp. 47–55.

Østergaard, L., Walter, R. & Olesen, J. F. (2006), Method for determination of tensile properties for ECC II: Inverse analysis and experimental results, *in* G. Fisher & V. C. Li, eds, 'International Rilem Workshop on High Performance Fiber-Reinforced Cementitious Composites (HPFRCC) in Structural Applications', RILEM Publications S.A.R.L., pp. 57–64.

Rashid, Y. R. (1968), 'Ultimate strength analysis of prestressed concrete pressure vessels', *Nuclear Engineering and Design* **7**, 334–344.

Shao, Y., Li, Z. & Shah, S. P. (1993), 'Matrix cracking and interface debonding in fiber-reinforced cement-matrix composites', *Advn. Cem. Bas. Mat.* **1**, 55–66.

Stang, H. (1992), Evaluation of properties of cementitious fiber composite materials - In high performance fiber reinforced cement composites, *in* H. Reinhardt & A. Naaman, eds, 'High Performance Fiber Reinforced Cement Composites', The International RILEM/ACI Workshop, E and FN Spon, pp. 388–406.

Stang, H. (2005), 'Mechanics of frc materials and structures', *Lecture notes: Materials Modelling given at the Departmentof Civil Engineering, DTU* .

Stang, H. & Li, V. C. (1999), *Extrusion of ECC-material*, Vol. 203-212, Chapman and Hull.

Stang, H., Olesen, J. F., Poulsen, P. N. & Dick-Nielsen, L. (2007), 'On the application of cohesive crack modeling in cementitious materials', *Materials and Structures* **40**, 365–374.

Tada, H. (1985), *The stress analysis of crack handbook*, 2 edn, Paris Production Incorporated, Missuori.

EQE International (1995), 'EQE symmary peport, the january 17, 1995 kobe earthquake'.

van Mier, J. G. M. (2004), Reality behind fictitious cracks?, *in* K. W. S. B. V.C. Li, C.K.Y. Leung, ed., 'Fracture Mechanics of Concrete Structures', Vol. I, Ia-FraMCos, pp. 11–30.

Walter, R., Olesen, J. F. & Stang, H. (2005), Interface mixed mode model, *in* H. A. R. E. Gdoutos, P. Rama Rao & S. Valente, eds, '11th International Conference on Fracture', Vol. Topic 29 - Full paper on CD, ICF, p. 917.

Walter, R., Olesen, J. F., Stang, H. & Vejrum, T. (2007), 'Analysis of an orthotropic deck stiffened with a cement-based overlay', *Journal of Bridge Engineering* **12**(3), 350–363.

Wang, S. & Li, V. C. (2004), 'Tailoring of pre-existing flaws in ECC matrix for saturated strain hardening', *Ia-FraMCos* .

Wang, S. & Li, V. C. (2006), Polyvinyl alcohol fiber reinforced engineered cementitious composites: Material design and performances, *in* G. Fisher & V. C. Li, eds, 'International Rilem Workshop pn High Performance Fiber Reinforced Cementitious Composites (HPFRCC) in Structural Applications', RILEM Publications S.A.R.L., pp. 65–73.

Wu, H. C. & Li, V. C. (1995), 'Stochastic process of multiple cracking in discontinuous random fiber reinforced brittle matrix composites', *Int'l of J. of Damage MEchanics* **4**(1), 83–102.

Zhang, J., Stang, H. & Li, V. (2001), 'Crack bridging model for fibre reinforced concrete under fatigue tension', *International Journal of Fatigue* **23**(8), 655–670.

Part II

Appended Papers

Paper I

Semi-analytical cohesive crack model for the analysis first crack strength of mortar

In Proceedings of: *the 17th Nordic Seminar on Computational Mechanics, Sweden, 2004*
A. Eriksson, J. Månsson and G. Tibert (eds)
Page 183-186

Semi-analytical cohesive crack model
for the analysis of first crack strength of mortar

Lars Dick-Nielsen, Peter Noe Poulsen, Henrik Stang and John Forbes Olesen
Department of of Civil Engineering
Technical University of Denmark, Lyngby, Denmark
e–mail: ldn@byg.dtu.dk, pnp@byg.dtu.dk, hs@byg.dtu.dk and jfo@byg.dtu.dk

Summary This paper discusses the tensile strength of bulk mortar and cement paste as a function of the initial defects and the toughness of the mortar and paste. A cohesive crack model, the fictitious crack model, is applied and it is shown that the process zone is of considerable length and that consequently LEFM cannot be used for prediction of tensile strength of the bulk material based on realistic defect sizes.

Introduction

Cement, mortar and concrete are usually characterized as brittle or quasi-brittle materials. The proper modelling of crack initiation and propagation in these materials has been under debate and intense research for more than 30 years. By now it is generally agreed upon that the cohesive crack model called the *fictitious crack model*, attributed to Hillerborg, [1], provides a reasonable consistent framework for the modelling of mode I propagation in concrete.

In implementations of the fictitious crack model it is not always insured that the stress intensity factor at the tip of the fictitious crack is in fact eliminated by the applied cohesive stresses, which in this case classifies the fictitious crack model as a bridged crack model rather than a cohesive crack model according to Cox and Marshall, [2].

Mortar is more brittle than concrete and neat cement paste again in general is more brittle than mortar. This effect is ascribed to the toughening effect of the aggregate at various scales linked to mechanisms like micro-crack shielding, crack deflection, crack trapping and aggregate/ligament bridging, see [3]. Each of these mechanisms lend itself to bridged crack modelling, while fine mortar and cement paste alone is often considered as materials which can adequately be described by linear elastic fracture mechanics, LEFM. Unfortunately the LEFM approach to neat cement paste or fine mortar presents discrepancies with respect to both the absolute size of initial defects as well as the dependency of tensile strength of the bulk material on variations in initial defect size.

In the present paper a cohesive version of the fictitious crack model is introduced in order to describe the influence of initial defects on the tensile strength of bulk. It is shown that even for such brittle materials the cohesive zone (or the process zone) is long enough to eliminate the use of LEFM. Also, it is found that the relation between initial defect size and tensile strength found in experiments by Wang and Li, [4] can be described with the fictitious crack approach. The approach taken is similar to the approach taken by Li and Liang in the investigation of fracture processes in concrete and fiber reinforced cementitious composites, [5].

Theoretical background

Material model

In this paper a crack in mortar is assumed to be cohesive and the cohesive law is simplified by a bilinear stress-separation curve as shown in Figure 1, where the area under the curve can be interpreted as the fracture energy G_F. The material is assumed to be linear elastic until the tensile strength f_t is reached. After crack initiation the material softens and follows the bilinear stress-separation relationship.

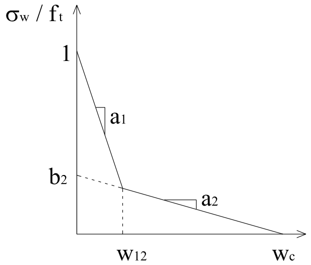

Figure 1: Bilinear stress-separation curve.

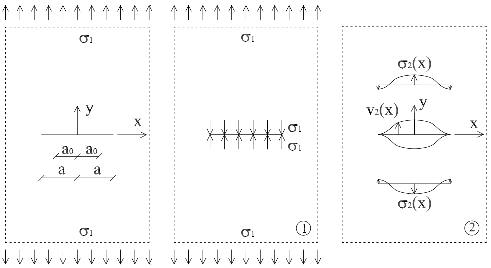

(a) Crack length. (b) Solution 1. (c) Solution 2.

Figure 2: Center cracked sheet.

Center cracked sheet

An infinite sheet with a center crack loaded in uniaxial tension is considered. The initial stress free crack is a slit of length $2a_0$ and the total length of the propagated crack is $2a$, see Figure 2(a). The cohesive crack is assumed to be stable when the stress intensity factor K_I is equal to zero. The equilibrium condition for a given crack length $2a$ and far-field stress σ_1 can be found by superposition of the two fundamental solutions illustrated in Figure 2(b) and 2(c).

The first fundamental solution is the trivial one. The stresses, σ_1 on the crack faces cause the stress state to be uniform in the sheet, the opening of the crack to be zero $v_1(x) \equiv 0$ and therefore K_{I1} is zero. The second fundamental solution is a crack in an infinite sheet loaded along the crack face by the stresses $\sigma_2(x)$. This solution is found by integration of an exact solution for a pair of opposite point loads, see Tada [6]. This leads to the following expressions for K_{I2} and $v_2(x)$.

$$\frac{1}{2}w(x) = v_2(x,0) = -\int_{-a}^{a} \frac{2\sigma_2(\xi)}{\pi E'} cosh^{-1} \frac{a^2 - \xi x}{a|x-\xi|} d\xi \tag{1}$$

$$K_I = 0 = K_{I2\pm a} = -\int_{-a}^{a} \frac{\sigma_2(x)}{\sqrt{\pi a}} \frac{\sqrt{a^2 - x^2}}{a \pm x} dx \tag{2}$$

where ξ is a variable along the x-axis, $w(x)$ is the total crack opening, $\sigma_2(x)$ is positive as outward normal to the crack face and $E' = E$ for plane stress. By use of the cohesive law (see Figure 1) and obtaining equilibrium by superposition of the two fundametal solutions the stress distribution along the crack face is:

$$\sigma_2(x) = \sigma_w\left(w(x)\right) - \sigma_1 \qquad \text{with } \sigma_w(x) = 0 \text{ for } |x| \leq a_0 \tag{3}$$

By satisfying both (1) and (3) the opening profile $v_2(x)$ can be found for a given far-field stress σ_1 and an imposed crack length a. Then K_I can be found from (2). Requiring K_I to be zero it is possible from (1), (2) and (3) to find matching values for the crack length a and the far-field stress σ_1 for a cohesive crack. The solution is found by numerical integration and by use of MATLAB's algorithms for solving non-linear equations. The displacement interpolation along the crack face is done by use of cubic splines. A numerical study, modelling only half the crack face due to symmetry, has shown that it is sufficient to use 11 discrete points.

First crack strength

Material data

The influence of the initial crack length a_0 as well as the shape of the stress-separation curve on the first crack strength σ_{fc} has been investigated.

The results of the present investigation are compared to the results by Wang and Li [4]. For a mortar with the same mixing as mix 3 in [4], material data has been obtained from an inverse analysis of a wedge splitting test (WST) [7] [8]. The following material data was found: the tensile strength $f_t = 2.83\,\mathrm{MPa}$, the stress-separations constants $a_1 = -1.556 \cdot 10^5\,m^{-1}$, $a_2 = -9.735 \cdot 10^3\,m^{-1}$ and $b_2 = 0.241$, the fracture energy $G_F = 14.05\,\mathrm{N/m}$ and the elastic modulus $E = 31\,\mathrm{GPa}$. The tensile strength f_t obtained from an inverse analysis of a WST will be less than the ideal strength of a defect free material. Therefore, in the following calculations the fracture energy G_F and the second part of the stress-separation curve a_2, b_2 are held constant, while f_t and thereby a_1 will be varied, keeping G_F constant.

The dependency of f_t and a_0

For values of f_t between 3-6 MPa, the relationship between the far-field stress σ_1 and the crack length a are calculated and the results for f_t equal to 3 and 5 MPa are plotted in Figure 3, for different sizes of the initial crack length a_0. In Figure 3 the present solutions as well as the solution according to LEFM are plotted ($\sigma_1\sqrt{\pi a} = K_{IC} = \sqrt{EG_F}$). Figure 3 shows that the peak stress drops when the initial crack length a_0 is increased, which was expected. In the following the peak stress will be identified with the first crack strength, σ_{fc}. Another tendency is that a high value of f_t results in a high sharp peak, while a low value of f_t results in low flat peak. This is caused by the fact that the fracture energy G_F is the same in all cases. All curves approach the LEFM curve asymptotically for large cracks. This is in good agreement with the theory of LEFM where the fracture process zone is regarded as a point.

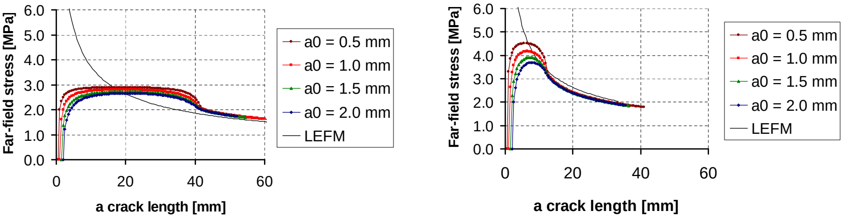

(a) Tensile strength f_t = 3 MPa.

(b) Tensile strength f_t = 5 MPa.

Figure 3: Far-field stress σ_1 and matching crack length a.

The materials with the different tensile strength f_t all show the same tendency regarding the development of the process zone. Figure 4 illustrates the development of the process zone for an initial crack length a_0 of 1 mm. For a tensile strength f_t of 5 MPa the transition opening on the stress-separation curve w_{12} is 2.59 μm, see Figure 1. For a tensile strength f_t of 5 MPa and an initial crack length a_0 of 1 mm the first crack strength will appear for a crack length a of 7 mm, see Figure 3(b). On Figure 4 it is seen that for this crack length the entire process zone will be related to the first branch of the stress-separation curve ($w < w_{12}$). For a crack length a of 12.5 mm the beginning of the process zone is seen to cross the the transition opening on the stress-separation curve w_{12}. Finally, for a crack length a of 25 mm the process zone is seen mostly to be related to the second branch of the stress-separation curve, and the process zone is still not fully evolved.

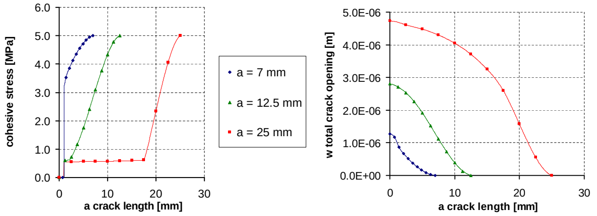

(a) cohesive stress. (b) Total crack opening.

Figure 4: Tensile strength f_t = 5 MPa and initial crack length a_0 = 1 mm

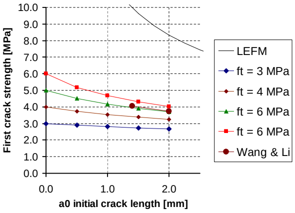

Figure 5: Relation between first crack strength σ_{fc} and initial crack length a_0.

In Figure 5 the first crack strength σ_{fc} is plotted as a function of the initial stress free crack length a_0. In the figure, furthermore, the results from Wang and Li [4] are plotted.

Figure 5 shows that even though mortar is often regarded as brittle, LEFM can not be used to calculate the first crack strength σ_{fc} when reasonable initial crack lengths are considered. The results from Wang and Li [4] show good agreement with the present results since the slope of the experimental curve almost coincides with the present model curves in Figure 5. Through a linear interpolation the tensile strength of the matrix is found to be 5.17 MPa.

According to the exact solutions in Tada [6] using the crack length at the peak load ($f_t = 5$MPa and $a_0 = 1$mm) it is found that by altering the shape of the initial stress free crack from a slit to a circular hole the K_I will change less than 1 %. This indicates that the shape of the original stress free crack is not that important for the first crack strength. Therefore, the present analysis is expected to give a reasonable result regardless of the initial shape of the stress free crack.

Concluding remarks

The present results show that even though mortar commonly is regarded as brittle, LEFM can not be used for calculation of the first crack strength. In the investigated interval of the initial crack length a_0, it is shown that the first crack strength σ_{fc} is lower than the apparent tensile strength f_t. According to LEFM the first crack strength and the apparent tensile strength will be identical in this interval.

References

[1] A. Hillerborg, M. Modéer and P.E. Petersson Analysis of Crack Formation and Crack Growth in Concrete by Means of Fracture Mechanics and Finite Elements *Cem. Concr. Res.*,**6**, 6, 773-782, 1976.

[2] B. Cox and D. Marshall Concepts in the Fracture and Fatigue of Bridged Cracks. *Acta Metallurgica et Meterialia*, **42**, 341-363, 1994.

[3] V.C. Li and M. Maalej Toughening in Cement Based Composites. Part I: Cement, Mortar and Concrete. *Cement and Concrete Composites*, **18**, 223-237, 1996.

[4] Shuxin Wang and Victor C. Li Tailoring of pre-existing flaws in ECC matrix for saturated strain hardening. *Ia-FraMCos*, (2004).

[5] Victor C. Li, M. ASCE and Erwin Liang Fracture Processes in Concrete and Fiber Rienforced Cementitious Composites. *Journal of Engineering Mechanics*, (1986).

[6] Hiroshi Tada *The stress analysis of crack handbook*. - Second edition. Paris Production Incorporated, Missuori, Second edition, (1985).

[7] Shuxin Wang *Private communications*. DTU, (2004).

[8] L. Østergaard, J. F. Olesen, H. Stang and D. A. Lange A simple and fast method for interpretation and inverse analysis of the wedge splitting test *Submitted for publication*

Paper II

Micro-mechanical Analysis of Fiber Reinforced Cementitious Composites using Cohesive Crack Modeling

In: *Journal of Advanced Concrete Technology*
2007, Volume 5, Number 3, page 373-382.

Micro-mechanical Analysis of Fiber Reinforced Cementitious Composites

Lars Dick-Nielsen[1], Henrik Stang[2] and Peter Noe Poulsen[3]

Received 11 April 2007, accepted 2 July 2007

Abstract

This paper discusses the mechanism appearing during fiber debonding in fiber reinforced cementitious composites with special emphasis on Engineered Cementitious Composites (ECC). The investigation is performed on the micro scale by use of a Finite Element Model. The model is 3 dimensional and the Fictitious Crack Model (FCM) and a mixed mode interface model are implemented. It is shown that the cohesive law for a unidirectional fiber reinforced cementitious composite can be found through superposition of the cohesive law for mortar and the fiber bridging curve. A comparison between the numerical and an analytical model for fiber pull-out is performed.

1 Introduction

Fiber bridging, i.e. fibers bridging a propagating and opening matrix crack, is a fundamental mechanism governing the nonlinear behavior of fiber reinforced cementitious composites. The stresses carried across the crack by the bridging fibers are often described with an (average) cohesive law. When a cohesive law is applied for the matrix crack as well, an average cohesive law emerges describing the crack in the composite.

Li et al. (1993) suggested using a superposition scheme for the fiber bridging cohesive stresses and the matrix cohesive law (the Fictitious Crack Model, FCM, Hillerborg et al., 1976) in order to derive an average cohesive law for fiber reinforced concrete. Engineered Cementitious Composite (ECC), (see e.g. Li, 2003) is a high performance, discontinuous fiber reinforced cementitious composite, which - in contrast to conventional fiber reinforced concrete - is characterized by its ability to undergo strain-hardening in tension. Strain-hardening is achieved through multiple cracking of the material. For strain-hardening to occur in an ECC material it is required, that the criteria for multiple cracking are satisfied. These criteria require that (1) the maximum fiber bridging stress is higher than the stress at which cracking is initiated and that (2) the cracks propagate in a steady state manner in an infinitely large specimen (see Li et al. 1992). Both criteria can be expressed in terms of the average cohesive law for the composite. Thus, in order to engineer ECC materials it is essential to be able to predict the average cohesive law for the composite. The cohesive law for the mortar can be found e.g. from a wedge splitting test and an inverse analysis (see e.g. Østergaard 2003). A closed form solution for the total response of the fibers has been derived (see e.g. Lin et al. 1999). The approach in the derivation is first to derive an analytical solution for the fiber debonding and pull-out case and then integrate this solution over the crack surface for random orientation and position of the fibers. Having arrived at the cohesive laws for the matrix and the fibers respectively, the remaining question now is: can the cohesive law for the ECC material be found through a simple superposition of the two fundamental laws or will there be effects that make superposition invalid? Or in other words, is the debonding and subsequent pull-out case representative of the fiber bridging, which takes place in the composite?

One effect that might be able to cause superposition to be invalid is described by Cook and Gordon (1964). In their paper they describe how a tensile stress field is formed in front of a crack tip and how this tensile stress field can cause debonding of a weak interface in front of the crack. If significant fiber-matrix debonding takes place before the crack tip reaches the fiber, the fiber debonding case with an initially perfect fiber-matrix interface would not be representative of the fiber bridging case and a direct superposition would not be valid during crack initiation. In the present paper this effect will be denoted the Cook/Gordon effect. Another effect possibly invalidating superposition could be matrix spalling (Leung and Li 1992, Leung and Chi 1995) taking place at the crack surface during inclined fiber debonding and pull-out. However, here matrix spalling is assumed to be a phenomenon primarily associated with fiber pull-out and thus not associated with the initial matrix crack propagation and fiber-matrix debonding. In the present investigation only initial matrix crack propagation and the associated fiber-matrix debonding is investigated thus matrix spalling is not included and only a fiber oriented perpendicular to the matrix crack surface is modeled.

Though the present approach has many similarities with other investigations of the fiber-matrix debonding and pull-out problem (e.g. Stang et al. 1990, Naaman et al. 1991, Leung and Li 1991 and others) and matrix crack formation in fiber composites (e.g. Aveston, Cooper and

---

[1] PhD-student, Department of Civil Engineering, Technical University of Denmark (DTU), Denmark.
[2] Professor, Department of Civil Engineering, Technical University of Denmark (DTU), Denmark. *E-mail:* hs@byg.dtu.dk
[3] Associate Professor, Department of Civil Engineering, Technical University of Denmark (DTU), Denmark.

Kelly 1971, Budiansky, Hutchinson and Evans 1986), emphasis is here placed on the *interaction* between fiber-matrix debonding and matrix crack formation. In the present approach matrix cracking is described using cohesive crack modeling originating from the FCM. Though the ECC matrix is often considered brittle, Dick-Nielsen et al. (2004) found the cohesive fracture mechanical approach to be more suitable than Linear Elastic Fracture Mechanics (LEFM) for modeling of crack propagation in paste and mortar. The cohesive crack model assumes the presence of a process zone and implicitly links this process zone to various micro-cracking and bridging mechanisms in the matrix.

The analysis presented is based on the concept of a Representative Volume Element (RVE). An RVE can traditionally be thought of either as an element containing a sufficiently number of microstructural inhomogeneities in order for it to be considered macroscopically homogeneous. Alternatively, it can be thought of as a (small) repetitive element from which a true RVE can be constructed. In both cases the element is subjected to boundary conditions which would introduce a homogeneous stress and strain state in the element, if the element was homogeneous, thus allowing for simple interpretation of the behavior of the inhomogeneous element in terms of average properties such as stiffness. Here the latter approach will be taken.

In the present paper the validity of the superposition scheme of the fundamental cohesive laws in order to obtain the average cohesive law for a typical ECC composite is investigated. To investigate whether superposition of the cohesive laws for the mortar and fiber bridging is valid, a Finite Element Method (FEM) model is set up. The three basic cases: debonding of a straight fiber perpendicular to the crack face, crack propagation in pure mortar and crack propagation in a RVE with mortar and fiber are analyzed and a parameter study is performed. Finally, a comparison between the numerical and an analytical model for fiber debonding and pull-out is performed.

2 Model description

2.1 Mesh

To investigate crack propagation in a RVE, a FEM model is used. Symmetry is assumed and the RVE is only representing one side of the crack (see **Fig. 1**). The aim of the investigation is to determine whether superposition of the cohesive laws for the fiber and the mortar can be applied in order to find the cohesive law for the RVE. Particularly, it will be investigated how the initial fiber-matrix debonding takes place in the fiber pull-out case and in the model involving matrix cracking, respectively. Therefore only the first part of the fiber-matrix debonding is relevant and the height of the RVE is chosen so the debonding of the fiber will not reach the end of the model for relevant matrix crack openings. To control where the crack propagation starts a straight notch is introduced in the crack plane.

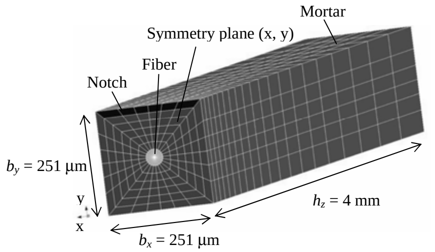

Fig. 1 The applied mesh and dimensions for the total model. Height, h_z = 4 mm and width, $b_x = b_y$ = 251 µm.

For modeling of the fiber, 15 node, wedge shaped, solid elements are used and for the mortar 20 node, cubic shaped, solid elements are used. The elements are based on quadratic interpolation and Gauss integration. Between the mortar and the fiber and in the symmetry crack plane 8+8 nodes interface elements are used. The model contains 3984 elements. The computation time was in the order of 14 hours on a computer with a 2.4 GHz Intel Xeon processor and 3 Gb RAM.

In the model the fiber is assumed to have a diameter of 40 µm and the length of the sides, *b* in the (x,y)-plane are 251 µm (symmetry plane). This gives a fiber volume percent of 2, which is typical for ECC. The height, h_z of the RVE is 4 mm. The length of the PVA fibers are typically 12 mm, but because the simulations end before the debonding of the fiber is completed, only 4 mm is modeled.

The model containing the fiber as well as the mortar crack (in the symmetry crack plane) is referred to as the total model. When the mortar crack is replaced with a free surface, the model can be used to simulate fiber debonding and pull-out. For convenience this model is referred to as the fiber pull-out model. Replacing the fiber by mortar and letting the mortar crack interface cover the entire bottom surface the model can simulate crack propagation in pure mortar.

2.2 Constraints

The displacements perpendicular to the end planes in the (x,y)-plane are constrained. This causes the load to be applied as a displacement load. The nodes in each side of the RVE in the (z, x)- and (z, y)-plane are tied together in the direction perpendicular to the plane. This causes the edges in the (x, z)- and (y, z)-planes to remain plane and result in a stress state throughout the RVE in average equal to plane stress.

2.3 Mixed mode cohesive crack model

The fiber-matrix interface crack as well as the mortar crack is modeled using a mixed mode cohesive model where the normal stresses, σ, and the shear stress, τ, depend on both the displacement in the tangential δ_t and the normal δ_n direction (see Walter et al. 2005).

$$\sigma = \sigma(\delta_t, \delta_n) \tag{1}$$

$$\tau = \tau(\delta_t, \delta_n) \tag{2}$$

In addition to the usual softening relations between normal deformation and normal stress and shear deformation and shear stress, softening of the cohesive normal stress law takes place due to a shear deformation and the same apply for the shear stress law and deformations in the normal direction. The model is incremental and has been implemented into the commercial finite element program DIANA.

2.4 Deriving the average cohesive law from the RVE

The aim is to derive an average cohesive law (σ_w, w) for the RVE. Here σ_w is the applied stress and w is the average crack opening. The average crack opening, w can be found by taking the total elongation, δ of the RVE and subtract the elastic elongation (see **Fig. 2**) where the total elongation is found from the FEM calculation.

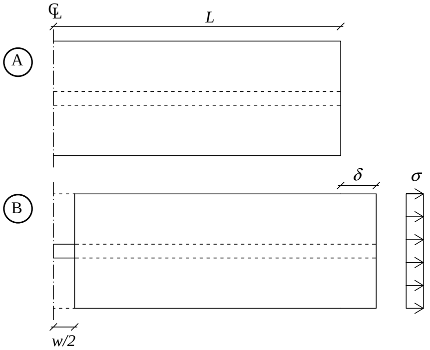

Fig. 2 Relationship between the average crack opening, *w/2* and the applied stress, σ.

The average crack opening, w can be found from the relation below, where the elastic strain, ε can be found from the applied stress, σ and the composite stiffness. Using these equations all effects from non-uniform crack opening and initial debonding will be included in the average crack opening.

$$\begin{aligned} \delta &= \varepsilon \cdot L + w/2 \\ \delta &= \sigma / \left(E_f \cdot \xi_f + \left(1 - \xi_f\right) \cdot E_m \right) \cdot L + w/2 \end{aligned} \tag{3}$$

$$w/2 = \delta - \sigma / \left(E_f \cdot \xi_f + \left(1 - \xi_f\right) \cdot E_m \right) \cdot L \tag{4}$$

Here E_f and E_m are the plane stress elastic moduli for the fiber and the mortar respectively, ξ_f is the fiber volume concentration and σ is the average stress applied by the prescribed displacement. This formulation enables the determination of an average crack opening without integrating over the actual crack opening profile.

Equation (4) is applied in the interpretation of the fiber pull-out model as well as the pure mortar model. This makes comparison between the obtained (σ_w, w)-relations from the different models consistent.

2.5 Material parameters

In the next section the results from the performed investigations are presented. First the results for one set of material parameters are presented and afterwards a parameter study is performed. Typical data from a PVA fiber ECC material are considered.

To perform the FEM calculation two sets of cohesive laws are needed for each calculation, one for the mortar crack and one for the interface between mortar and the fiber. The cohesive law for the mortar is based on experimental investigations on a typical ECC matrix (obtained by Shuxin Wang, University of Michigan) where a bi-linear cohesive law is determined from wedge splitting tests and inverse analysis. The cohesive law for the interface between the mortar and the fiber is difficult to measure. Therefore values determined by Shao, Li and Shah (1993) are taken as a basis for the mode II cohesive law, while the mode I cohesive law is estimated. To get a better understanding of the influence of these cohesive laws a parameter study is performed.

The mode I cohesive law for the mortar is assumed to be bi-linear as shown in **Fig. 3**. The following parameters were determined: the tensile strength f_t = 2.83 MPa, the stress-separation constants a_1 = -156 mm^{-1}, a_2 = -9.74 mm^{-1} and b_2 = 0.241, the fracture energy G_F = 14.1 N/m, the elastic modulus E = 31.0 GPa and the Poisson's ratio ν = 0.2. The cohesive law for the shear stresses (mode II) in the mortar is not significant, since the crack will mainly propagate in a mode I. This is confirmed by calculations performed during the present investigation. The cohesive mode II law for the mortar is chosen as a linear relation: τ_{max} = 3.0 MPa and the slope of the stress-separation curve a_1 = -50 mm^{-1}.

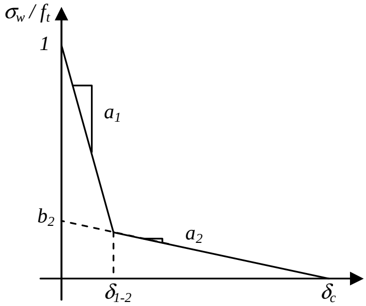

Fig. 3 Bi-linear stress-separation curve and the associated terminology.

The Young's modulus for the PVA fibers is E_f = 42.8 GPa and the Poisson's ratio is chosen to ν = 0.2. This Poisson's ratio is chosen in order to isolate the Cook/Gordon effect from any influence of a possible Poisson's effect. In the parameter study the effect of the Poisson's ratio will be investigated separately. The cohesive mode II law for the fiber-matrix interface is also bi-linear and has the following values: The shear strength τ_{max} = 3 MPa, constants a_1 = -222 mm^{-1}, a_2 = -19.6 mm^{-1} and b_2 = 0.392. These values are based on measurements of Shao et al. (1993), where a shear strength of 3 MPa was the largest measured. The mode I cohesive law for the fiber-matrix interface is estimated to vary linearly with a tensile strength of 0.5 MPa and a constant a_1 of -1000 mm^{-1}. Because of the difficulty in measuring the fiber-matrix cohesive law a parameter study will be performed.

3 Results

The approach now is to determine average cohesive laws in terms of stress-separation curves for the pure mortar model, the fiber pull-out model and total model. When these three curves are determined, the interrelationship between the curves is investigated and discussed.

3.1 Stress-separation curves

In **Fig. 4** average cohesive laws for the mortar model, the fiber pull-out model and total model are shown. In addition to these curves a curve made from superposition of the pure mortar curve and the fiber pull-out curve is shown. It appears from the figure that the average cohesive law from the total model can be found from a direct superposition of the pure mortar cohesive law and the fiber pull-out curve.

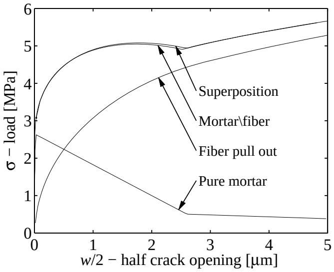

Fig. 4 Average cohesive laws.

In the next sections some of the mechanisms that appear during the crack propagation and fiber debonding will be discussed. This will give a better understanding of why superposition is valid for the present choice of material parameters.

3.2 Crack propagation in symmetry plane

In **Fig. 5** the crack front in the mortar interface is plotted for different loading stages. For an applied stress of 2.32 MPa only the elements close to the notch are open. The crack front is the point where the crack initiation takes place and the normal stress, σ is equal to the tensile strength, f_t.

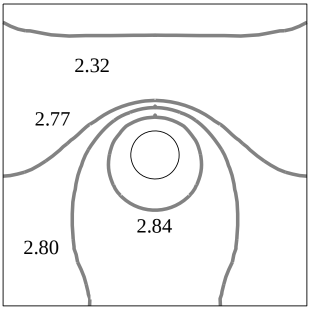

Fig. 5 Crack front for different loading stages (Load in MPa).

In the figure it is shown that the crack does not propagate directly across the fiber with a straight crack front. When the crack front gets close to the fiber the crack starts to propagate around the fiber leaving a section behind the fiber closed. As the load is increased, the section behind the fiber opens but in the opposite direction than the rest of the crack. The crack opening is less than 10 nm after the crack has propagated through the entire cross section of the RVE.

3.3 Debonding along the fiber

Fig. 5 illustrates how the crack propagates around the fiber in the mortar crack interface. Another interesting mechanism to illustrate is the mortar crack propagation versus the fiber debonding. In **Fig. 6 (a)** the lines at which the crack propagation in the mortar and the fiber debonding will be compared are marked with two fat lines. **Fig. 6 (b)** shows the crack propagation in the mortar compared with the debonding of the fiber for an applied stress of 2.80 MPa. In **Fig. 6 (b)** the deformations are scaled with a factor 10^4 and the opened nodes are marked with a circle.

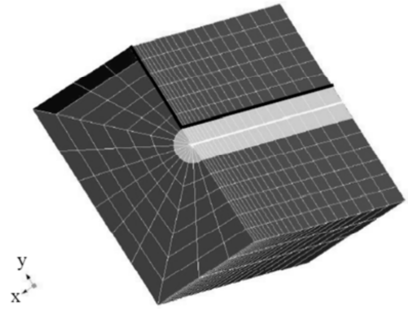

Fig. 6 (a) Cut in model.

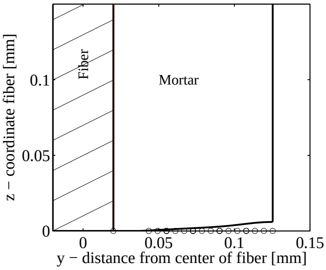

Fig. 6 (b) Debonding versus crack propagation.

The fiber starts to debond for an applied stress of 2.80 MPa, but debonding is only initiated at the node at the bottom. The debonding process continues when the crack in the mortar hits the fiber. At this point in time debonding has progressed 22 µm along the front of the fiber. It is seen that the Cook/Gordon effect is present but insignificant for the present choice of material parameters.

3.4 Stresses along the fiber-matrix interface in the total model

In sections 3.4 and 3.5 the stresses along the fiber-matrix interface at the front of the fiber (where the matrix crack first meets the fiber) will be discussed for the total model and the fiber pull-out model respectively. The fiber front is marked with a thick line in **Fig. 6**. **Fig. 7 (a)** shows the applied stress for the total model, **Fig. 7 (b)** the shear stresses on the fiber-matrix interface and **Fig. 7 (c)** the normal stresses on the fiber-matrix interface. In **Figs. 7 (b)** and **(c)** the curves refer to the values for the different load levels indicated in **Fig. 7 (a)**.

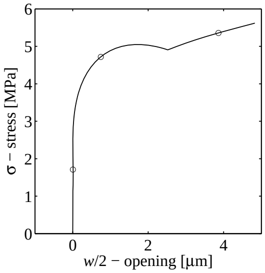

Fig. 7 (a) Applied load.

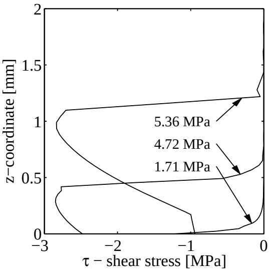

Fig. 7 (b) The shear stresses on the fiber-matrix interface. The curves refer to the values for the different load levels indicated in Fig. (a).

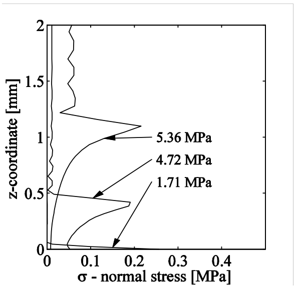

Fig. 7 (c) The normal stresses on the fiber-matrix interface. The curves refer to the values for the different load levels indicated in Fig. (a).

The maximum normal and shear stress in the cohesive laws for the mortar/fiber interface are 0.5 MPa and 3.0 MPa, respectively. In the **Fig. 7** it is seen that neither of the maximum stresses are reached due to the mixed mode material model applied to the interface. From the figures it is seen that debonding of the fiber in the total model is initiated by a combination of normal and shear stresses. But this mixed mode debonding process is not a phenomenon that is strictly related to the initiation phase of the debonding process. Early in the debonding process a characteristic shear and normal stress profile are formed and these profiles then move up along the fiber. Further it should be noted that the Poisson's ratio in the fiber and the mortar in this calculation are identical. A separate investigation of the effect of different Poisson's ratio in the fiber and matrix is performed later.

3.5 Stresses along the fiber-matrix interface in the fiber pull-out model

In the previous section the stresses along the fiber front was discussed for the total model. In this section a similar investigation is performed for the fiber pull-out model. **Fig. 8 (a)** shows the applied stress for the fiber pull-out model, **Fig. 8 (b)** the shear stresses on the fiber-matrix interface and **Fig. 8 (c)** the normal stresses on the fiber-matrix interface. In **Fig. 8 (b)** and **(c)** the curves refer to the values for the different load levels indicated in **Fig. 8 (a)**.

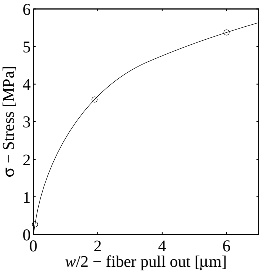

Fig. 8 (a) Applied load.

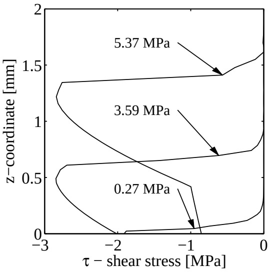

Fig. 8 (b) The shear stresses on the fiber-matrix interface. The curves refer to the values for the different load levels indicated in Fig. (a).

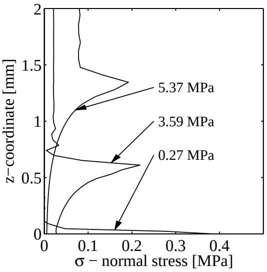

Fig. 8 (c) The normal stresses on the fiber-matrix interface. The curves refer to the values for the different load levels indicated in Fig. (a).

The results from the fiber pull-out model are very similar to the results obtained from the total model. Again the debonding is initiated due to a mixed mode stress combination. The tensile stress field in front of the debonding zone is not present in the analytical fiber pull-out model, which is the foundation for the derivation of the fiber bridging relation by Lin et al. (1999). The influence of leaving out the tensile stress field in the derivation of the analytical fiber pull-out model will be discussed in section 3.9. As stated in the previous section these tensile stresses are present even without a difference in the Poisson's ratio in the fiber and the matrix.

The similarity of the stress profiles for the total model and the fiber pull-out model, together with the weak effect of the Cook/Gordon mechanism and the fact that the mortar crack propagates through the RVE without initiating significant debonding, explains why superposition between the stress-separation curves for the mortar and fiber is valid.

3.6 Comparison of the Cook/Gordon approach and the cohesive approach

In order to investigate the effect of the applied fracture mechanical approach on the significance of the Cook/Gordon effect, the stress field ahead of the crack model applied by Cook and Gordon (1964) is compared with the stress field ahead of the cohesive crack applied in the present approach.

Cook and Gordon analyzed the stress state around a crack shaped as a flat ellipsoidal hole in an infinite sheet loaded in uni-axial tension. The ellipse has the semi-axes a and b resulting in a crack tip radius r ($r = b^2/a$). They assumed that the crack tip radius is of molecular dimensions and that it remains constant during crack propagation in a brittle medium. In **Fig. 9** the stress state in front of the crack tip is plotted according to Cook and Gordon (1964) for the ratio $a/b = 100$. In the figure σ_{xx} are the stresses parallel with the crack plane and σ_{yy} are perpendicular to the crack plane. Stresses have been normalized with respect to the maximum normal stress, σ_{yy}, which is identified as the tensile strength of the material.

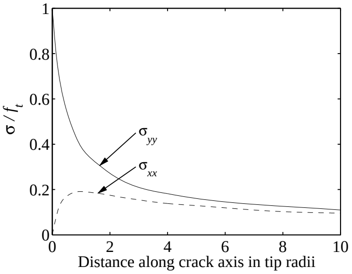

Fig. 9 Stress state in front of crack tip according to Cook and Gordon (1964).

The magnitude of the crack tip radius is assumed by Cook and Gordon to be 0.2 nm. This means that the peak in the normal stresses parallel to the crack plane σ_{xx} will appear very close to the crack tip. The ratio between the two peak stresses is found to be just below 1/5. To relate these results to the cohesive approach a sheet with the width 0.6 m and the height 0.5 m is modeled using FEM. The sheet is loaded in uni-axial tension and contains a slit like stress free crack with the length 4 mm (2 a_0). The dimensions are chosen such that the sheet can be regarded as infinite compared to the initial crack. The model contains an interface in which the crack can propagate. The model consist of 20 x 412 (height x width) quadrilateral, 8 nodes plane stress elements. The element size increase with a factor 1.025 from the crack tip towards the edge along the width, and with a factor 3 from the crack towards the ends along the height. The material used is identical to the mortar described in section 2.5 (f_t = 2.83 MPa). In **Fig. 10 (a)** matching values of the far field stress and the half crack length, *a* are plotted.

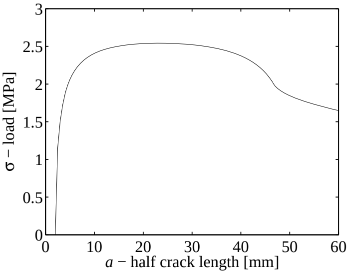

Fig. 10 (a) Matching values of far-field stress and crack length.

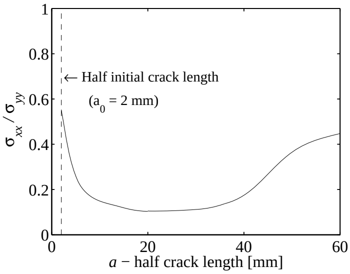

Fig. 10 (b) Ratio between the normal stresses at the crack tip.

In **Fig. 10 (b)** the ratio between the two normal stresses at the crack tip in the cohesive approach is plotted for different crack lengths, *a*. The ratio found in the cohesive approach is of the same magnitude as in the approach adopted by Cook and Gordon. For crack lengths in the micro scale the ratio between the normal stresses found in the cohesive model are significant higher than predicted by Cook and Gordon. The Cook/Gordon effect is therefore more pronounced in the cohesive approach.

3.7 Parameter study of the cohesive laws

In sections 3.1-3.5, the cracking and debonding process for one set of material parameters have been investigated. In order to evaluate the sensitivity of the conclusions on the choice of material parameters, a parameter study is carried out. The parameters being varied are the parameters characterizing the mixed mode cohesive law for the mortar/fiber interface as shown in **Fig. 11**.

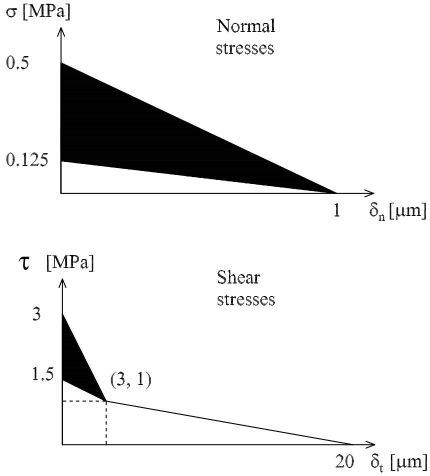

Fig. 11 Cohesive laws for the mortar/fiber interface with indication of the parameter variation in the parameter study undertaken.

For the normal stresses the tensile strength undergoes the values 0.125 MPa, 0.25 MPa and 0.5 MPa. For the shear stresses the slope of the first branch is varied. This is done by letting the shear strength undergo the values 1.5 MPa, 2 MPa and 3 MPa. Calculations for all combinations of normal and shear strength have been performed. The results obtained in this study are very similar to the ones obtained in the previous sections. The new results will therefore not be illustrated here.

An interesting combination was a low tensile strength (0.125 MPa) and a high shear strength (3 MPa). This could cause debonding in the total model to be initiated due to the Cook/Gordon effect while debonding in the fiber pull-out model would be initiated mainly due to shear stresses. The analysis showed that the low tensile strength did in fact lower the shear stress needed to initiate debonding in the total model. But because the same was valid in the fiber pull-out model, superposition between the cohesive laws for the mortar and fiber pull-out was still valid.

3.8 Parameter study of the Poisson's ratio

In the previous sections the fiber and mortar had the same Poisson's ratio. This was chosen in order to isolate the Cook/Gordon effect on the fiber debonding in the total model. In this section the fiber is given a more realistic Poisson's ratio of 0.35 in order to investigate the effect of the Poisson's ratio. For the present investigation four calculations are performed. The normal strength in the mode I cohesive law is varied from 0.125 MPa to 0.5 MPa. Finally, a pure mode II calculation is performed. In all calculations the cohesive mode II law with a shear strength of 3 MPa is used (see section 3.7). **Fig. 12** illustrates the stresses on the fiber-matrix interface at the fiber front (see **Fig. 6**) for the mode I law with a tensile strength of 0.5 MPa. In **Fig. 12 (b)** and **(c)** the curves refer to the values for the different load levels indicated in **Fig. 12 (a)**. The results from the calculation where the fiber has a Poisson's ratio of 0.35 are shown with thick lines and the corresponding results for at Poisson's ratio of 0.2 are shown with thin dotted lines.

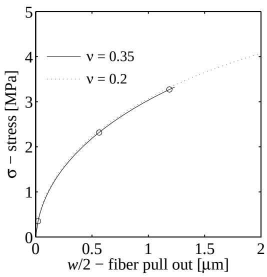

Fig. 12 (a) Applied load.

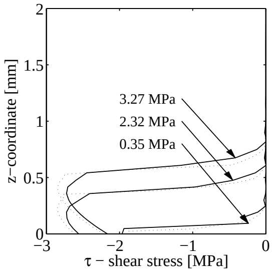

Fig. 12 (b) Shear stresses on the fiber-matrix interface. The curves refer to the values for the different load levels indicated in Fig. (a).

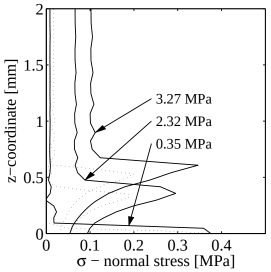

Fig. 12 (c) Normal stresses on the fiber-matrix interface. The curves refer to the values for the different load levels indicated in Fig. (a).

In the figures it is seen that increasing the Poisson's ratio in the fiber causes the normal stresses on the front of the fiber to increase as expected. Due to the mixed mode material model the increase in normal stresses causes the shear stresses to decrease. The shear stress profile for a Poisson's ratio of 0.2 has a higher peak stress but is a little slimmer compared to the corresponding results for a Poisson's ratio of 0.35. In total the fiber pull-out curves for the two Poisson's ratios end up being very similar, with the curve for a Poisson's ratio of 0.2 slightly higher than the curve corresponding to a Poisson's ratio of 0.35.

In **Fig. 13** fiber pull-out curves are plotted to illustrate the effect of the Poisson's ratio for different mode I cohesive laws on the interface.

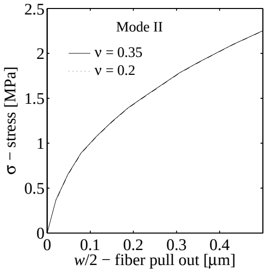

Fig. 13 Fiber pull-out curves as functions of fiber Poisson's ratio for different mode I cohesive laws on the interface: (a) Pure mode II.

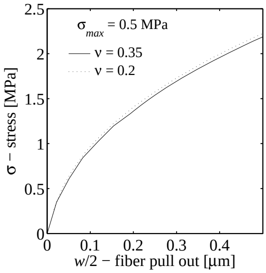

Fig. 13 Fiber pull-out curves as functions of fiber Poisson's ratio for different mode I cohesive laws on the interface: (b) tensile strength of 0.5 MPa.

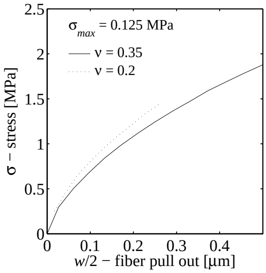

Fig. 13 Fiber pull-out curves as functions of fiber Poisson's ratio for different mode I cohesive laws on the interface: (c) tensile strength of 0.125 MPa.

In the extreme case where the mode I law is so strong that debonding will occur in pure mode II, the Poisson's effect can be neglected. When comparing **Fig. 13 (a)** and **(b)** it is observed that a mode I law with a tensile strength of 0.5 MPa results in a fiber pull-out curve close to the one obtained in the pure mode II calculation. This explains why the Poisson's ratio has so little influence when applying a mode I law with a tensile strength of 0.5 MPa. For a mode I cohesive law with a tensile strength of 0.125 MPa the difference in Poisson's ratio between the mortar and the fiber is seen to have a significant influence of results. This is because the increase in normal stresses becomes significant compared with the tensile strength. The conclusion is that if the interface between the fiber and the mortar has a week mode I cohesive law, it is important to include the effects introduced by the Poisson's ratio. In this investigation all fibers have been pulled out normal to the crack plane. Another relevant investigation is the Poisson's effect on pull-out of fibers inclined to the crack plane. When pulling out a fiber inclined to the crack plane, the Poisson's effect might be insignificant compared to the large contact pressure between fiber and crack face or possible spalling of the matrix.

3.9 Comparison of the analytical and numerical model for fiber pull-out

In this section a comparison is made between the present numerical model for fiber pull-out and the corresponding analytical model by Lin et al. (1999). Three assumptions are made in order to derive the analytical model: (1) an aspect ratio larger than 100. (This is fulfilled for most fibers and this is also valid for the present numerical model). (2) The slip between matrix and fiber during debonding is negligible hence the shear stresses are constant, τ_0. (This is not valid in the numerical model when applying a cohesive law. As illustrated in **Fig. 8** a shear stress profile is formed after debonding is initiated and as the debonding propagates the shear stress profile travels with the debonding). The Poisson's effect is negligible. As shown in the previous section the Poisson's effect can be neglected, but only in the case where the mode I cohesive strength between fiber and mortar is strong. Apart from these three assumptions the analytical model does not take into consideration the tension stress field in front of the debonded zone, hence debonding in the analytical model is pure mode II. The relation between the pull-out force, P, and the relative displacement, δ, between the fiber and the matrix in the analytical model is given by the expression below:

$$P=\sqrt{\frac{\pi^2\tau_0 E_f d_f^3(1+\eta)}{2}\delta+\frac{\pi^2 G_d E_f d_f^3}{2}} \qquad (5)$$

Here E_f and d_f are Young's modulus and diameter of the fiber respectably, and $\eta = V_m E_m / V_f E_f$ where V_m and V_f is the volume fraction of mortar and fiber respectively. The chemical bond strength, G_d is related to the fracture energy, G_f of the mode II cohesive law, however in the analytical model, G_d is assumed to be dissipated in a point. Because of the difficulties in deciding which constant frictional bond strength, τ_0 correspond to the applied cohesive law, a direct comparison between the numerical model and the analytical model is not performed. Instead an investigation is performed with the numerical model on the effect of the mode I cohesive law, which is left out in the analytical model. This is done by comparing fiber pull-out curves obtained from applying a fixed mode II law with a shear strength of 3 MPa together with a variation of the cohesive mode I laws. The cohesive laws used are the ones shown in section 3.7. In **Fig. 14** the fiber pull-out curves are plotted for a Poisson's ratio in the fiber of 0.35.

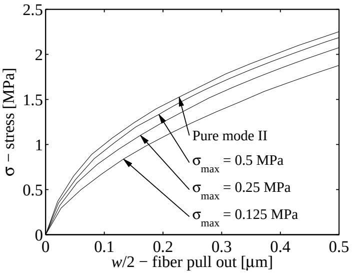

Fig. 14 Fiber pull-out curves for different mode I cohesive laws and a fixed mode II law using the numerical model with a Poisson's ratio in the fiber of 0.35.

In the figure it is seen that the pull-out load decreases for a decreasing tensile strength in the mode I cohesive law. If the analytical model is calibrated with a fiber pull-out test, the influence of leaving out the mode I part is probably not so significant, because the constants will be affected by the mixed mode conditions. If on the other hand the fiber pull-out is modeled based on independently obtained mode II constants then a significant error can be made by leaving out the mode I part, particularly if the mode I properties are relatively weak.

4 Concluding remarks

In the present investigation it has been examined whether superposition of the average cohesive law for the fiber pull-out and the cohesive law for mortar was valid in order to find the average cohesive law for the total model. Special attention was given to the tensile stress field in front of the crack tip, possibly leading to the so-called Cook/Gordon effect, while the investigations were limited to the case of straight fibers arranged perpendicular to the crack surface. The present investigation showed that in general superposition is valid. Furthermore it was found that a low mode I strength in the mortar/fiber interface did lower the shear stress needed to initiate debonding in the total model. However, because the same applied in the fiber pull-out model superposition of the cohesive laws was still valid.

The present investigation further showed that the mortar crack propagation and the subsequent fiber debonding and pull-out essentially are two separate mechanisms in the sense that the mortar crack propagated through the RVE without initiating any significant debonding: the mortar crack grows past the fiber and then gradually back towards the fiber before significant debonding begins.

The influence of a difference in the Poisson's ratio between mortar and fiber was examined. It was found that the Poisson's ratio did not have any influence on the problem and the debonding would propagate in an almost pure mode II, when the strength of the mode I interface between fiber and mortar was sufficient high. If on the other hand the mode I strength was low, then the increase in normal stresses due to the Poisson's effect did lower significantly the force needed to pull-out the fiber due to the mixed mode condition.

Finally, a comparison between an analytical and numerical model for fiber pull-out was conducted. In the analytical model the mixed mode stress condition is not taken into consideration. The conclusion is that as long as the analytical model is calibrated with fiber pull-out tests then the influence of leaving out the mode I part is not significant, because the material constants will be affected by the mixed mode conditions. If the mode I strength is low and the analytical model is not calibrated with tests then leaving out the mode I part can lead to overestimation of the load carrying capacity.

References

Aveston, J., Cooper, G.A. & Kelly, A. (1971) "Single and Multiple Fracture. The Properties of Fibre Composites." In: *Proc. Conf. National Physical Laboratories. 4. November. 1971. Guildford*. IPC Science and Technology Press Ltd. 15-24.

Budiansky, B., Hutchinson, J.W. & Evans, A.G. (1986) "Matrix Fracture in Fiber-Reinforced Ceramics." Journal Mech. Phys. Solids, 34, 167-189.

Cook, J., Gordon J. E., Evans, C. C. & Marsh, D. M. (1964). "A mechanism for the control of crack propagation in all-brittle Systems." *Proc. Roy. Soc*, 2282 A, 508-520.

Dick-Nielsen, L., Poulsen, P.N., Stang, H. & Olesen, J.F. (2004) "Semi-analytical cohesive crack model for the analysis of first crack strength of mortar." Proc. of the 17th Nordic Seminar on Computational Mechanics. (Eds A. Eriksson, J. Månsson and G. Tibert). 183-186.

Hillerborg, A., Modeer, M. & Petersson, P.E. (1976). "Analysis of Crack Formation and Crack Growth in Concrete by Means of Fracture Mechanics and Finite Elements." *Cem. Concr. Res*. 6, 773-782.

Leung, C.K.Y. & Li, V.C. (1991). "New Strength-based Model for the Debonding of Discontinuous Fibers in an Elastic Matrix." *Journal of Materials Science,* 26, 5996-6010.

Leung, C.K.Y. & Li, V.C. (1992). "Effect of Fiber Inclination on Crack Bridging Stress in Brittle Fiber Reinforced Brittle Matrix Composites." *Journal Mech. Phys. Solids,* 40, 1333-1362.

Leung, C.K.Y. & Chi, J. (1995). “Crack-Bridging Force in Random Ductile Fiber Brittle Matrix Composites.” *Journal of Engineering Mechanics, ASCE*, 121, 1315-1324.

Li, V. C., Stang, H. & Krenchel, H. (1993). “Micromechanics of Crack Bridging in Fiber Reinforced Concrete.” *Materials and Structures*, 26, 486-494.

Li, V.C. & Leung, C.K.Y. (1992). “Steady State and Multiple Cracking of Short Random Fiber Composites.” *ASCE J. Eng. Mech.*, 188, 2246-2264.

Li, V.C. (2003) “On Engineered Cementitious Composites (ECC) – A Review of the Material and its Applications.” *J. Advanced Concrete Technology*, 1, 215-230.

Lin, Z., Kanda, T. & Li, V. C. (1999) “On interface property characterization and performance of fiber-reinforced cementitious composites.” *J. Concrete Sci. & Eng.*, 1, 173-184.

Naaman, A.E., Namur, G.G., Alwan, J.M. & Najm, H.S. (1991) “Fiber Pullout and Bond Slip. I: Analytical Study.” *Journal of Structural Engineering.* 117, 2769-2790.

Shao, Y., Li, Z. & Shah, S. P. (1993). “Matrix cracking and interface debonding in fiber-reinforced cement-matrix composites.” *Advn. Cem. Bas. Mat*. 1, 55-66.

Stang, H., Li, Z. & Shah, S.P. (1990). “Pullout Problem: Stress versus Fracture Mechanical Approach.” *Journal of Engineering Mechanics*. 116, 2136-2150.

Walter, R., Olesen, J. F. & Stang, H. (2005). “Interface mixed mode model.” *Proceedings of 11th Internal Conference on Fracture*, Turin (Italy) – March 20-25, 2005. Mixed mode 4628.

Østergaard, L. (2003). “*Early-Age Fracture Mechanic. and Cracking of Concrete – Experiments and modelling*.” Ph.D. thesis, Department of Civil Engineering, Technical University of Denmark.

Paper III

Conditions for Strain-Hardening in ECC Uniaxial Test Specimens

Submitted to: *Journal of Engineering Mechanics*

CONDITIONS FOR STRAIN-HARDENING IN ECC UNIAXIAL TEST SPECIMENS

Lars Dick-Nielsen[1]

Henrik Stang[2]

Peter Noe Poulsen[3]

Abstract: The paper addresses the conditions for strain-hardening in uniaxial test specimens made from Engineered Cementitious Composites (ECC) by investigating crack propagation in ECC material. Unlike previous investigations, a cohesive approach is taken for the mortar crack. The ECC crack is also assumed to be cohesive and the cohesive law applied takes into account both fiber and mortar properties. The investigation was carried out using a semi-analytical model as well as a Finite Element Model allowing the effect of specimen shape and boundary conditions to be taken into account. The simulations were for one crack propagating in finite and infinite sheets under uniaxial tension. The results show that the maximum crack opening during crack propagation in various test specimen geometries was small, 20 μm, which is also small compared to typical deformations at peak bridging stress.

CE Database subject headings: Fracture Mechanics, Cracking, Concrete, Cements, Cohesion, Fiber reinforced materials, Strain hardening, Synthetic fibers.

---

[1] Ph.D.-student, Department of Civil Engineering, Technical University of Denmark, building 118, 2800 Kgs. Lyngby, Denmark. E-mail: ldn@byg.dtu.dk

[2] Professor, Department of Civil Engineering, Technical University of Denmark, building 118, 2800 Kgs. Lyngby, Denmark. E-mail: hs@byg.dtu.dk

[3] Associate professor, Department of Civil Engineering, Technical University of Denmark, building 118, 2800 Kgs. Lyngby, Denmark. E-mail: hs@byg.dtu.dk

1. Introduction

Fiber-reinforced cementitious materials are often classified based on their mechanical behavior when subjected to uniaxial tension. In such classification, a distinction is typically made between materials undergoing *tension-softening* and *strain-hardening* when subjected to uniaxial tension (Stang, 1992) and (Naaman and Reinhardt, 1996). It should be noted that the classification is based on the predominant behavior, because even materials undergoing tension-softening will always to a small extent, initially, undergo strain-hardening (see e.g. van Mier 2004) and materials undergoing strain-hardening will eventually undergo tension-softening when the final failure occurs (Naaman and Reinhardt, 1996). Tension-softening is typically associated with the formation of one or a few localized cracks, while strain-hardening is associated with the formation of multiple cracks. The two types of material behavior have significant consequences in terms of structural behavior, see e.g. (Li, 2003) and (Walter et al, 2007), where superior structural behavior from strain-hardening materials has been demonstrated. From a computational point of view, the two types of behavior also have wide-ranging consequences due to the fact that the strain localization associated with tension-softening requires a fracture mechanical approach, while strain-hardening materials can be described using continuum mechanics.

Not surprisingly, a lot of effort has been put into developing strain-hardening materials and a large number of different cementitious strain-hardening materials have been developed over the years. A targeted micromechanics-based engineering approach was taken by Li and co-workers in developing a strain hardening material with extreme strain-hardening capacity and crack width control see e.g. (Li, 1992). One of the objectives of the engineering approach was to develop a theoretical framework for the conditions in which strain-hardening occurs under uniaxial tension. Li and Leung (1992) showed that for strain-hardening to occur in an ECC specimen it is required that (1) the maximum stress carried by the fibers across an open mortar crack, the so-called fiber-bridging stress, is higher than the stress at which cracking is initiated, and that (2) the cracks propagate in a so-called steady-state manner in an infinitely large specimen (known as flat-crack propagation). These criteria were intended as guidelines identifying the important parametric dependencies and have served as such in material development and optimization, see e.g. (Li, 1998), (Li et al., 2002) and (Wang and Li, 2006). However, the criteria are simplified and do not take into account the finite size of a test specimen, the geometry and boundary conditions of the specimen, and the interaction between cracks and initial defects (localization). Furthermore, it should be noted that the criterion related to steady-state crack propagation is based on a linear elastic fracture mechanical description of the mortar.

The present paper investigates the stability of crack propagation under the influence of finite specimen size and boundary conditions. Dick-Nielsen et al. (2004) found the cohesive fracture mechanical approach to be more suitable than Linear Elastic Fracture Mechanics (LEFM) for modeling crack propagation in paste and mortar. In our modeling, the crack propagation was therefore assumed to be governed by cohesive fracture mechanics and a cohesive law was applied to the mortar, fibers and the ECC-material. The cohesive law for the ECC-material was found through superposition of the cohesive law for the mortar and the fiber-bridging curve; Dick-Nielsen et al. (2005) demonstrated the validity of this approach. To investigate crack propagation in an infinite sheet (in order to shed light on the criterion for steady-state flat-crack propagation originally derived by Marshall and Cox (1988)), a semi-analytical approach and Finite Element Method (FEM) simulations were employed. A series of numerical simulations of uniaxial tensile tests were carried out on specimens containing one predefined flaw. The simulations were performed to get a better understanding of the influence of finite specimen size and specific boundary conditions. A parameter study was performed to investigate the influence of mortar and fiber properties, specimen size, boundary conditions, and the position and size of the initial flaw.

Only the propagation of a single crack is considered here; the analysis relies on the implicit assumption that when the first-crack strength (peak far-field stress) is less than the maximum stress on the fiber-bridging curve (the peak fiber-bridging stress), and when the first crack propagates with crack openings less than the deformation associated with the peak on the fiber-bridging curve, then the fiber-bridging stress will eventually produce more cracks adjacent to the first and thus create multiple cracking and strain-hardening.

2. Fracture mechanics basis

Intuitively, it is clear that for strain-hardening to occur in an ECC specimen, the maximum crack opening has to be small during crack propagation compared to the crack opening at peak fiber-bridging stress, assuming that the fiber response during debonding and pullout is on average a smooth curve with an ascending part, a peak, and a subsequent descending part. In contrast, if the maximum crack opening is not controlled during crack propagation and exceeds the deformation at peak fiber-bridging stress, this would lead to a zipper type of crack propagation leaving the fibers on the descending part of the fiber-bridging response and thus creating a softening response from the composite material crack. According to Griffith (1920), the crack opening in a linear elastic material can be found from equation (1) and matching values of the crack length, $2a$ and the applied far-field stress, σ can be found from equation (2), (where K_{IC} is the critical mode I stress intensity factor).

$$v(x) = \frac{2\sigma}{E}\sqrt{a^2 - x^2} \tag{1}$$

$$\sigma = \frac{K_{IC}}{\sqrt{\pi a}} \tag{2}$$

The Griffith crack mode results in a crack opening shaped like an ellipse in which the opening at crack middle increases as the crack propagates**.** To avoid the opening increasing during crack propagation, the steady-state cracking criterion requires the crack to propagate in a flat-crack mode. Flat-crack propagation was first analyzed by Marshall and Cox (1988) applying the J-integral approach. According to Marshall and Cox the complementary energy, J'_b, of the fiber-bridging curve has to be larger than the mortar toughness, J_{tip}, as stated in equation (3).

$$J_{tip} \le w_0\sigma_0 - \int_0^{w_0} \sigma(w)dw = J_b^{'} \tag{3}$$

Here w is the crack opening, and $\sigma(w)$ is the average stress carried by the fibers, the so-called fiber-bridging curve with the peak point (w_0, $\sigma_0=\sigma(w_0)$). Both this criterion and the Griffith theory are based on LEFM. Dick-Nielsen et al. (2004) showed that although mortar is commonly regarded as brittle, LEFM cannot be used to accurately model crack propagation in such materials. A more adequate modeling can be achieved by the use of cohesive fracture mechanics in terms of the *fictitious crack model* (FCM) attributed to Hillerborg (1976). The FCM provides a good framework for the modeling of mode I propagation in most cementitious materials. In contrast to the cohesive models of Barenblatt (1962) and Dugdale (1960), the cohesive stresses in the crack in the FCM are not constant and not distributed over a predefined, short length, but depend on the crack-opening profile. Determining the cohesive laws for the materials in question is a fundamental issue when dealing with the FCM in connection with fiber-reinforced materials. For the average fiber response, the cohesive law is found by using a closed form solution derived by Lin et al. (1999). The cohesive law for ECC is then found through the superposition of the cohesive laws for the mortar and fibers; this approach has been suggested before by Li et al. (1993) and further concretized in numerical simulations by Dick-Nielsen et al. (2005).

3. Geometry and material parameters

At the present time, there is no global standard specimen geometry or test set-up for testing strain-hardening capabilities in ECC. However, a tendency in most approaches seen in the literature is that one dimension of the test specimen is significantly smaller than the other two. In order to arrive at some general conclusions, the majority of the simulations in the present paper were performed for an infinite sheet. Simulations for selected finite geometries were performed to relate these general conclusions to finite geometry. The simulations were all carried out for sheets loaded in uniaxial tension containing one initial stress-free slit-like flaw.

The cohesive law for the mortar was simplified by a bilinear cohesive law (see Figure 1 A)), in which the area under the curve can be interpreted as mortar toughness, J_{tip} (or mortar fracture energy G_f). The following parameters were used to describe the bilinear cohesive law: the tensile strength, f_t, the negative slope of the first linear part normalized with the tensile strength, a_1, the cut-off on the x-axis (stress normalized with the tensile strength) of the second linear part, b_2, and the negative slope of the second linear part normalized with the tensile strength, a_2. The material data for the mortar was obtained from Wang (2004) from an inverse analysis of a wedge-splitting test as described by Østergaard (2003). The following material data were found for the mortar: f_t = 2.83 MPa, a_1 = 156 mm^{-1}, a_2 = 9.7 mm^{-1} and b_2 = 0.24, the mortar toughness J_{tip} = 14.05 N/m and the elastic modulus E = 31 GPa.

To calculate the fiber-bridging curve, a closed-form solution derived by Lin et al. (1999) was used. For the fibers, the following material constants were used, which correspond to standard values given in (Lin et al., 1999) and (Li et al., 2002) for a typical, randomly oriented PVA fiber ECC material: the slip-hardening coefficient for the fiber/mortar interface, β = 2.21, the fiber volume fraction, v_f = 0.02, the snubbing coefficient, f = 0.3, the fiber strength reduction coefficient, f' = 0.3, the fiber length, L_f = 12 mm, the frictional stress on the fiber/mortar interface, τ_0 = 0.3 MPa, the modulus of the fiber, E_f = 42.8 GPa, the Young modulus of the mortar, E_m = 31 GPa, the chemical bond strength of the fiber/mortar interface, G_d = 4.71 N/m, the fiber diameter d_f = 39.6 μm, and the in-situ fiber strength σ_{fu} = 1400MPa.

The resulting cohesive law for the particular ECC material was found from the superposition of the pure mortar law and the fiber-bridging curve (Li et al. 1993, Dick-Nielsen et al. 2005). The ECC was assumed to be linear elastic until the tensile strength, f_t, for the ECC is reached. After crack initiation, the material follows the resulting cohesive law. During the present investigation, a parameter study of both the mortar data and the fiber data was performed. The cohesive laws for the mortar, fibers and ECC are shown in Figure 3 A).

4. Method of analysis

To investigate cohesive crack propagation in a sheet containing an initial flaw, a semi-analytical model and FEM calculations were used; the semi-analytical model was first employed by Dick-Nielsen et al. (2004). The model describes crack propagation in an infinite sheet loaded in uniaxial tension and containing a center crack. The length of the initial stress-free flaw is $2a_0$, and the total length of the propagated crack is $2a$; see Figure 1 B). The cohesive crack is assumed to close smoothly so that the stress intensity factor K_I is equal to zero. The equilibrium condition for a given crack length, $2a$, and far-field stress, σ_1, can be found by the superposition of the two fundamental solutions for a crack in an infinite sheet illustrated in Figure 1 C) and D).

In the first fundamental solution, the stresses, σ_1, are added to the crack faces, causing the crack to close ($v_1(x) \equiv 0$, where v_1 is the displacement of the crack surface due to the first fundamental solution) and the stress state to be uniform in the sheet, so that the stress intensity factor due to the first fundamental solution, $K_{I,1}$, is zero. In the second fundamental solution the crack is loaded along the crack face by the stresses, $\sigma_2(x)$. This solution is found by integration of an exact solution for a pair of opposite point loads, see Tada (1985). The following expressions for the stress intensity factor and the displacement of the crack surface, $K_{I,2}$ and $v_2(x)$, can then be found:

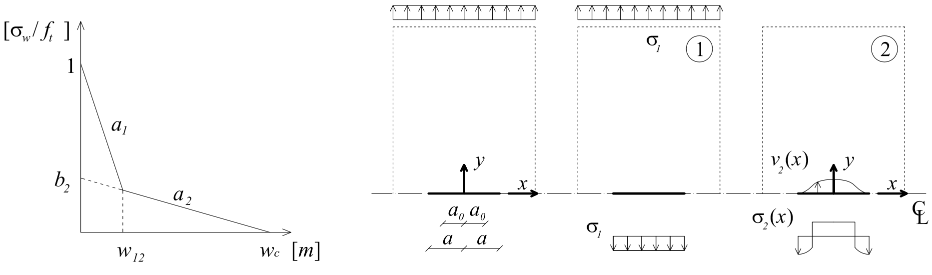

Figure 1. **A)** Average cohesive law for mortar. **B)** Geometry. **C)** Solution 1. **D)** Solution 2.

$$\frac{1}{2}w(x) = v_2(x,0) = -\int_{-a}^{a} \frac{2\sigma_2(\xi)}{\pi E'} \cosh^{-1} \frac{a^2 - \xi x}{a\,|x-\xi|}\, d\xi \qquad (4)$$

$$K_I = 0 = K_{I,2\pm a} = -\int_{-a}^{a} \frac{\sigma_2(x)}{\sqrt{\pi a}} \frac{\sqrt{a^2 - x^2}}{a \pm x} dx \quad (5)$$

Here ξ is the integration variable along the x-axis, $w(x)$ is the total crack opening, $\sigma_2(x)$ is positive as outward normal to the crack face, and $E' = E$ for plane stress. It is required that the superposition of the two fundamental solutions leads to equilibrium and bridging stresses in agreement with the applied cohesive law. Thus, $\sigma_2(x)$ can then be found:

$$\sigma_2(x) = \sigma_w(w(x)) - \sigma_1 \quad \text{with} \quad \sigma_w(x) = 0 \quad \text{for} \quad |x| \le a_0 \quad (6)$$

For any given crack length, $a > a_0$, it is possible to find a matching far-field stress, σ_1 by fulfilling (4), (5) and (6). The solution was found by numerical integration and using MATLAB's algorithms for solving non-linear equations. The displacement interpolation along the crack face was done using cubic splines. Due to symmetry, only half the crack was modeled and a numerical study showed that it was sufficient to use in the order of 14 discrete interpolation points.

4.1. Validation of the semi-analytical model

To validate the semi-analytical model, the results obtained for a simulation of a sheet of pure mortar were compared with the corresponding results from a FEM-model. The FEM model employed contains an interface in which the crack can propagate. The model has a height of 1000 mm and a width of 1200 mm and contains an initial slit-like center flaw with the length, $2a_0$ of 4 mm. The model consists of 30 x 206 (height x width) quadrilateral, 8 nodes plane stress elements. The element size increases by a factor of 1.03 from the flaw tip towards the edge along the width, and by a factor of 1.55 from the flaw towards the loaded edges along the height. In the FEM simulations, the boundary conditions along the two loaded edges resulted in a uniform displacement in the load direction along the width. The results from the simulation are shown in Figure 2.

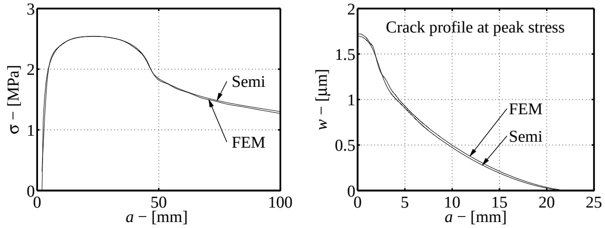

Figure 2. A) Half-crack length, a, and matching far-field stress, σ. **B)** Crack opening profile at peak stress.

As shown in Figure 2, the results from the two approaches were almost identical. The semi-analytical model was developed for center cracks only, so in the following, this model was employed for simulations of center cracks, while a FEM-model was employed for simulations of edge cracks.

4.2. LEFM versus the cohesive crack approach

A comparison between LEFM and the cohesive approach was performed for a single crack to assess the difference. Simulations of a crack propagating in mortar were carried out using the semi-analytical model as well as the Griffith theory. To investigate the influence of fibers, simulation of a crack propagating in ECC was also performed using the semi-analytical model. The cohesive laws related to the materials in the cohesive approach are shown in Figure 3 A). The Griffith simulation was done for mortar with a toughness equal to that used in the cohesive approach (K_{IC} = 660 kN/m$^{3/2}$). For both the mortar and the ECC, the results are for an infinite sheet containing an initial slit-like flaw of 4 mm ($2a_0$) loaded in uniaxial tension. In Figure 3 B), matching values of the half-crack length, a, and the applied load, σ, are shown. In Figure 3 C), the opening in the middle of the crack is shown during crack propagation for both the mortar and ECC.

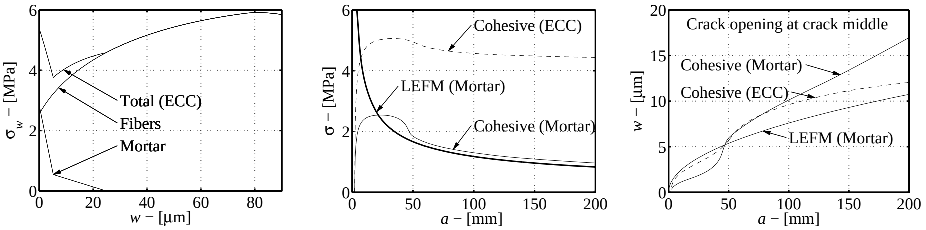

Figure 3. A) Average cohesive laws. **B)** Half-crack length, *a*, and matching far-field stress, σ. **C)** Crack opening at crack middle.

4.3. LEFM versus the cohesive crack approach – Discussion

A comparison of the Griffith and the cohesive approach for crack propagation in mortar shows that the Griffith approach predicts larger crack openings in pure mortar for crack lengths, *a*, up to 47 mm (see Figure 3 C)). After this crack length, the largest crack opening is predicted by the cohesive approach. Although the crack openings predicted by the two approaches do not match, they are of the same magnitude. For total crack lengths, 2*a* smaller than 400 mm, the predicted crack openings at crack middle are less than 20 μm.

The effect of adding fibers to the mortar is shown in Figure 3 B) and C). Crack propagation in mortar and ECC was simulated applying the cohesive approach. For crack lengths, *a*, up to 47 mm, the opening at crack middle was largest in the ECC material. This is due to the higher force needed to drive the crack in the ECC material (see Figure 3 B)). For crack lengths, *a*, larger than 80 mm, the crack opening is largest in the pure mortar material. The curve for the opening at crack middle has the same characteristic s-shape for both materials. Right after the peak stress has been reached, the slope of the crack opening curve increases. The slope declines but is still positive as the second branch of the two cohesive laws is reached (w = 5.2 μm). The second branch of the cohesive law *for the mortar* has a lower slope than the first, but it is still a softening branch. In contrast, the second branch of the cohesive law *for the ECC* is a hardening branch. This explains why the slope of the crack opening curve and the crack opening itself were smaller for the crack in the ECC material. For total crack lengths, 2*a*, smaller than 400 mm, flat-crack growth is not obtained with or without fibers.

According to the steady-state, flat-crack propagation criterion for multiple cracking, the complementary energy of the fibers has to be larger than the toughness of the mortar for the crack to propagate in a flat-crack mode. The total complementary energy, J'_b, for the fibers was 81.2 N/m and the mortar toughness, J_{tip}, was 14.05 N/m. In Figure 3 B), the peak stress for the ECC specimen occurred at a load of 5.06 MPa and a crack length, *a*, of 33.5 mm. At this point, the crack opening in the middle was 3.87 μm as shown in Figure 3 C) and 3.30 μm at x = 2 mm (the beginning of the cohesive zone). The utilized complementary energy at peak stress in a point at the beginning of the process zone was 0.75 N/m, which corresponds to only 5% of the mortar toughness. The crack opening has to be larger than 19 μm for complementary energy larger than the mortar toughness to be utilized in a point at the beginning of the process zone. For a total crack length, 2*a*, of 400 mm, the crack opening at crack middle was less than 15 μm.

5. Results and discussion

5.1. Influence of initial flaw size – Results

Simulations were performed for infinite ECC sheets containing initial flaws with various realistic lengths. The results are shown in Figure 4 and Figure 5 for center and edge cracks respectively. The entire length of the center flaw is denoted $2a_0$, while the entire length of the edge flaw is denoted a_0. Thanks to this definition, flaw lengths in the two situations can be directly compared.

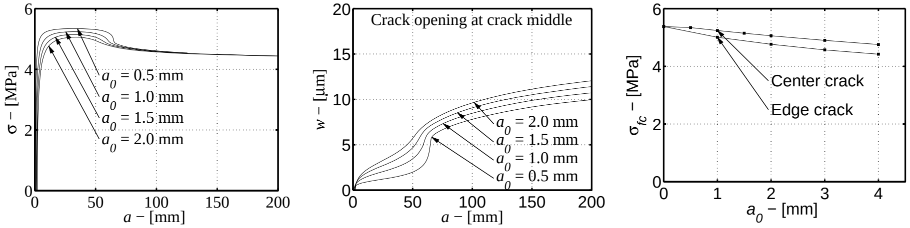

Figure 4. Influence of initial flaw length, a_0 – center crack. **A)** Half-crack length, *a*, and matching far-field stress, σ. B) Opening at crack middle, *w*, and matching half-crack length, *a*. **C)** Relationship between first-crack strength, σ_{fc}, and the initial flaw length, a_0.

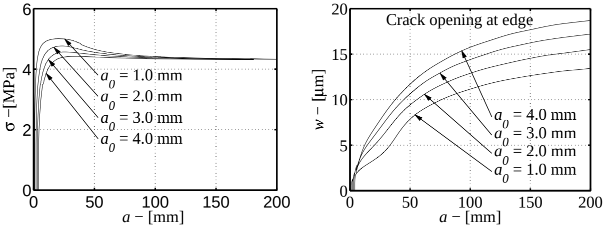

Figure 5. Influence of initial flaw length, a_0 – edge crack. **A)** Total crack length, *a*, and matching far-field stress, σ. B) Crack opening at the edge, *w*, and matching total crack length, *a*.

5.2. Influence of initial flaw size – Discussion

As shown by Dick-Nielsen (2004), increasing the length of the initial stress-free flaw results in a decrease in first-crack strength (peak stress – see Figure 4 C)). For center cracks, the decrease in first-crack strength is weak, while the decrease is a little more pronounced for edge cracks. Stability of crack propagation increases slightly with increasing flaw size, and again this effect is more pronounced for edge cracks. In the graph for the opening at crack middle, all the curves have the characteristic s-shape (see Figure 4 B) and Figure 5 B)). For crack lengths, *a* smaller than 200 mm, the maximal crack opening was less than 20 µm independent of crack position and initial flaw size. At no time during these crack propagations were the process zones fully evolved, which is the reason why LEFM cannot be used for crack propagation modeling.

5.3. Influence of the slope of the first linear branch of the cohesive law for the mortar a_1 – Results

The influence of the slope of the first linear branch of the cohesive law for the mortar, a_1, was investigated for infinite sheets (see Figure 6 A)). This was done by altering the shape of the cohesive law for the mortar: the opening, *w*, in the second point in the cohesive law was varied, while keeping the stress at this point fixed. The tensile strength, f_t, and the opening at the end of the cohesive law were kept fixed as well (shown in Figure 6 A)). The new cohesive laws for the ECC material are shown in Figure 6 B). The results from the crack propagation analysis are shown in Figure 7 and Figure 8 for center and edge cracks respectively.

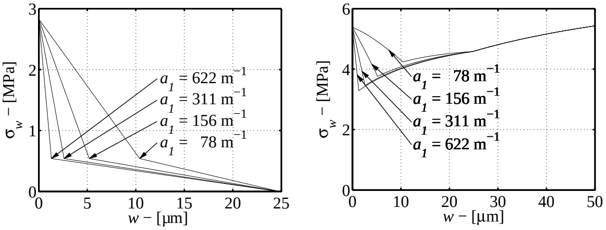

Figure 6. Cohesive laws for different slopes of the first linear branch of the cohesive law for the mortar, a_1 – cohesive stresses, σ_w and matching crack openings, w. **A)** Mortar. **B)** ECC.

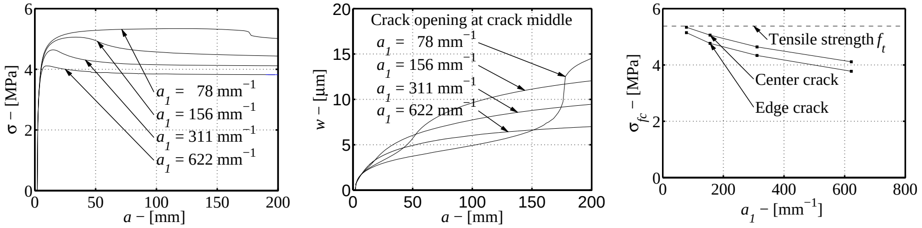

Figure 7. Influence of the slope of the first linear branch of the cohesive law for the mortar, a_1 – center crack. **A)** Half-crack length, a, and matching far-field stress, σ. **B)** Opening at crack middle, w, and matching half-crack length, a. **C)** Relationship between first-crack strength, σ_{fc} and a_1.

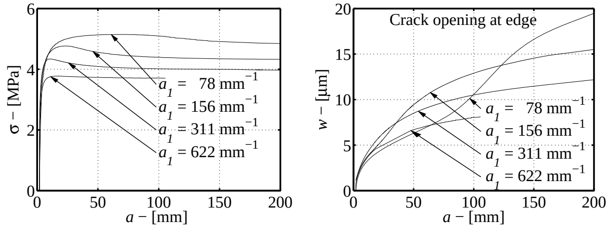

Figure 8. Influence of the slope of the first linear branch of the cohesive law for the mortar, a_1 – edge crack. **A)** Total crack length, a, and matching far-field stress, σ. **B)** Crack opening at the edge, w, and matching total crack length, a.

5.4. Influence of the slope of the first linear branch of the cohesive law for the mortar a_1 – Discussion

As shown in Figure 7 C), the first-crack strength decreases as a_1 increases. The decrease in the first-crack strength was independent of the position of the initial flaw. As shown in Figures 7A and 8A, the stability of crack growth decreases with increasing slope. In Figure 7 B) and Figure 8 B), the opening in the middle of the crack during crack propagation is shown. When interpreting these results, one should keep in mind that the hardening branch in the cohesive laws begins at the following openings for the respective cohesive laws: 1.3 μm, 2.6 μm, 5.2 μm and 10.4 μm. All the curves showing the evolution of the crack opening with crack length still have the characteristic s-shape. For the analysis with the slope, a_1 of 311 mm^{-1} and 622 mm^{-1}, the *s*-shape is not as pronounced as is the case for the two other slopes. This is caused by the fact that the hardening branch for the cohesive law for the ECC material for larger values of a_1 takes over at relatively small crack openings.

When we alter the slope of the first linear branch of the cohesive law for the mortar, a_1, in the manner described, the toughness of the mortar is altered as well. An increase in a_1 results in a decrease in mortar toughness. According to the criterion related to steady-state, flat-crack propagation, a decrease in mortar toughness should increase the chances for the crack propagating in a steady-state flat-crack mode and thus increase the chances of multiple cracking. As shown in Figure 7 B) and Figure 8 B), an increase in a_1 results in smaller crack openings, but generally only for relatively large crack lengths, with a larger than 100-200 mm. All crack openings in the analysis presented here are smaller than 20 μm.

5.5. Influence of tensile strength of the mortar – Results

A series of analyses were conducted to investigate the influence of the tensile strength of the mortar for infinite sheets. In the simulations, the second branch of the cohesive law, characterized by constants a_2, b_2, was held constant, while the tensile strength, f_t and thereby a_1 varied, keeping the mortar toughness, J_{tip} fixed. The cohesive laws for the mortar and for the ECC are shown in Figure 9. The results from the analysis are shown in Figure 10 and Figure 11 for center and edge cracks respectively.

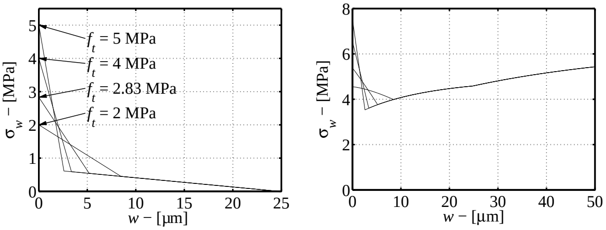

Figure 9. Average cohesive laws for different mortar tensile strength, f_t, keeping the mortar toughness constant. **A)** Mortar. **B)** ECC.

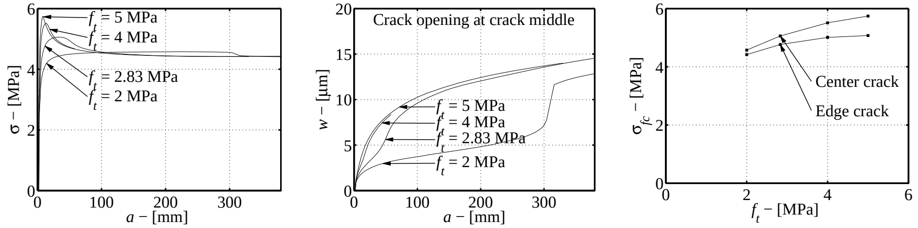

Figure 10. Influence of the tensile strength of the mortar, f_t, keeping the mortar toughness constant – center crack. **A)** Half-crack length, a, and matching far-field stress, σ. B) Opening at crack middle, w, and matching half-crack length, a. **C)** Relationship between first-crack strength, σ_{fc}, and the tensile strength of the mortar, f_t.

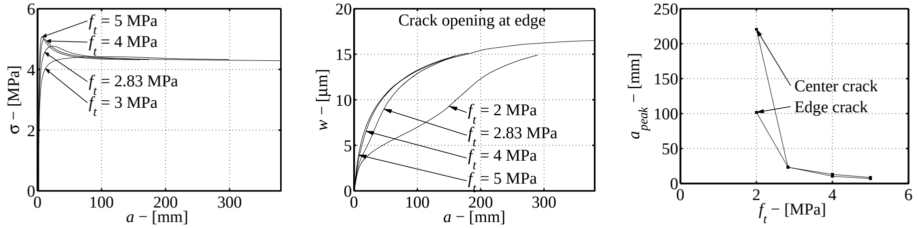

Figure 11. Influence of the tensile strength of the mortar, f_t, keeping the mortar toughness constant – edge crack. **A)** Total crack length, a, and matching far-field stress, σ. B) Crack opening at the edge, w, and matching total crack length, a. C) The relationship between the crack length at first-crack strength, a_{peak}, and the tensile strength of the mortar, f_t. a_{peak}, is the half-crack length for center cracks and the total length for edge crack.

5.6. Influence of tensile strength of the mortar – Discussion

When the tensile strength of the mortar increases, the first-crack strength increases as well (see Figure 10 C)). The increase for the center crack is most pronounced. An increase in the tensile strength results in larger crack openings for small crack lengths (see Figure 10 B) and Figure 11 B)). This is caused by the fact that the mortar toughness is fixed and an increase in tensile strength results in a larger part of the fracture energy being associated with the first, very small crack opening (see Figure 9 A)). This increase in fracture energy associated with a small crack opening, results in an increase in the force required to drive the crack and thus larger crack openings for small crack lengths. For larger crack lengths, the load/crack-length curves gradually coincide. Within the analyzed interval of crack length, the process zone is not fully evolved, but when the hardening part of the cohesive law begins to have a larger influence, the crack openings begin to coincide as well.

As shown in Figure 10 and Figure 11 A+B), the effect of tensile strength vanishes for large crack lengths. For crack lengths smaller than 300 mm, the tensile strength of the mortar, and thereby the shape of the cohesive law, has a large influence on the crack opening during crack propagation. The conventional steady-state, flat-crack criterion deals only with fracture energy and not the shape of the cohesive law because the criterion is based on LEFM, in which the entire energy is dissipated in a point. This criterion is therefore valid for brittle materials, but because the process zone in this analysis reaches lengths of over 300 mm, the shape of the cohesive law becomes important.

In Figure 11 C), the crack length at peak stress, a_{peak}, is plotted as a function of the tensile strength of the mortar. Here a_{peak} is half the crack length for center cracks and the total length for edge cracks. For a mortar with high tensile strength, the crack propagation becomes highly unstable for relatively small crack lengths (less than 23 mm), while the crack propagation remains stable up to relatively large crack lengths for mortars with small tensile strength. This means that if a mortar with low tensile strength is tested, only stable crack growth will appear for normal-sized test specimens.

5.7. Influence of fiber type – Results

In the analysis above, the cohesive law for the mortar has been investigated. According to the criteria for multiple cracking, a large complementary energy of the fibers is preferable in the process of achieving strain-hardening. In this series of analyses, the complementary energy of the fibers was varied. The new fiber curve was obtained by scaling the w-axis by a factor 0.5 (see Figure 12 A)). The fibers applied so far are referred to as type 1 and the new fibers as type 2. The cohesive laws for the fibers and ECC are shown in Figure 12 A). The results from the analysis are shown in Figure 12 B) and C). The simulations were only performed for center cracks.

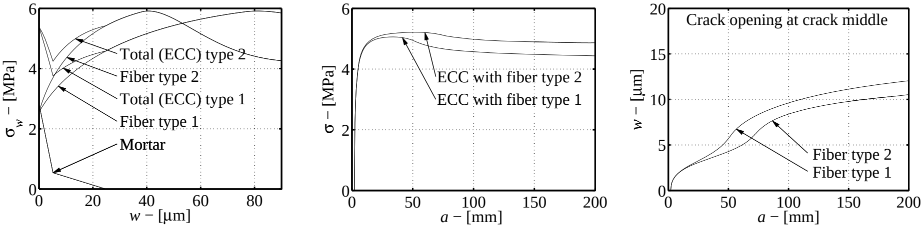

Figure 12. A) Cohesive laws for fibers and ECC **B)** Half-crack length, a, and matching far-field stress, σ. **C)** Opening at crack middle, w, and matching half-crack length, a.

5.8. Influence of fiber type – Discussion

In this analysis, the complementary energy was reduced to see whether this would have a negative influence on the chances of achieving steady-state, flat-crack propagation. Although the total complementary energy for fiber type 2 was reduced, the utilized complementary energy for fiber type 2 for small crack openings was larger than for fiber type 1 due to the higher slope at the beginning. The first branch of the cohesive law for the ECC was raised and the slope of the second branch was increased. This resulted in higher first-crack strengths and smaller crack openings. This tendency was also observed in tests performed by Li et al. (2002), where a reduction in complementary energy led to an increase in first-crack strength. To make use of complementary energy larger than the mortar toughness at a point at the beginning of the process zone, the crack opening in the ECC-material containing fiber type 2 has to be larger than 16 μm. For crack lengths, *a*, smaller than 200 mm, the opening at crack middle is less than 11 μm. Reducing the complementary energy leads to an increase in crack propagation stability according to Figure 12B).

5.9. Influence of specimen geometry – Results

To investigate the influence of finite specimen geometry, six new FEM-models were employed. The material properties in all models are the same as in the original analysis presented in section 3. Like the previous FEM simulations, the boundary conditions along the two loaded edges result in a uniform displacement in the load direction along the width. When the influence of the specimen geometry was investigated, the finite sheet with the dimensions 30 mm x 80 mm (breadth/width x height) was taken as a point of reference. These dimensions were chosen so that they match the dimensions of the instrumented part of test specimens in the JSCE – Tentative Guideline for Design and Constructions of Engineering Cementitious Composites – ECC (2005). In Figure 13 A) and B), results for various geometries are shown for a center crack and an edge crack respectively. The center flaws all have a total length, $2a_0$ of 4 mm, while the edge flaws have a total length, a_0, of 2 mm. In Figure 13 C), the opening at crack middle is shown for various crack lengths, for both a finite geometry and an infinite geometry.

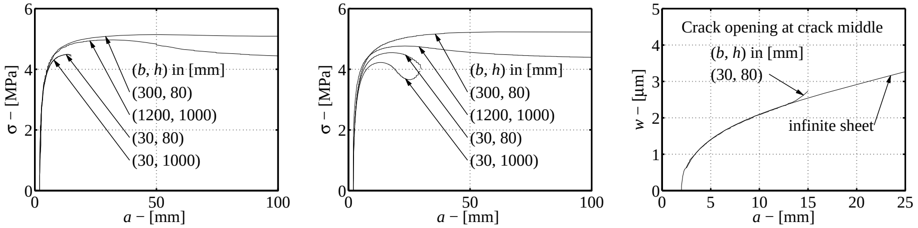

Figure 13. Influence of geometry. **A)** <u>Center crack</u> – Half-crack length, *a*, and matching far-field stress, σ. B) <u>Edge crack</u> – Total crack length, *a*, and matching far-field stress, σ. **C)** <u>Center crack</u> – Opening at crack middle, *w*, and matching half-crack length, *a*.

5.10. Influence of specimen geometry – Discussion

For center cracks and edge cracks in the sheet with dimensions 30 mm x 80 mm (width x height) the force needed to drive the crack is small compared to the corresponding force for an infinite sheet; see Figure 13 A) and B). This is due to the smaller stiffness, caused by the small width in the finite sheet. If we keep the width fixed at 30 mm and increase the height to 1000 mm, the results do not change for the center crack. For the edge crack, increasing the height causes the first-crack stress, σ_{fc}, to decrease by 7%. If we increase the height, the model becomes less stiff, caused by the increased distance to the fixed boundaries. Due to the symmetry of the center crack model, it is not sensitive to the change of stiffness. If we keep the height fixed at 80 mm and increase the width to 300 mm, the first-crack strength in both models increases, compared to that obtained for a width of 30 mm. This is due to the fact that the stiffness is increased and for these dimensions the center crack model is affected as well. In all cases, crack propagation stability increases with increasing first-crack strength.

In Figure 13 C), the opening at crack middle during crack propagation is shown for the infinite sheet containing a center crack and for a sheet with the dimensions 30 mm x 80 mm. As shown in the figure, the opening at crack middle in the finite sheet is identical to the opening in the infinite sheet up to a crack length, *a*, of 13 mm. After this crack length, the opening in the finite sheet becomes larger than that in the infinite sheet. This was expected due to the stiff boundary conditions and small width of the finite specimen. At a crack length, *a*, of 15 mm in the finite sheet, the crack has run through the sheet.

5.11. Influence of boundary conditions – Results

A series FEM of simulations were conducted to investigate the influence of the boundary conditions of the test specimen. A sketch of the test setup employed is shown in Figure 14. It is basically similar to the setup employed by the JSCE (2005). There is a hinge at the end of each bar (A and B). The rotation in these hinges can be fixed or free.

The FEM mesh employed is shown in Figure 15 (due to symmetry only half the model is shown). It is assumed that the displacement of the specimen within the steel jaws is fixed. In the FEM model, this part is modeled by a series of rigid bars. The steel bars from the jaws to the hinges have a diameter d_b. The dog-bone specimen has a thickness of 13 mm and is modeled by plane stress elements. The width of the center part of the dog-bone specimen is 30 mm and the ends have a width of 60 mm. To obtain a fine mesh near the crack and a coarse mesh near the ends, a series of triangular element rows were employed. The model employed has 16 elements along the width in the coarse part and 128 elements in the fine part. The fine mesh consists of 10 elements along the height on each side of the symmetry line and each of these elements has a height of 0.63 mm.

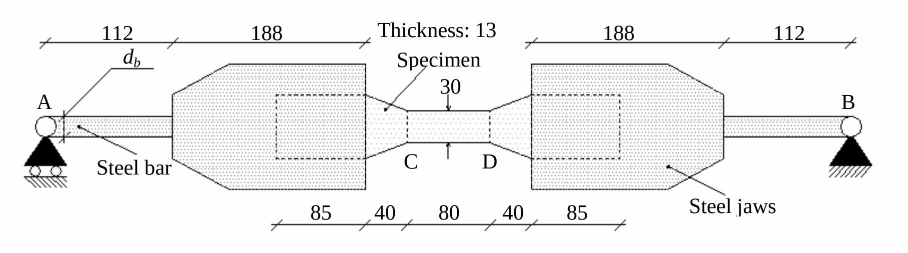

Figure 14. Test set-up – all dimensions in [mm].

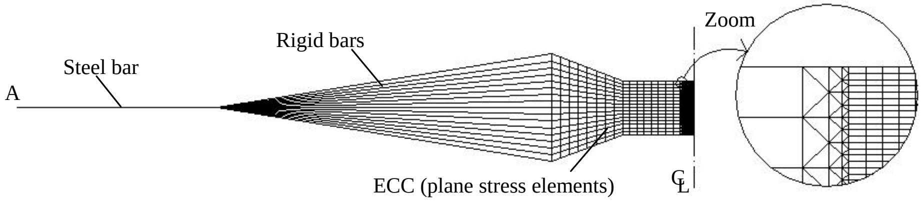

Figure 15. The FEM mesh employed for the dog-bone specimen.

Due to double symmetry in the model containing the center flaw, this model cannot react to the hinges in the setup, therefore only specimens containing edge flaws were simulated. In Figure 16, matching values of the total crack length, a, and the far-field stress, σ, are plotted. The far-field stress in these simulations refers to the average stress in the section between the inclined and narrow part. For comparison, the results from the rectangular sheets with a width of 30 mm and heights of 80 mm and 1000 mm have been plotted as well (from the previous section). For the rectangular sheets, the boundary conditions along the two loaded edges result in a uniform displacement in the load direction along the width.

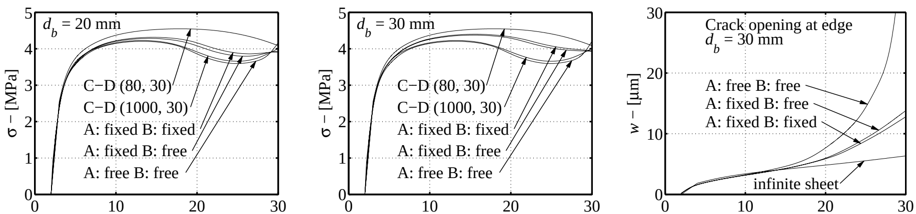

Figure 16. Total crack length, a, and matching far-field stress, σ. There are 5 simulations for each diameter, d_b: 3 simulations for different adjustments of the hinges (dog-bone specimens) and 2 simulations where only the part between C and D (Figure 14) were modeled and the loaded boundaries are here rigid (these results are taken from Figure 13 b)) A). d_b = 20 mm B). d_b = 30 mm. C). Crack opening at the edge, w, and matching total crack length, a – d_b = 30 mm.

5.12. Influence of boundary conditions -- Discussion

In Figure 16 A), results from the dog-bone test setups with a bar diameter, d_b of 20 mm are compared to results obtained from the rectangular sheets whose boundary conditions along the two loaded edges result in a uniform displacement in the load direction along the width. The results from the dog-bone simulation with free-free rotations at the hinges are very similar to those obtained from the rectangular sheet with the dimension 30 mm x 1000 mm (width x height). Although the displacements are fully fixed at the ends of the rectangular sheet, the large height reduces the bending stiffness of the specimen. When the rotations are fixed-fixed or fixed-free in the hinges, the setup becomes stiffer and the first-crack strength increases approximately 2% compared to that obtained with free-free rotations. The simulations show that one fixed hinge is sufficient to control the rotation at the hinges. The results from the rectangular sheet with the dimensions 30 mm x 80 mm (width x height) show a first-crack strength approximately 8% higher than that obtained for the free-free model. Because of the imposed boundary conditions, the small rectangular sheet is the stiffest test setup one can obtain when the instrumented part has these dimensions, and it was therefore expected that the first-crack strength here would be the highest. An important tendency that can be concluded from Figure 16 A) is that the stiffer the boundary conditions the more stable the crack growth.

In Figure 16 B) results are shown for simulations employing a bar diameter of 30 mm. Increasing the bar diameter by 50% does not change the results for the model with the free-free hinges. As long as the hinges are free-free, the stiffness of the test setup does not play a role, the rotation will take place in the hinges leaving the bars straight. In the simulations where the rotations at the hinges are fixed-free or fixed-fixed, the increased stiffness increases the first-crack strength by approximately 2% compared with those obtained when the diameter was 20 mm. As the bar diameter increases, the results get closer to those obtained for the rectangular sheet with the dimensions 30 mm x 80 mm (width x height). In Figure 16 C), the crack opening, *w*, at the edge is plotted as a function of the crack length, *a*, for a bar diameter of 30 mm. The openings are compared with the corresponding opening for an infinite sheet (taken from Figure 13 B)). For crack lengths less than 13 mm, the crack openings in the four simulations are almost identical. For larger crack lengths, the opening at the edges in the dog-bone specimens becomes significantly larger than the corresponding opening in the infinite sheet due to the smaller stiffness in the dog-bone test setup. When at least one hinge is fixed, the opening increases by a factor of 2.2 compared with the corresponding opening for the infinite sheet for a crack length of 30 mm. When both hinges are free the opening for a crack length of 30 mm increases by a factor of 7.7 compared with the opening in the infinite sheet. This means that potential strain-hardening may be hindered by flexible boundary conditions simply due to the large crack openings experienced during crack propagation.

6. Conclusions and discussion

In the present investigation, conditions for strain-hardening in ECC materials were investigated. The investigation was based on the assumption that mortar crack propagation is adequately described by cohesive fracture mechanics in the form of the FCM and that a cohesive law for the composite can be constructed through the superposition of the mortar cohesive law and the fiber-bridging curve. In both the present analysis and in the derivation of the steady-state, flat-crack propagation criterion, the propagation of just one crack is examined. When ECC undergoes strain-hardening, an interaction between the cracks takes place, which is not taken into consideration in this analysis. However, the analysis relies on the implicit assumption that when the first-crack strength (peak far-field stress) is less than the peak fiber-bridging stress, and when the first crack propagates with crack openings less than the deformation associated with the peak on the fiber-bridging curve, then the fiber-bridging stress eventually is able to produce more cracks adjacent to the first and thus create multiple cracking and strain hardening.

A comparison between the LEFM approach and the cohesive approach for crack propagation in mortar was made. The magnitude of the crack openings were the same, but the far-field stress and the sensitivity to initial flaw size were significantly different. For crack lengths, *a*, up to 200 mm, the crack openings found were less than 20 μm.

It was found that during crack propagation the opening at crack middle in pure mortar was larger than the corresponding opening in ECC material, but only for crack lengths, a, longer than 80 mm. For crack lengths in the investigated range, the addition of fibers to the mortar did not make the crack propagate in a steady-state mode. In the analysis with the original material parameters, the utilized complementary energy in a point at the beginning of the process zone at peak stress and at a crack length, a, of 200 mm only amounted to 5% and 47% of the toughness of the mortar respectively. The steady-state crack propagation criterion states that the crack will propagate in a steady-state flat-crack mode when the complementary energy of the fibers is larger than the toughness of the mortar. According to the cohesive approach, utilizing complementary energy of the same order of magnitude as the mortar toughness will not occur for crack lengths, a, smaller than 200 mm. This means that the steady-state crack criterion cannot be proved experimentally by using test specimens of normal size. With the finite dimensions of the sheet, the load/crack-length curves alter the crack opening, but the opening at crack middle is still of the same magnitude. The boundary conditions of the applied test specimen, on the other hand, have an influence on the crack openings observed during crack propagation and potential strain-hardening may be hindered by flexible boundary conditions due to the large crack openings experienced during crack propagation.

A parameter study of the influence of initial flaw sizes, the initial slope a_1 of the cohesive law for the mortar, the tensile strength of the mortar, and the fiber type was performed. The study showed that first-crack strength and the evolution of the opening at crack middle are influenced primarily by the cohesive law of the mortar and the fiber-bridging curve and only weakly by the initial flaw size, Reducing the mortar toughness (keeping the tensile strength constant) and reducing the tensile strength (keeping the toughness constant) both promote multiple cracking because the first-crack strength of the ECC material is reduced. Increasing initial flaw size was found to have a weak reducing effect on the first-crack strength. The complementary energy of the fiber-bridging curve was found to have little influence on the multiple cracking potential, as long as the deformation at peak stress on the fiber-bridging curve was kept larger than the maximum crack opening during propagation. The maximum crack opening observed during crack propagation in various test specimen geometries was small, typically less than 20 μm, and also small compared to typical deformations at peak bridging stress.

The investigated parameters all had an influence on the stability of crack propagation in the ECC material. In particular, tensile strength had a pronounced influence on the crack length at first-crack strength (peak far-field stress). However, the significance of stability of crack growth and its influence on multiple cracking is not clear and cannot be assessed with the present models.

7. Acknowledgements

The authors acknowledge fruitful discussions with Professor V.C. Li on the subject during his various stays at the Department of Civil Engineering, Technical University of Denmark.

Notation

The following symbols are used in this paper:

E = Elastic modulus
G_d = Chemical bond strength of the fiber/mortar interface
G_f = Fracture energy of mortar
J'_b = Complementary energy of the fiber-bridging curve
J_{tip} = Mortar toughness,
K_{IC} = Critical mode I stress intensity factor
L_f = Fiber length
a = Crack length
a_0 = Initial stress-free crack length
a_1 = Negative slope of the first linear part of the cohesive law for the mortar (normalized with the tensile strength)
a_2 = Negative slope of the second linear part of the cohesive law for the mortar (normalized with the tensile strength)
a_{peak} = Crack length at peak stress
b_2 = The cut-off on the x-axis (stress normalized with the tensile strength) of the second linear part of the cohesive law for the mortar
d_f = Fiber diameter
d_b = Diameter of steel bar
f = Fiber snubbing coefficient
f' = Fiber strength reduction coefficient
f_t = Tensile strength of mortar
v = Displacement of the crack surface ($v = \frac{1}{2} w$)
v_f = Fiber volume fraction
w = Crack opening
w_0 = Crack opening at peak load
x = Axis in the crack parallel with the crack direction
β = Slip-hardening coefficient for the fiber/mortar interface
ξ = Integration variable along the x-axis
σ = Far-field stress
σ_0 = Far-field stress at peak load
σ_{fc} = First-crack strength (peak stress)
σ_{fu} = In-situ fiber strength
$\sigma(x)$ = Stresses along the crack face
τ_0 = Frictional stress on the fiber/mortar interface

References

Barenblatt, G.I., 1962. “The Mathematical Theory of Equilibrium Cracks in Brittle Fracture.” *Adv. Appl. Mech.* **7**, 56–129.

Dick-Nielsen, L., Poulsen, P.N., Stang, H., Olesen, J.F., 2004. “Semi-analytical cohesive crack model for the analysis of first crack strength of mortar.” *Proc. of the 17th Nordic Seminar on Computational Mechanics*. (Eds A. Eriksson, J. MÅnsson and G. Tibert). 183-186.

Dick-Nielsen, L., Stang, H., Poulsen, P.N., 2005. “Micro-mechanical Analysis of Fiber Reinforced Cementitious Composites using Cohesive Crack Modeling.” *Proc. of the Knud Højgaard conference*. (Eds. O.M. Jensen, M. Geiker and H. Stang). 277-292.

Dugdale, D.S., 1960. “Yielding of Steel Sheets Containing Slits.” *J. Mech. Phys. Solids*, **8**, 100-104.

Griffith, A.A., 1920. “The phenomena of rupture and flow in solids.” *Phil Trans Roy Soc London*. **A221**, 163-198.

Hillerborg, A., Modeer, M., Petersson, P.E., 1976. “Analysis of Crack Formation and Crack Growth in Concrete by Means of Fracture Mechanics and Finite Elements.” *Cem. Concr. Res*. **6**, 773-782.

JSCE, 2005. “Tentative Guideline for Design and Constructions of Engineering Cementitious Composites-ECC.” (Draft). JSCE TC, 334.

Li, V.C., 1992. “Performance Driven Design of Fiber Reinforced Cementitious Composites.” *Proc. of 4th RILEM International Symposium on Fiber Reinforced Concrete.* (Ed. R. N. Swamy), Chapman and Hall. 12 – 30.

Li, V.C., 1998. “Engineered Cementitious Composites – Tailored Composites Through Micromechanical Modeling.” *In: Fiber Reinforced Concrete: Present and the Future.* (Ed. N. Banthia, A. Bentur, A. and A. Mufti). Canadian Society for Civil Engineering, Montreal. 64-97.

Li, V.C., 2003. “On Engineered Cementitious Composites (ECC) – A Review of the Material and its Applications.” *J. Advanced Concrete Technology*, **1**, (3), 215-230.

Li, V.C., Leung, C.K.Y., 1992. “Steady State and Multiple Cracking of Short Random Fiber Composites.” *ASCE J. Eng. Mech*. **188**, 2246-2264.

Li, V.C., Stang, H., Krenchel, H., 1993. “Micromechanics of Crack Bridging in Fiber Reinforced Concrete.” *Materials and Structures*. **26**, 486-494.

Li, V.C., Wu, C., Wang, S., Ogawa, A., Saito, T. 2002. “Interface Tailoring for Strain-hardening Polyvinyl Alcohol-engineered Cementitious Composite (PVA-ECC).” *ACI Material Journal*. **99**(5), 463-472.

Lin, Z., Kanda, T., Li, V.C., 1999. “On interface property characterization and performance of fiber-reinforced cementitious composites.” *Concrete Science and Engineering*. **1**, 173-184.

Marshall, D.B., Cox, B.N., 1988. “A J-integral method for calculating steady-state matrix cracking stresses in composites.” *Mech. Mat*. **8**, 127-133.

Naaman, A.E. and Reinhardt, H.W. 1996. “Characterization of High Performance Fiber Reinforced Cement Composites.” *In: High Performance Fiber Reinforced Cement Composites 2 (HPFRCC 2) Proc. of the Second International RILEM Workshop*. (Eds. A.E. Naaman and H.W. Reinhardt). E&FN Spon, 1-24.

Stang, H. 1992. “Evaluation of Properties of Cementitious Fiber Composite Materials. In High Performance Fiber Reinforced Cement Composites.” In: High Performance Fiber Reinforced Cement Composites. *Proc. of the International RILEM/ACI Workshop.* (Eds. H.W. Reinhardt and A.E. Naaman). E&FN Spon, 388-406.

Tada, H., 1985. “The stress analysis of crack handbook.” Second edition. Paris Production Incorposloped, Missouri.

Van Mier, J.G.M., 2004. ”Reality Behind Fictitious Cracks?” In: Fracture Mechanics of Concrete Structures, Volume I. (Eds. V.C. Li, C.K.Y. Leung, K.J. Willam, S.L. Billington). Ia-FraMCos. 11-30.

Walter, R., Olesen, J.F., Stang, H.,Vejrum, T., 2007. ”Analysis of an Orthotropic Deck Stiffened with a Cement-Based Overlay.” *Journal of Bridge Engineering*, **12**(3), 350-363.

Wang, S., 2004. Private communications. DTU.

Wang, S. and Li, V.C. 2006. “High-Early-Strength Engineered Cementitious Composites.” *ACI Materials Journal*. **103**(2), 97-105.

Østergaard, L., 2003. “Early-Age Fracture Mechanics and Cracking of Concrete.” Ph.D. Thesis. Printed by DTU-Tryk. Department of Civil Engineering, Technical University of Denmark.

Paper IV

A Plastic Damage Mechanics Model for Strain-Hardening Fiber-Reinforced Cementitious Composite, Part I: Theory

Submitted to: *Journal of Engineering Mechanics*

A Plastic Damage Mechanics Model
for Strain-Hardening Fiber-Reinforced Cementitious Composite
Part I: Theory

L. Dick-Nielsen [1]

H. Stang [2]

P. N. Poulsen [3]

P. Kabele [4]

Abstract: This article discusses the establishment of a plasticity-based damage mechanics model for Strain-Hardening Fiber-Reinforced Cementitious Composites (SHFRCC). The present model differs from existing models by combining a matrix crack and a fiber-bridging model to describe the behavior of SHFRCC material. The model provides information about crack opening, orientation and spacing, which makes it possible to assess the condition of a structure. A simple simulation is performed to demonstrate the capability of the model.

CE Database subject headings: Fracture Mechanics, Cracking, Finite element method, Constitutive equations, Concrete, Cements, Cohesion, Fiber-reinforced materials, Strain hardening.

---

[1] Ph.D.-student, Department of Civil Engineering, Technical University of Denmark, building 118, 2800 Kgs. Lyngby, Denmark. E-mail: ldn@byg.dtu.dk

[2] Professor, Department of Civil Engineering, Technical University of Denmark, building 118, 2800 Kgs. Lyngby, Denmark. E-mail: hs@byg.dtu.dk

[3] Associate professor, Department of Civil Engineering, Technical University of Denmark, building 118, 2800 Kgs. Lyngby, Denmark. E-mail: hs@byg.dtu.dk

[4] Associate professor, Faculty of Civil Engineering, Czech Technical University in Prague, Czech Republic. E-mail: petr.kabele@fsv.cvut.cz

1 INTRODUCTION

In contrast to conventional Fiber-Reinforced Concrete (FRC), Strain-Hardening Fiber-Reinforced Cementitious Composite (SHFRCC) is characterized by its ability to undergo multiple cracking in tension. Conceptually, the cementitious matrix in SHFRCC is assumed to contain initial flaws which are randomly distributed throughout the composite material. Micro-cracks start to develop from the initial flaws due to stress concentration at the tip of the flaws when the material is loaded in tension. Micro-cracks form and propagate under increasing load and, together with fiber-bridging in the cracks, give rise to multiple cracking and strain-hardening. Investigations into the conditions in which matrix and fiber properties achieve strain-hardening through multiple cracking have been carried out by a number of authors, see e.g. (Naaman 1987), (Li & Leung 1992), (Li & Chan 1994), (Leung 1996), (Kanda & Li 1999), (Dick-Nielsen, Stang & Poulsen 2006*a*) and (Dick-Nielsen, Stang & Poulsen 2007).

Thanks to the strain-hardening behavior of SHFRCC material, smeared-crack models available in commercial Finite Element Method (FEM) programs can be used to simulate the behavior of SHFRCC structures (Dick-Nielsen, Stang & Poulsen 2006*b*). An overview of smeared models is given by Jirasek (2004). An example of a model specifically developed for SHFRCC is that derived by Han, Feenstra & Billington (2003). This model is a total-strain, rotating smeared-crack model. The model is characterized by its detailed description of the unloading phase, which makes it suitable for cyclic loading simulations. In the SHFRCC model proposed by Kabele (2002), the cracks are fixed, once initiated. The model is characterized by the scheme used to describe resistance against relative sliding of crack surfaces. This resistance is assumed to occur solely due to fiber bridging, while fibers are described as randomly oriented Timoshenko beams.

A number of finite element simulations on the micro- and meso-scale have been carried out in previous investigations by the authors. These simulations were performed to get a better understanding of the strain-hardening process in SHFRCC. On the micro-scale, the mechanism during micro-crack propagation and subsequent fiber-debonding and pull-out has been investigated (Dick-Nielsen, Stang & Poulsen 2005). On the meso-scale, investigations on the propagation of single and multiple cracks have been carried out (Dick-Nielsen et al. 2006*a*), (Stang, Olesen, Poulsen & Dick-Nielsen 2007) and (Dick-Nielsen et al. 2006*b*). On this scale, it was found that matrix cracks can reach significant lengths before they become stress-free. For a material model to be effective in the state where the matrix cracks initiate and propagate, a separate matrix crack and fiber-bridging description is needed. The present model is based on the smeared, fixed, multiple-cracking approach. The model differs from existing models by describing the behavior of the cracks through a separate matrix crack and fiber-bridging model and by giving detailed information on crack opening and spacing.

The matrix crack is described by employing an elasto-plastic material model for damage initiation and propagation, which is a modified version of a model originally developed by Carol, Prat & López (1997) for plain concrete. The model employs a modified Mohr-Coulomb yield surface, which enables a mixed-mode cohesive description of the cracks. Although the fracture energy of the SHFRCC matrix is low, it has been shown in (Stang et al. 2007) that it is best described by a cohesive approach. During the sliding of a crack, the model is able to capture the dilation in the normal direction. For the fibers, the normal stiffness is described using a multi-linear strain-stress curve which can be found from a uniaxial tensile test. The shear stiffness of fiber bridging has been described as randomly oriented Timoshenko beams bridging the crack (Kabele 2002).

The present article is the first of two companion articles. In the first article the plasticity-based damage mechanics model for the macro-scale is derived. The theory is described in detail and the model is demonstrated using a simple example. In the second article the capability of the model is demonstrated by comparing simulation results with experimental results. Furthermore, the use of the model in material design is demonstrated by means of a parameter study.

2 PLASTICITY DAMAGE MODEL

The behavior of the SHFRCC material in the present model is based on the concept of a Representative Volume Element (RVE). An RVE is traditionally thought of as an element containing a sufficiently large number of microstructural inhomogeneities for it to be considered macroscopically homogeneous. The RVE concept is not adequate as long as the number of cracks is small, but the concept is employed for lack of a better. As the number of cracks increases, the concept becomes more adequate. Here, a two-dimensional RVE in plane stress with the side length, l, is considered. For the model to be effective the length, l, must be large enough to ensure that the RVE contains a sufficient number of parallel cracks in the strain-hardening phase. In this way, the RVE can be considered as a material point, where the constitutive equations are solved. The RVE is subject to average total stress, $\boldsymbol{\sigma}$, and strain, $\boldsymbol{\varepsilon}$, and can contain several series of parallel multiple cracks, where each series has different orientation. In this section, the constitutive equations for an RVE containing multiple cracks in multiple directions will be derived for the elastic and plastic states.

2.1 Model input

As input to the model, data on the composite level, the fibers and the matrix are required.

On the composite level, the following data are needed (see figure 1): the initial E-modulus, E_0, Poisson's ratio, ν, the tensile strength, $f_{t,SH,0}$, a constant, b, that describes the crack opening at which the crack becomes stress-free during unloading, and the threshold angle, ϕ, which limits the angle between two crack systems. This threshold angle must be related to physical observations. Furthermore, the relationship between the total normal strain, ε, and the normal stress, σ, is required. Figure 1 shows the uniaxial tensile response for the SHFRCC material up to localization. In the figure, the normal stress in the matrix crack and fiber-bridging stress on a crack surface are plotted as a function of the normal strain. It is assumed that all cracks in one direction associated with a material point have the same crack opening, $\boldsymbol{\delta}$. Interaction between micro-cracks and initial defects leads to a jagged strain-stress relationship (Dick-Nielsen et al. 2006*b*), which has also been observed in tests (Wang & Li 2004). To avoid numerical problems during computations, an idealized smooth curve is employed as shown in the figure, and interactions between micro-cracks are therefore not considered in the present model. The tensile curve for the SHFRCC material can be found from a uniaxial tensile test or through a four-point bending (FPB) test and an inverse analysis (Østergaard 2003). Furthermore, the length of the RVE, l, should be related to the test specimen from which the uniaxial stress-strain relationship was found. The length should be chosen so that the RVE contains a sufficient number of cracks. Finally, a crack evolution law giving the relationship in the RVE between the total normal strain and the number of parallel cracks per length, n, is needed (see figure 2). The crack evolution law has to be continuous, since a smooth overall stress-strain response is aimed for. It is assumed that the dependency between the number of cracks per length, n, and the normal strain can be described by a piecewise linear relationship. The crack evolution law creates a link between the behavior of a single crack, the (δ, σ)-relationship, and the behavior of the continuum, the (ε, σ)-relationship. In the current version, the crack evolution law was calibrated through experiments. Examples of micro-mechanical models for the crack evolution law can be found in the literature, see e.g. (Aveston, Cooper & Kelly 1971) and (Wu & Li 1995).

For the fibers the following input is needed: a shear stiffness constant, k, which gives the relationship between crack opening and sliding and the shear bridging stress. This constant depends on the fiber volume fraction, V_f, the shear modulus for the fibers, G_f, and the shape of the fibers (Kabele 2002). The shear stiffness constant must be calibrated through experiments.

The material parameters required for the matrix are the tensile strength, $f_{t,0}$, the cohesion, c_0, two friction coefficients for the yield surface, μ_f, and μ_0, a friction coefficient for the plastic potential, $\mu_{g,0}$, and the mode I and II fracture energy, $G_{F,I}$, and $G_{F,II}$.

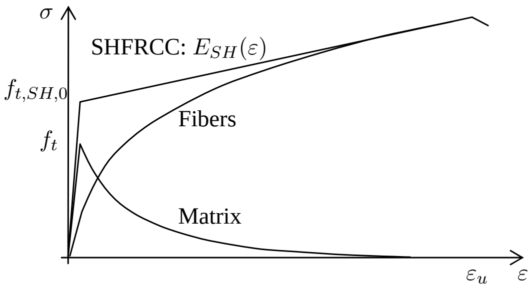

Figure 1: The relationship between the normal strain and normal stress in the continuum, the stress in the matrix crack and the normal fiber-bridging stress.

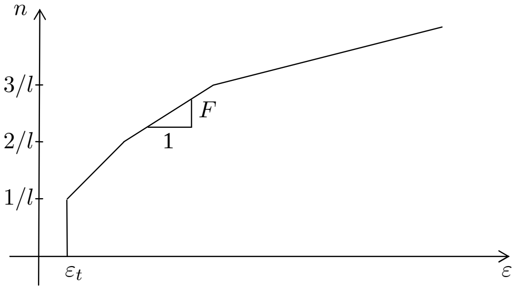

Figure 2: Crack evolution law: normal strain vs. number of cracks per length.

2.2 The constitutive equations

In the first part of the theory, the crack is treated as a unified whole. Later, the behavior of a crack is split into a fiber part and a matrix part, as shown in figure 1. In general, a crack is initiated as the stress reaches the yield surface, according to plasticity theory. In the current investigation, the cohesion chosen is sufficiently high for the first crack to be initiated under pure mode I conditions. Due to this, the first crack is perpendicular to the direction of the first principal stress and after initiation the crack direction remains fixed. Furthermore, it is assumed that the stress, $\boldsymbol{\sigma}$, is equal to the stress in the crack, $\boldsymbol{\sigma}_{cr}$, and the stress in the uncracked elastic part of the material, $\boldsymbol{\sigma}_e$. The strain, ε, however is split into two parts, one related to the uncracked elastic material, $\boldsymbol{\varepsilon}_e$, and one related to the additional deformations due to the opening of cracks, $\boldsymbol{\varepsilon}_{cr}$:

$$\boldsymbol{\varepsilon} = \boldsymbol{\varepsilon}_e + \boldsymbol{\varepsilon}_{cr} \tag{1}$$

Figure 3 shows the local coordinate system in a crack. The relationship between the global strain in a crack, $\boldsymbol{\varepsilon}_{cr}$, and the local strain in a crack, $\boldsymbol{e}_{cr}$, can be written as:

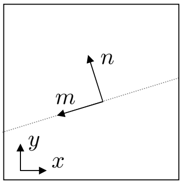

Figure 3: Local coordinate system in crack.

$$\boldsymbol{\varepsilon}_{cr} = \boldsymbol{T}\boldsymbol{e}_{cr} \tag{2}$$

$$\begin{bmatrix} \varepsilon_x^{cr} \\ \varepsilon_y^{cr} \\ \gamma_{xy}^{cr} \end{bmatrix} = \begin{bmatrix} n_x^2 & n_x m_x \\ n_y^2 & n_y m_y \\ 2n_x n_y & n_x m_y + n_y m_x \end{bmatrix} \begin{bmatrix} \varepsilon_{nn}^{cr} \\ \gamma_{nm}^{cr} \end{bmatrix} \tag{3}$$

taking only ε_{nn}^{cr} and γ_{nm}^{cr} into account, and $\boldsymbol{T}$ is the transformation matrix. A similar relationship can be found between the global stress, $\boldsymbol{\sigma}$, and the stress, $\boldsymbol{s}$, in the crack:

$$\boldsymbol{s} = \boldsymbol{T}^T\boldsymbol{\sigma} \tag{4}$$

The relationship between the local strain in the crack, $\boldsymbol{e}_{cr}$, the crack opening for a single crack, $\boldsymbol{\delta}$, the length of the RVE, l and the number of parallel cracks in the RVE, N can be written as:

$$\boldsymbol{e}_{cr} = N/l\boldsymbol{\delta} = n\boldsymbol{\delta} \tag{5}$$

Thus the total strain formulation (eq. (1)) can then be rewritten as:

$$\boldsymbol{\varepsilon} = \boldsymbol{\varepsilon}_e + \boldsymbol{T}n\boldsymbol{\delta} \tag{6}$$

In incremental form splitting the strain gives:

$$\boldsymbol{d\varepsilon} = \boldsymbol{d\varepsilon}_e + \boldsymbol{T} dn \boldsymbol{\delta} + \boldsymbol{T} n \boldsymbol{d\delta} \tag{7}$$

The relationship between the elastic strain increment, $\boldsymbol{d\varepsilon}_e$, and stress increment, $\boldsymbol{d\sigma}$, is:

$$\boldsymbol{d\sigma} = \boldsymbol{D}_e \boldsymbol{d\varepsilon}_e = \boldsymbol{D}_e(\boldsymbol{d\varepsilon} - \boldsymbol{T} dn \boldsymbol{\delta} - \boldsymbol{T} n \boldsymbol{d\delta}) \tag{8}$$

where $\boldsymbol{D}_e$ is the elastic stiffness matrix, which refers to the intact material between the cracks and is therefore constant throughout the entire analysis.

$$\boldsymbol{D}_e = [\boldsymbol{C}_e]^{-1} = \frac{E_0}{1-\nu^2} \begin{bmatrix} 1 & \nu & 0 \\ \nu & 1 & 0 \\ 0 & 0 & \frac{1-\nu}{2} \end{bmatrix} \tag{9}$$

The relationship between crack opening for a single crack, $\boldsymbol{\delta}$, and stress in the crack, $\boldsymbol{s}$, in incremental form can be written as:

$$\boldsymbol{d\delta} = \boldsymbol{C}_{cr} \boldsymbol{ds} = \boldsymbol{C}_{cr} \boldsymbol{T}^T \boldsymbol{d\sigma} \tag{10}$$

where the stress, $\boldsymbol{ds}$, is substituted using eq. (4) and $\boldsymbol{C}_{cr}$ is the tangent compliance matrix for a single crack. To solve the differential equation (eq. (8)), the crack evolution law needs to be introduced in incremental form:

$$dn = F(\varepsilon_{nn}) d\varepsilon_{nn} \tag{11}$$

where $d\varepsilon_{nn}$ is the normal component of total strain normal to the crack direction ($d\varepsilon_{nn} = [1\ 0]\boldsymbol{T}^T \boldsymbol{d\varepsilon}$) and F is the slope of the crack evolution law (see figure 2). Inserting eq. (10) and (11) in eq. (8) the differential equation can now be written as:

$$\boldsymbol{d\sigma} = \boldsymbol{D}_e(\boldsymbol{d\varepsilon} - \boldsymbol{T} F d\varepsilon_{nn} \boldsymbol{\delta} - \boldsymbol{T} n \boldsymbol{C}_{cr} \boldsymbol{T}^T \boldsymbol{d\sigma}) \tag{12}$$

To obtain a relationship between total strain increment, $\boldsymbol{d\varepsilon}$, and the stress increment, $\boldsymbol{d\sigma}$, eq. (12) is rearranged:

$$\begin{aligned} &(\boldsymbol{C}_e + \boldsymbol{T} n \boldsymbol{C}_{cr} \boldsymbol{T}^T)\boldsymbol{d\sigma} = (\boldsymbol{d\varepsilon} - \boldsymbol{T} F \boldsymbol{\delta} d\varepsilon_{nn}) \Leftrightarrow \\ &(\boldsymbol{C}_e + \boldsymbol{T} n \boldsymbol{C}_{cr} \boldsymbol{T}^T)\boldsymbol{d\sigma} = (\boldsymbol{I} - \boldsymbol{T} F \boldsymbol{\delta}[1\ 0]\boldsymbol{T}^T)\boldsymbol{d\varepsilon} \Leftrightarrow \\ &\boldsymbol{d\sigma} = (\boldsymbol{C_e} + \boldsymbol{T} n \boldsymbol{C_{cr}} \boldsymbol{T}^T)^{-1}(\boldsymbol{I} - \boldsymbol{T} F \boldsymbol{\delta'} \boldsymbol{T}^T)\boldsymbol{d\varepsilon} \end{aligned} \tag{13}$$

where $\boldsymbol{I}$ is a 3-by-3 unit matrix and $\boldsymbol{\delta}'$ is a 2-by-2 matrix containing the displacement components (see eq. (14)).

$$\boldsymbol{\delta'} = \begin{bmatrix} \delta_{nn} & 0 \\ \delta_{mn} & 0 \end{bmatrix} \tag{14}$$

The tangent stiffness matrix, $\boldsymbol{D_{ep}}$, is readily identified from eq. (13) and for multiple crack directions $\boldsymbol{T}$, $n\boldsymbol{C}_{cr}$, and $F\boldsymbol{\delta'}$ can be written as:

$$\boldsymbol{T} = [\ \boldsymbol{T}_1 \quad \boldsymbol{T}_2 \quad ... \quad \boldsymbol{T}_j\ ] \tag{15}$$

$$n\boldsymbol{C}^{cr} = \begin{bmatrix} n_1\boldsymbol{C}_1^{cr} & 0 & ... & 0 \\ 0 & n_2\boldsymbol{C}_2^{cr} & & 0 \\ : & & & : \\ 0 & 0 & ... & n_j\boldsymbol{C}_j^{cr} \end{bmatrix} \tag{16}$$

$$F\boldsymbol{\delta'} = \begin{bmatrix} F_1\boldsymbol{\delta'}_1 & 0 & ... & 0 \\ 0 & F_2\boldsymbol{\delta'}_2 & & 0 \\ : & & & : \\ 0 & 0 & ... & F_j\boldsymbol{\delta'}_j \end{bmatrix} \tag{17}$$

where j refers to the current crack direction.

The constitutive equations presented here are only valid up before localization occurs in a crack thanks to the assumption that all cracks associated with a material point have identical crack openings. For the model to be valid after localization takes place, an extension has to be made.

2.3 Matrix crack model

The matrix crack is modeled employing an elasto-plastic material model for damage initiation and propagation in plain concrete. The model employed is a modified version of the model originally developed by Carol et al. (1997). The model employs a modified Mohr-Coulomb yield surface, f allowing the crack to propagate under mixed-mode conditions. During the sliding of the crack, the model is able to capture the dilation in the normal direction. The dilation phenomenon is important when modeling crack propagation in cementitious materials. If a crack opening is confined in the normal direction during sliding, large normal-compression forces can build up on the crack surface. The model includes damage parameters and, as the material softens, the shape of the yield surface will gradually tend towards the Coulomb yield surface. The normal and shear crack openings are organized in the matrix $\boldsymbol{\delta}$, and the associated matrix stress components on the crack surface are organized in the matrix $\boldsymbol{s}_m$:

$$\boldsymbol{\delta} = \begin{bmatrix} \delta_{nn} \\ \delta_{mn} \end{bmatrix} \tag{18}$$

$$\boldsymbol{s}_m = \begin{bmatrix} s^m_{nn} \\ s^m_{mn} \end{bmatrix} \tag{19}$$

2.3.1 Yield surface

The modified Mohr-Coulomb yield surface, f_1, can be written as:

$$f_1 = (s^m_{mn})^2 - (c - s^m_{nn}\mu)^2 + (c - f_t\mu)^2 \tag{20}$$

where c is the cohesion, μ, is the friction coefficient and f_t is the tensile strength of the matrix. In compression, the yield surface is cut off and enclosed by a circular surface, f_2, as shown in figure 4. This helps to avoid too large stresses in compression and ensures that the dilation effect vanishes with large openings. The expression for the circular surface is given as:

$$f_2 = (s^m_{nn} - s_c)^2 + (s^m_{mn})^2 - r^2 \tag{21}$$

where s_c is the normal stress in the center of the yield surface and r is the radius of the yield surface. The normal stress at which the two surfaces intersect is denoted s'. The circular surface and the Coulomb surface have coinciding tangents at the intersection to create a smooth transition between the two surfaces (see figure 4). To ensure this, the center of the circle, s_c, and the radius, r, are functions of the material parameters, c, μ, f_t and s'. The normal stress at the center of the circular surface, s_c, the circle radius, r, and the uniaxial compression strength, f_c can be found as:

$$s_c = -\mu c + \mu^2 s' + s' \tag{22}$$

$$r = \sqrt{(s' - s_c)^2 + (c - s'\mu)^2 - (c - f_t\mu)^2} \tag{23}$$

$$f_c = s_c - r \tag{24}$$

assuming that the normal stress at the intersection, s', is known.

The material softens as the crack opens. The softening is described through the damage parameter, κ_1:

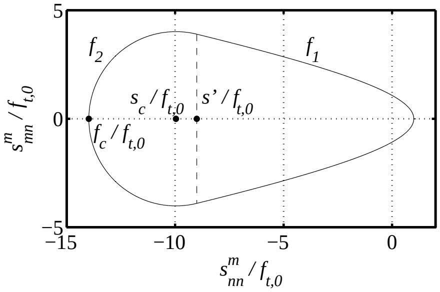

Figure 4: Modified Mohr-Coulomb yield surface. The transition between the Coulomb surface, f_1, and the circular surface, f_2, is marked by a dashed line.

$$\begin{aligned} c &= c_0(1-\kappa_1) && \kappa_1 < 1 \\ \mu &= \mu_0(1-\kappa_1) + \mu_f \\ f_t &= f_{t,0}(1-\kappa_1) \\ s' &= s'_0(1 - \frac{e^{-a}\kappa_1}{(1+(e^{-a}-1)\kappa_1)}) \end{aligned} \tag{25}$$

where a is a constitutive parameter. In the present model, the yield surface can only contract and the contraction will occur as the crack opens and slides. An extension to the model would be to allow the yield surface to reestablish partly as the crack closes, and thereby partly reestablish the friction and compression capacity.

2.3.2 Flow rule

The crack opening increment, $\boldsymbol{d\delta}$, is perpendicular to the plastic potential surface, g. A non-associated plastic flow rule is applied for the Coulomb surface and the circular surface:

$$g_1 = (s^m_{nm})^2 - (c - s^m_{nn}\mu_g)^2 + (c - f_t\mu_g)^2 \quad s_c > 1 \tag{26}$$

$$g_2 = (s^m_{nm})^2 + (c - s^m_{nn}\mu_g)^2 + (c - f_t\mu_g)^2 \quad s_c \leq 1 \tag{27}$$

where μ_g is a friction coefficient for the plastic potential and g_1 is employed for normal stresses larger than the normal stress at the center of the circular surface, s_c and g_2 for stresses smaller than s_c.

The flow rule can be written as:

$$\boldsymbol{d\delta} = d\lambda \frac{\boldsymbol{\partial g}}{\boldsymbol{\partial s}_m} \tag{28}$$

The normals for the two potentials are:

$$\frac{\boldsymbol{\partial g}_1}{\boldsymbol{\partial s}_m} = \begin{bmatrix} 2\mu_g(c - s^m_{nn}\mu_g) \\ 2s^m_{mn} \end{bmatrix} \tag{29}$$

$$\frac{\boldsymbol{\partial g}_2}{\boldsymbol{\partial s}_m} = \begin{bmatrix} -2\mu_g(c - s^m_{nn}\mu_g) \\ 2s^m_{mn} \end{bmatrix} \tag{30}$$

The sign change in the normal for the circular potential ensures that the crack closes when the stress point reaches the back of yield circular surface. The physical interpretation of this is that the dilation effect falls as the shear or normal opening of the crack increases. The friction coefficient for the plastic potential, μ_g, degrades as a function of the damage parameter, κ_2:

$$\mu_g = \mu_{g,0}(1 - \kappa_2) \quad \kappa_2 < 1 \tag{31}$$

2.3.3 Damage law

The increase in damage, $\boldsymbol{d\kappa}$, is related to the flow rule through the damage law:

$$\boldsymbol{d\kappa} = \begin{bmatrix} d\kappa_1 \\ d\kappa_2 \end{bmatrix} = d\lambda \boldsymbol{h} \tag{32}$$

where $\boldsymbol{h}$ is the damage function. The choice of damage function depends on the normal stress in the crack and the current yield surface. In tension work hardening, $\boldsymbol{h}_1$, is used:

$$\boldsymbol{h}_1 = \begin{bmatrix} \dfrac{\boldsymbol{s}_m \dfrac{\boldsymbol{\partial g_1}}{\boldsymbol{\partial s_m}}}{G_{F,I}} \\ \dfrac{\boldsymbol{s}_m \dfrac{\boldsymbol{\partial g_1}}{\boldsymbol{\partial s_m}}}{G_{F,II}} \end{bmatrix} \quad s^m_{nn} \geq 0 \tag{33}$$

If we insert eq. (33) and (28) in the damage law (eq. (32)), the increase in damage can be rewritten as:

$$\boldsymbol{d\kappa} = \begin{bmatrix} \dfrac{\boldsymbol{s}_m \boldsymbol{d\delta}}{G_{F,I}} \\ \dfrac{\boldsymbol{s}_m \boldsymbol{d\delta}}{G_{F,II}} \end{bmatrix} \tag{34}$$

The damage parameter, $\boldsymbol{\kappa}$, is thereby a normalized measure for the amount of fracture energy consumed. The applied hardening function in tension gives the following relationship between normal crack opening, δ_{nn}, and normal stress, s^m_{nn}, in a pure mode I crack opening.

$$s^m_{nn} = f_{t,0} e^{-\delta_{nn} f_{t,0}/G_{F,I}} \tag{35}$$

where $f_{t,0}$ is the initial tensile strength of the matrix and $G_{F,I}$ is the mode I fracture energy.

A modified version of work hardening, $\boldsymbol{h}_2$, is employed in compression, when the normal stress is greater than the normal stress at the center of the yield circular surface, s_c. Only shear stress greater than the friction stress ($\sigma\mu_f$) is assumed to give rise to work.

$$\boldsymbol{h}_2 = \begin{bmatrix} \dfrac{s^m_{mn} + \mu_f \sigma sign(s^m_{mn})}{G_{F,II}} \dfrac{\partial g}{\partial s^m_{mn}} \\ \dfrac{s^m_{mn} + \mu_f \sigma sign(s^m_{mn})}{G_{F,II}} \dfrac{\partial g}{\partial s^m_{mn}} \end{bmatrix} \quad s_c \leq s^m_{nn} < 0 \tag{36}$$

Another modified version of work hardening, $\boldsymbol{h}_3$, is employed during compression, when the normal stress is smaller than the normal stress in the center of the circle, s_c.

$$\boldsymbol{h}_3 = \begin{bmatrix} \dfrac{s^m_{mn}}{G_{F,II}} \dfrac{\partial g}{\partial s^m_{mn}} + \dfrac{s^m_{nn} d}{G_{F,I}} \dfrac{\partial g}{\partial s^m_{nn}} \\ \dfrac{s^m_{mn}}{G_{F,II}} \dfrac{\partial g}{\partial s^m_{mn}} + \dfrac{s^m_{nn} d}{G_{F,I}} \dfrac{\partial g}{\partial s^m_{nn}} \end{bmatrix} \quad s^m_{nn} < s_c \tag{37}$$

where d is a constitutive parameter determining how fast the softening will take place. In this damage function, h_3, the normal opening is related to the mode I fracture energy, $G_{F,I}$ and the shear opening to the mode II fracture energy, $G_{F,II}$.

2.3.4 Consistency condition

The consistency condition makes sure that the stress in the matrix remains on the yield surface during plastic loading. The condition can be derived by making a first-order Taylor expansion of the yield condition, f:

$$f + \frac{\boldsymbol{\partial f}^T}{\boldsymbol{\partial s}_m} \boldsymbol{ds}_m + \frac{\boldsymbol{\partial f}^T}{\boldsymbol{\partial \kappa}} \boldsymbol{d\kappa} = 0 \tag{38}$$

where $\boldsymbol{\kappa}$ is the damage parameter and the derivative of the yield function with respect to the damage parameter can be found in the Appendix. Because f is equal to zero in the plastic state, eq. (38) can be rewritten employing eq. (32).

$$\frac{\partial \boldsymbol{f}^T}{\partial \boldsymbol{s}_m} \boldsymbol{ds}_m + \frac{\partial \boldsymbol{f}^T}{\partial \boldsymbol{\kappa}} d\lambda \boldsymbol{h} = 0 \tag{39}$$

Introducing the hardening modulus, A, the consistency condition is written as:

$$\frac{\partial \boldsymbol{f}^T}{\partial \boldsymbol{s}_m} \boldsymbol{ds}_m - A d\lambda = 0 \tag{40}$$

The plastic multiplier, $d\lambda$, can be found from eq. (40):

$$d\lambda = \frac{\partial \boldsymbol{f}^T}{\partial \boldsymbol{s}_m} \boldsymbol{ds}_m A^{-1} = \frac{\partial \boldsymbol{f}^T}{\partial \boldsymbol{s}_m} A^{-1} \boldsymbol{T} \boldsymbol{d\sigma}_{global} \tag{41}$$

where $\boldsymbol{d\sigma}_{global}$ is the global stress increment.

2.3.5 The compliance matrix

The relationship between the stress increment, $\boldsymbol{ds}_m$, and the crack opening increment, $\boldsymbol{d\delta}$, can be found by inserting eq. (41) in eq. (28):

$$\begin{gathered} \boldsymbol{d\delta} = \frac{\partial \boldsymbol{g}}{\partial \boldsymbol{s}_m} d\lambda \Leftrightarrow \\ \boldsymbol{d\delta} = \frac{\partial \boldsymbol{g}}{\partial \boldsymbol{s}_m} \frac{\partial \boldsymbol{f}^T}{\partial \boldsymbol{s}_m} \boldsymbol{ds}_m A^{-1} \end{gathered} \tag{42}$$

The compliance matrix is then given in eq. (42):

$$\boldsymbol{C}_{cr}^{m} = \frac{\partial \boldsymbol{g}}{\partial \boldsymbol{s}_m} \frac{\partial \boldsymbol{f}^T}{\partial \boldsymbol{s}_m} A^{-1} \tag{43}$$

where the hardening modulus, A, is given in eq. (39) and 40:

$$A = -\frac{\partial \boldsymbol{f}^T}{\partial \boldsymbol{\kappa}} \boldsymbol{h} \tag{44}$$

2.4 Fiber-bridging model

The stiffness of the fibers in the direction normal to the crack surface, e_b, can be found using information about the global normal stiffness of the SHFRCC, E_{SH}, the initial E-modulus for plane stress, $E = E_0/(1-\nu^2)$, the number of parallel cracks per length, n, and the stiffness of the matrix crack for pure mode I opening, $e^m_{nn,I}$. If we consider only the stiffness in the direction normal to a crack, eq. (13) gives:

$$(1/E + nC^{cr}_{11})^{-1}(1 - F\delta_{nn}) = E_{SH} \tag{45}$$

By substituting the crack compliance, C^{cr}_{11}, with the sum of the mode I matrix and fiber stiffness, $C^{cr}_{11} = 1/(e_b + e^m_{nn,I})$, the mode I fiber stiffness, e_b, can be found:

$$e_b = \frac{nE_{SH}E + e^m_{nn,I}(E_{SH} - E + E\delta_{nn}F)}{E - E_{SH} - E\delta_{nn}F} \tag{46}$$

where the pure mode I stiffness of the matrix, $e^m_{nn,I}$, can be found as a function of the current normal opening of a single crack. Thanks to the present formulation, the global tangent stiffness computed agrees with the global tangent stiffness, E_{SH}, found from an idealization of an uniaxial tensile test, when the cracks open in pure mode I. If the cracks open in mixed mode, the actual normal stiffness for the matrix, e^m_{nn}, will be lower than the pure mode I stiffness, $e^m_{nn,I}$, due to the mixed-mode crack formulation. It is assumed that the fiber normal stiffness, e_b, is unaffected by mixed mode crack opening.

During the sliding of a crack the fibers are modeled as randomly oriented Timoshenko beams and the relationship between crack deformations and shear stresses can be found by solving a boundary value problem (Kabele 2002). Assuming that the bending effect of a short stubby beam can be neglected and its deformation is dominated by uniform shearing only, the relationship can be given as:

$$s^b_{nm} = k\frac{\delta_{nm}}{\delta_{nn}} \tag{47}$$

where k is a constant calibrated by test, and δ_{nn} and δ_{nm} are the mode I and II crack openings, respectively. The tangent matrix for the average fiber stiffness can then be written as:

$$D^b_{cr} = \begin{bmatrix} e_b & 0 \\ -\frac{k\delta_{nm}}{\delta^2_{nn}} & \frac{k}{\delta_{nn}} \end{bmatrix} \tag{48}$$

In the current version of the model, the stiffness of the fiber-bridging has to be calibrated through experiments. If the changes are made to the matrix mix or the fiber amount or type is changed, a calibration is needed. An analytical model of the relationship between crack-opening and fiber-bridging normal stress has been derived by (Lin, Kanda & Li 1999).

2.5 The total compliance crack matrix

Because the matrix and fiber-bridging in the crack work in parallel, the total stiffness of the crack can be written as:

$$D_{cr} = D_{cr}^b + D_{cr}^m \tag{49}$$

The superposition of stiffness in the crack remains a hypothesis until the model has been validated by experimental results.

2.6 Unloading and reloading

During unloading and reloading, three different elements need to be considered: matrix, fibers and composite level.

The yield surface governs the unloading and reloading of the matrix crack . As observed in experiments (Kesner & Billington 1998), the elastic E-modulus tends to degrade as a function of the largest crack opening obtained. A simple scheme taking this degrading of normal stiffness into consideration is employed during unloading and reloading of the matrix crack (figure 5 and eq. (50)).

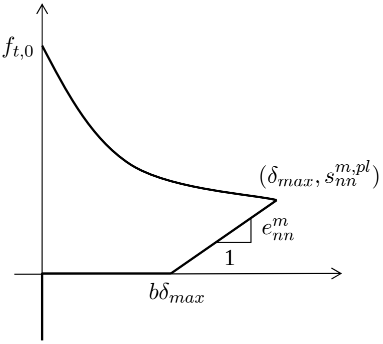

Figure 5: Unloading and reloading of the matrix crack.

$$e_{nn,un}^m = \begin{cases} s_{nn}^{m,pl}/((1-b)\delta_{max}) & \delta_{nn} > b\delta_{max} \\ 0 & b\delta_{max} > \delta_{nn} > 0 \\ \infty & \delta = 0 \end{cases} \tag{50}$$

where b is a constant calibrated by experiments, $s_{nn}^{m,pl}$ is the normal stress before unloading and δ_{max} is the maximal normal crack opening before unloading. The normal crack opening, δ_{nn}, cannot assume negative values, because this means that the crack surfaces would overlap. Giving the crack infinite normal stiffness causes the stiffness of the SHFRCC material in the crack-normal direction to be equal to the initial stiffness in compression. Eq. (50) is only valid when unloading occurs and while the normal stress is positive. If the normal stress is negative before unloading (this can occur during sliding), then the normal stiffness will be equal to infinity, because the matrix crack is then under compression. If the normal stress becomes positive, eq. (50) will again be valid. For the stress point to be able to move quickly from one side of the yield surface to the other ($(s^m_{nn},\ s^m_{nm}) \rightarrow (s^m_{nn},\ -s^m_{nm})$), when the tangential displacement increment changes direction, the elastic shear stiffness of the matrix crack is set to f_t / (1 $\mu m)$. The magnitude of the elastic shear stiffness influences the distribution of shear stresses between the matrix crack and fibers in the elastic state. An experimental investigation of this phenomenon can decide the real magnitude.

The crack opening governs the unloading and reloading of the fibers. The scheme applied to determine the relationship between the crack opening and the bridging stiffness normal to the crack surface resembles that applied for the matrix crack (figure 5). The fibers become elastic when the normal crack opening decreases:

$$e^b_{nn,un} = \begin{cases} s^{b,pl}_{nn}/((1-b)\delta_{max}) & \delta_{nn} > b\delta_{max} \\ 0 & b\delta_{max} > \delta_{nn} > 0 \end{cases} \tag{51}$$

When the crack has closed, the normal stress is transferred entirely through the matrix crack. It is assumed for simplicity that the fiber-bridging stress cannot become negative. The bridging stiffness normal to the crack surface is given by eq. (46), when the crack normal opening reaches the previous maximal opening, δ_{max}. It is assumed that the stiffness parallel with the crack surface can be found using eq. (47).

The total normal strain in the crack normal direction governs the unloading and reloading at the SHFRCC (composite) level. If the normal strain decreases, the number of cracks per length, n, remains constant. The SHFRCC becomes plastic and the number of cracks per length, n, can again increase when the normal strain in the crack normal direction exceeds the previous maximal strain in the crack normal direction.

2.7 Initiation of second crack direction

The first crack is initiated when the first principal stress reaches the tensile strength of the SHFRCC material, $f_{t,SH,0}$. The normal to the crack surface is parallel with the first principal stress, and the crack direction remains fixed after crack initiation. An angle threshold limits the angle between two crack systems, and the size of the angle threshold must be determined through experiments. A second crack system is initiated when the stress state in the matrix outside the angle threshold reaches the yield surface. The normal to the second crack system is parallel to the normal to the yield surface.

3.1 Introduction

The capability of the material model can be demonstrated by considering the opening of a single crack at a material point (see figure 6). The dimension of the RVE associated with the material point is 10 mm x 10 mm (l x l). The load is applied along the upper boundary in two steps. In step I a displacement, u_I, of 0.15 mm perpendicular to the crack plane is applied and in step II u_I is held constant, while a tangential displacement, u_{II}, of 0.1 mm is applied. Figure 7 shows the displacement load as a function of the time increment, t.

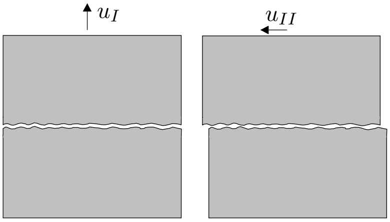

(a) Step I: Pure mode I crack opening.

(b) Step II: Mixed mode crack opening.

Figure 6: Opening of a single crack in a RVE.

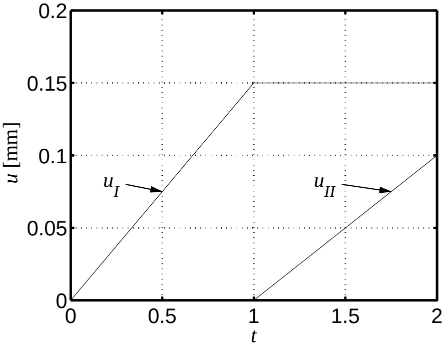

Figure 7: Displacement load, u, as a function of the time increment, t.

3.2 Model input

The material data applied for this simulation are: the tensile strength, $f_{t,SH,0}$ = 2.6 MPa, the initial E-modulus, E_0 = 33 GPa, the strain-hardening E-modulus, E_{SH} = 0.24 GPa and the ultimate strain before softening, ε_u = 0.007. Poisson's ratio, ν, is assumed to be 0.2. These material data are similar to those found by Østergaard, Walter & Olesen (2006) from the FPB experiments and an inverse analysis for the mix proportions given in table 1.

Table 1: Mix proportions of SHFRCC by weight (Østergaard et al. 2006).

Cement	Sand	Quarts	FA (milled)	FA	Water	SP	Fibers
1.00	0.40	0.40	0.36	0.84	0.54	0.014	0.045

The number of cracks per length, n, is assumed to be constantly equal to one. Finally the applied matrix properties related to the elasto-plastic matrix crack model are: the matrix tensile strength, $f_{t,0}$ = 2.0 MPa, the friction coefficient, c_0 = 6 MPa, the mode I fracture energy, $G_{F,I}$ = 30 N/m, the mode II fracture energy, $G_{F,II}$ = 30 N/m, the friction coefficients μ_f = 0.4, μ_0 = 0.2 and μ_g = 0.3 and the unloading constant b = 0.5.

3.3 Simulation results

The evolution in the matrix crack stress components is shown in figure 8. The current yield-surface is plotted for each stress point. In load-step I, the crack is initiated and opens in pure mode I. In this step, the matrix crack is only bridged by normal stress, and by the end of the step this is reduced to 39 % of the initial tensile strength, $f_{t,0}$. In step II, a mixed-mode opening is applied to the crack by adding pure sliding deformation at the upper RVE boundary, while keeping the normal deformation on this boundary constant. Because of the dilation effect, compression stress builds up in the matrix crack. After a certain amount of sliding, the dilation effect wears off and the stress in the matrix crack is reduced towards zero.

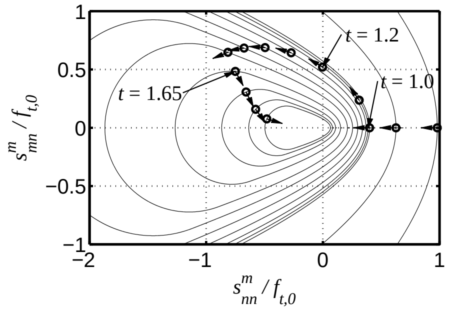

Figure 8: The matrix crack stress components are plotted together with the matching yield surface history. The arrows indicate the direction of the stress evolution.

In figure 9, the normal to the plastic potential, g, is plotted for a selected number of stress points. For each stress point the yield surface is plotted as well. Figure 10 shows the crack opening as a function of the step number. The relationship between the normal to the plastic potential and the increase in crack opening is described through the flow rule (eq. (28)). In step I, only mode I opening occurs in the crack and the normal to the plastic potential points straight forward. In step II, both normal and tangential opening occurs, where the normal opening is due to the dilation effect and the finite elastic stiffness of the continuum. As soon as the stress point reaches the back of the yield circular surface, the normal to the plastic potential begins to point backwards. As this happens, the dilation effect begins to wear off and the compression stresses decrease, causing the crack opening to decrease.

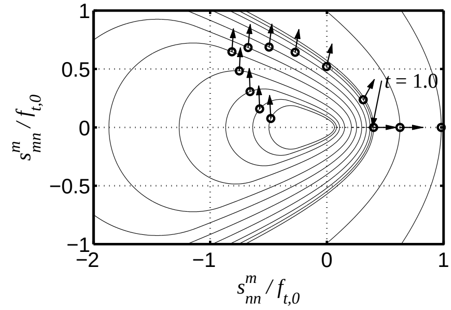

Figure 9: The normal to the plastic potential, g is plotted for a selected number of stress points. For each stress point the matching yield surface is plotted.

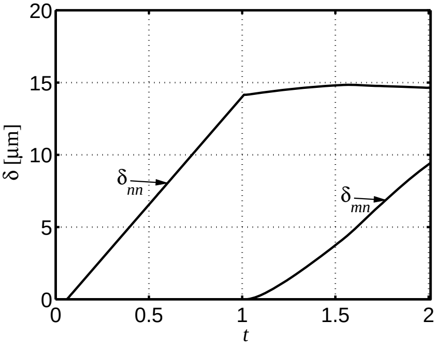

Figure 10: Crack opening as function of the time increment, t.

Figure 11 shows the stress history in the crack as a function of the time increment. In step I, the crack opens in pure mode I. At crack initiation there is a difference between the stress in the SHFRCC material, s, and the stress in the matrix crack, s_m, which is in good agreement with numerical observations (Dick-Nielsen et al. 2005), where a crack with an opening of only a few nanometers runs through the matrix before debonding of the fibers take place. Similar experimental observations have been made by (Wang & Li 2004). The SHFRCC mix 3 in these experiments had a first crack strength of 4 MPa, while experiments performed by Wang at the Technical University of Denmark, showed that the matrix in mix 3 had a tensile strength of 2.8 MPa. After crack initiation the matrix stress, s_m, decreases, the fiber-bridging, s_b, increases and the slope of the total strain-stress-relationship is E_{SH}. At the beginning of step II, the matrix crack stress decreases due to dilation. As the dilation effect wears off, the total stress, s, converges towards the fiber stress. This example demonstrates clearly the need to separate the matrix crack and the fiber descriptions. The fiber-bridging remains almost constant during sliding, while the matrix crack stress (and thereby the total stress) decreases significantly due to the dilation effect.

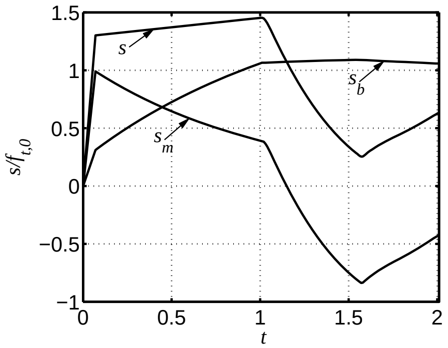

Figure 11: Normal stress history in the crack as a function of the time increment, t.

4 CONCLUSIONS

In the present article, a plasticity-based damage mechanics model for Strain-Hardening Fiber-Reinforced Cementitious Composite (SHFRCC) has been introduced. The present model differs from existing models by combining a matrix crack and a fiber model to describe the behavior of the SHFRCC material, and by giving detailed information on crack opening, orientation and spacing. The information provided by the model makes it possible to assess the state of an SHFRCC structure.

The behavior of a crack at a material point during mixed-mode opening has been simulated. This simulation demonstrated the need to separate the matrix crack and fiber-bridging behavior. During sliding, the change in fiber stresses was insignificant, but because of the dilation effect, the matrix crack stresses, and thereby the composite stresses, were significantly decreased.

In addition to information on global stresses and deformations, data about crack stress, opening, orientation and spacing was also obtained. Although the example is a simple one, it demonstrates the capability of the model. The simulation with the crack at the material point only contained a single crack. In part II, simulations of constructions containing multiple cracks will be carried out and compared with experimental data.

5 ACKNOWLEDGEMENTS

The authors would like to acknowledge the fruitful discussions we have had with Leif-Otto Nielsen, associate professor at the Department of Civil Engineering at the Technical University of Denmark.

The fourth author (PK) would like to acknowledge the financial support by the Ministry of Education, Youth and Sports of the Czech Republic Research Plan No. MSM6840770003.

Notation

The following symbols are used in this paper:

A	Hardening modulus
$\boldsymbol{C}_{cr}$	Tangent compliance matrix for a single crack
$\boldsymbol{D}_e$	Elastic stiffness matrix
$\boldsymbol{D_{ep}}$	Tangent stiffness matrix for the composite
E_0	E-modulus
E_{SH}	Strain-hardening modulus for the composite
F	Slope of the crack evolution law
$\boldsymbol{I}$	Unit matrix
N	Number of parallel cracks associated with a material point
$G_{F,I}$	Mode I fracture energy for the matrix
$G_{F,II}$	Mode II fracture energy for the matrix
G_f	Shear modulus for the fibers
$\boldsymbol{T}$	Transformation matrix
V_f	Fiber volume fraction
a	Constitutive parameter for the matrix
b	Unloading constant
c_0	Cohesion in the matrix
d	Constitutive parameter for the matrix
e	Stiffness of crack
$\boldsymbol{e}_{cr}$	Local strain in a crack
f_1	Mohr-Coulomb yield surface
f_2	Circular yield surface
f_c	Uniaxial compression strength of the matrix
$f_{t,0}$	Tensile strength of the matrix
$f_{t,SH,0}$	Tensile strength of the composite
g	Plastic potential
$\boldsymbol{h}$	Damage function
k	Shear stiffness constant for the fibers
l	Side length of RVE
n	Number of cracks per length
r	radius of the yield surface, f_2
$\boldsymbol{s}$	Local stress in a crack
s_c	Normal stress in the center of the yield surface, f_2
s'	Normal stress at which the two surfaces intersect
t	Time increment
u	Displacement
$\boldsymbol{\delta}$	Crack opening
$\boldsymbol{\varepsilon}$	Strain
$\boldsymbol{\varepsilon}_{cr}$	Strain related to the cracks
$\boldsymbol{\varepsilon}_e$	Strain in the uncracked elastic material
ε_t	Normal strain at first crack initiation
ε_u	Ultimate strain (before localization)
$\boldsymbol{\sigma}$	Stress

$\boldsymbol{\sigma}_{cr}$	Stress in the crack
$\boldsymbol{\sigma}_{e}$	Stress in the uncracked composite
ϕ	Threshold angle between two crack systems
$\boldsymbol{\kappa}$	Damage parameter
λ	plastic multiplier
μ_0	Friction coefficients for the yield surface
μ_f	Friction coefficients for the yield surface
$\mu_{g,0}$	Friction coefficients for the plastic potential
ν	Poisson’s ratio

References

Aveston, J., Cooper, G. A. & Kelly, A. (1971), *Single and multiple fracture - The Properties of Fibre Composites*, National Physical Laboratory (IPC Science and Technology Press Ltd), pp. 15–24.

Carol, I., Prat, P. C. & López, C. M. (1997), 'Normal/shear cracking model: Application to discrete crack analysis', *Journal of Engineering Mechanics* **123**(8), 765–773.

Dick-Nielsen, L., Stang, H. & Poulsen, P. N. (2005), Micro-mechanical analysis of fiber reinforced cementitious composites using cohesive crack modeling, *in* O. M. Jensen, M. Geiker & H. Stang, eds, 'Knud Hojgaard Conference on Advanced Cement-Based Materials', pp. 277–292.

Dick-Nielsen, L., Stang, H. & Poulsen, P. N. (2006*a*), Condition for strain-hardening in ECC uniaxial test specimen, *in* M. S. Konsta-Gdoutos, ed., 'Measuring, Monitoring and Modeling Concrete Properties', Springer, Alexandroupolis, Greece, pp. 41–47.

Dick-Nielsen, L., Stang, H. & Poulsen, P. N. (2006*b*), Simulation of strain-hardening in ECC uniaxial test specimen by use of a damage mechanics formulation, *in* H. M. G. Meschke, R D. Borst & N. Bicanic, eds, 'EURO-C 2006 Computational Modelling of Concrete Structures', pp. 319–328.

Dick-Nielsen, L., Stang, H. & Poulsen, P. N. (2007), 'Conditions for strain-hardening in ECC uniaxial test specimen', *Journal of Engineering Mechanics* p. submitted.

Han, T. S., Feenstra, P. H. & Billington, S. L. (2003), 'Simulation of highly ductile fiber-reinforced cement-based composite components under cyclic loading', *ACI Structural Journal* **100**(6), 749–757.

Jirasek, M. (2004), *Modeling of Localized Inelastic Deformation*.

Kabele, P. (2002), 'Equivalent continuum model of multiple cracking', *Engineering Mechanics (Association for Engineering Mechanics, Czech Republic)* **9 (1/2)**, 75–90.

Kanda, T. & Li, V. C. (1999), 'Effect of fiber strength and fiber-matrix interface on crack bridging in cement composites', *Journal of Engineering Mechanics* **125**(3), 290–299.

Kesner, K. E. & Billington, S. L. (1998), 'Investigation of ductile cement based composites for seismic strengthening and retrofit', *Concrete Research and Technology* pp. 19–33.

Leung, C. K. Y. (1996), 'Design criteria for pseudoductile fiber-reinforced composites', *Journal of Engineering Mechanics* **122**(1), 10–18.

Li, V. C. & Chan, Y. W. (1994), 'Determination of interfacial debond mode for fiber-reinforced cementitious composites', *Journal of Engineering Mechanics* **120**(4), 707–719.

Li, V. C. & Leung, C. K. Y. (1992), 'Steady state and multiple cracking of short random fiber composites', *ASCE Journal of Engineering Mechanics* **188**, 2246–2264.

Lin, Z., Kanda, T. & Li, V. C. (1999), 'On interface property characterization and performance of fiber-reinforced cementitious composites', *Concrete Science and Engineering* **1**, 173–184.

Naaman, A. E. (1987), High performance fiber reinforced cement composites, *in* 'Symposium on Concrete Structures for the Future, Paris, France', IABSE, pp. 371–376.

Olsen, C. & Billington, S. (2007), 'Energy absorbent infill panels for seismic retrofit of steel frame buildings utilizing high performance fiber-reinforced cementitous composites with self compacting capabilities - phase 1: Single panel component cyclic tests', *???* .

Østergaard, L. (2003), *Early-Age Fracture Mechanics and Cracking of Concrete*, DTU-Tryk.

Østergaard, L., Walter, R. & Olesen, J. F. (2006), Method for determination of tensile properties for ECC II: Inverse analysis and experimental results, *in* G. Fisher & V. C. Li, eds, 'International Rilem Workshop on High Performance Fiber-Reinforced Cementitious Composites (HPFRCC) in Structural Applications', RILEM Publications S.A.R.L., pp. 57–64.

Stang, H., Olesen, J. F., Poulsen, P. N. & Dick-Nielsen, L. (2007), 'On the application of cohesive crack modeling in cementitious materials', *Materials and Structures* **40**, 365–374.

Wang, S. & Li, V. C. (2004), 'Tailoring of pre-existing flaws in ECC matrix for saturated strain hardening', *Ia-FraMCos* .

Wu, H. C. & Li, V. C. (1995), 'Stochastic process of multiple cracking in discontinuous random fiber reinforced brittle matrix composites', *Int'l of J. of Damage MEchanics* **4**(1), 83–102.

6.1 The derivative of the Coulomb surface with respect to the damage parameter

Since the yield function is only a function of κ_1 the derivative of the Coulomb surface with respect to the damage parameter can be found with the expression below:

$$\frac{\boldsymbol{\partial f_1}}{\boldsymbol{\partial \kappa}} = \begin{bmatrix} \dfrac{\partial f_1}{\partial \kappa_I} \\ 0 \end{bmatrix} = \begin{bmatrix} \dfrac{\partial f_1}{\partial c}\dfrac{\partial c}{\partial \kappa_I} + \dfrac{\partial f_1}{\partial \mu}\dfrac{\partial \mu}{\partial \kappa_I} + \dfrac{\partial f_1}{\partial f_t}\dfrac{\partial f_t}{\partial \kappa_I} \\ 0 \end{bmatrix} \tag{52}$$

The derivatives for the yield function (eq. (20)) with respect to the material parameters can be written as:

$$\begin{bmatrix} \dfrac{\partial f_1}{\partial c} \\ \dfrac{\partial f_1}{\partial \mu} \\ \dfrac{\partial f_1}{\partial f_t} \end{bmatrix} = \begin{bmatrix} 2\mu(\sigma - f_t) \\ 2(c - \sigma\mu)\sigma - 2(c - f_t\mu)f_t \\ -2(c - f_t\mu)\mu \end{bmatrix} \tag{53}$$

The derivatives for the material parameters (eq. (25)) with respect to the damage parameter, κ_1, are given as:

$$\begin{bmatrix} \dfrac{\partial c}{\partial \kappa_I} \\ \dfrac{\partial \mu}{\partial \kappa_I} \\ \dfrac{\partial f_t}{\partial \kappa_I} \end{bmatrix} = \begin{bmatrix} -c_0 \\ -\mu_0 \\ -f_{t0} \end{bmatrix} \tag{54}$$

6.2 The derivative of the circular surface with respect to the damage parameter

Since the yield function is only a function of κ_1, the derivative of the function describing the circular surface with respect to the damage parameter can be found with the expression below:

$$\frac{\boldsymbol{\partial f_2}}{\boldsymbol{\partial \kappa}} = \begin{bmatrix} \dfrac{\partial f_2}{\partial \kappa_I} \\ 0 \end{bmatrix} = \begin{bmatrix} \dfrac{\partial f_2}{\partial s_c}\dfrac{\partial s_c}{\partial \kappa_I} + \dfrac{\partial f_2}{\partial r}\dfrac{\partial r}{\partial \kappa_I} \\ 0 \end{bmatrix} \tag{55}$$

Substituting the expression for the material parameters (eq. (25)) into the expression for the circle center, s_c, and the radius, r, leads to two very complicated expressions. So the expression for the derivative for these parameters with respect to the damage parameter, κ_1, has been split into two expressions that are more transparent:

$$\frac{\partial r}{\partial \kappa_I} = \frac{\partial r}{\partial c}\frac{\partial c}{\partial \kappa_I} + \frac{\partial r}{\partial f_t}\frac{\partial f_t}{\partial \kappa_I} + \frac{\partial r}{\partial \mu}\frac{\partial \mu}{\partial \kappa_I} + \frac{\partial r}{\partial s'}\frac{\partial s'}{\partial \kappa_I} \tag{56}$$

$$\frac{\partial s_c}{\partial \kappa_I} = \frac{\partial s_c}{\partial c}\frac{\partial c}{\partial \kappa_I} + \frac{\partial s_c}{\partial f_t}\frac{\partial f_t}{\partial \kappa_I} + \frac{\partial s_c}{\partial \mu}\frac{\partial \mu}{\partial \kappa_I} + \frac{\partial s_c}{\partial s'}\frac{\partial s'}{\partial \kappa_I} \tag{57}$$

where the derivatives of the circle radius, r, and center, s_c, can be found from eq. (23) and (22) with respect to the material parameters, c, f_t and μ and the derivative for the material parameters c, f_t, and μ are given in eq. (54). The derivative for the intersection normal stress between the two yield surfaces, s', can be written as:

$$\frac{\partial s'}{\partial \kappa_I} = -\frac{s'_0\, e^{-a}}{\left(1 + \kappa_I\, e^{-a} - \kappa_I\right)^2} \tag{58}$$

The derivatives of the function of the circular yield surface (eq. (21)) with respect to the circle center, s_c, and radius, r, are given as:

$$\begin{bmatrix} \dfrac{\partial f_2}{\partial s_c} \\ \dfrac{\partial f_2}{\partial r} \end{bmatrix} = \begin{bmatrix} -2s_{nn}^m + 2s_c \\ -2r \end{bmatrix} \tag{59}$$

Paper V

A Plastic Damage Mechanics Model for Strain-Hardening Fiber-Reinforced Cementitious Composite, Part II: Simulations

Submitted to: *Journal of Engineering Mechanics*

A Plastic Damage Mechanics Model

for Strain-Hardening Fiber-Reinforced Cementitious Composite

Part II: Simulations

L. Dick-Nielsen [1]

H. Stang [2]

P. N. Poulsen [3]

S. L. Billington [4]

Abstract: This article validates the material model for Strain-Hardening Fiber-Reinforced Cementitious Composites (SHFRCC) derived in the companion paper (Part I) to this article, by comparing simulation and experimental results. The simulations were carried out on a four-point bending (FPB) beam and on infill panels. In both cases, the simulation results were found to match the experimental results very well. The material model differs from existing models by providing detailed information about crack openings and spacing. For the infill panel, a parameter study showed that the model can help both limiting the cracked area and reduce the magnitude of the crack openings by employing relatively moderate changes to the matrix and fibers.

CE Database subject headings: Fracture Mechanics, Cracking, Finite element method, Concrete, Cements, Cohesion, Fiber reinforced materials, Strain hardening.

---

[1] Ph.D.-student, Department of Civil Engineering, Technical University of Denmark, building 118, 2800 Kgs. Lyngby, Denmark. E-mail: ldn@byg.dtu.dk

[2] Professor, Department of Civil Engineering, Technical University of Denmark, building 118, 2800 Kgs. Lyngby, Denmark. E-mail: hs@byg.dtu.dk

[3] Associate professor, Department of Civil Engineering, Technical University of Denmark, building 118, 2800 Kgs. Lyngby, Denmark. E-mail: hs@byg.dtu.dk

[4] Associate professor, Department of Civil & Environmental Engineering, Stanford University, Terman Engineering Center, Stanford, USA. E-mail: billington@stanford.edu

1 Introduction

Fiber-reinforced cementitious materials are often classified based on their predominant behavior under uniaxial tension. A distinction is then made between tension-softening and strain-hardening materials (Stang 1992), (Naaman & Reinhardt 1996), and the latter are often referred to as strain-hardening fiber-reinforced cementitious composites (SHFRCC). Strain-hardening is associated with the formation of multiple parallel cracks, while only a few cracks usually appear in tension-softening materials. The two kinds of material behavior have a large influence on the structural behavior of a structure, and SHFRCC-materials have often proved superior, see e.g. (Li 2003) and (Walter, Olesen, Stang & Vejrum 2007). Also the modeling approach is influenced by the material behavior under uniaxial tension. Tension-softening materials are often modeled employing a fracture-mechanical approach in which the behavior of a single crack is described, see e.g. (Hillerborg, Modeer & Petersson 1976), (Belytschko & Black 1999), (Asferg, Poulsen & Nielsen 2007) and (Dick-Nielsen, Poulsen, Stang & Olesen 2004). In contrast to this, the ductile behavior of SHFRCC materials often makes the use of continuum models more suitable, see e.g. (Kabele 2002) and (Han, Feenstra & Billington 2003).

A large number of continuum models for cementitious materials have been derived over the last 50 years. Two types of models often employed are damage mechanics models and smeared models. In the damage mechanics models, the elastic material parameters degrade as the damage parameters increase, see e.g. Kachanov (1958). In the smeared models, the strain is split into two parts: one related to the cracks and the other related to the elastic material between the cracks, see e.g. Rashid (1968) and Bazant & Oh (1983). The smeared models were originally intended for tension-softening materials, but the concept can be extended to strain-hardening materials as well.

Very few continuum models have so far been derived to capture the special behavior of SHFRCC materials, see e.g. (Han et al. 2003) and (Kabele 2002). Both of these models are based on the smeared-crack approach; the first is a total-strain, rotating smeared-crack model and the latter is a smeared fixed-crack model. The models give no detailed information about the crack pattern and do not capture the dilation effect of the matrix during the sliding of a crack. Stang, Olesen, Poulsen & Dick-Nielsen (2007) found that cracks in the SHFRCC matrix reach significant lengths before the matrix becomes stress-free. A realistic description of the SHFRCC material during the propagation of the matrix cracks should therefore include both the matrix and the fiber behavior as shown in (Dick-Nielsen, Stang & Poulsen 2005) and (Dick-Nielsen, Stang & Poulsen 2006).

In Part I of this article, a plasticity-based damage mechanics model for SHFRCC based on the smeared fixed, multiple-cracking approach was presented. The behavior of the SHFRCC-material in the present model is based on the concept of a Representative Volume Element (RVE), where the RVE is thought of as an element containing a sufficient number of microstructural inhomogeneities for it to be considered macroscopically homogeneous. This model differs from existing SHFRCC models by combining a matrix crack model and a fiber model, and it is capable of giving detailed information about crack openings and spacing. In figure 1, the normal stress in the composite, the normal stress in the matrix crack, and the normal fiber-bridging stress are plotted as a function of the normal strain. The magnitude of the crack openings in PVA-SHFRCC is of the order of 50-200 μm before localization occurs (Li 2003) and (Fischer, Stang & Dick-Nielsen 2007) and 50-130 μm for SHFRCC reinforced with high strength steel fibers (Liao, Chao, Park & Naaman 2006). For larger crack openings the cracks will mainly be bridged by the fibers, but for openings of this magnitude the cracks will be bridged by cohesive matrix stresses as well. The matrix part especially influences the crack behavior during the sliding of the crack, where dilation effects will appear.

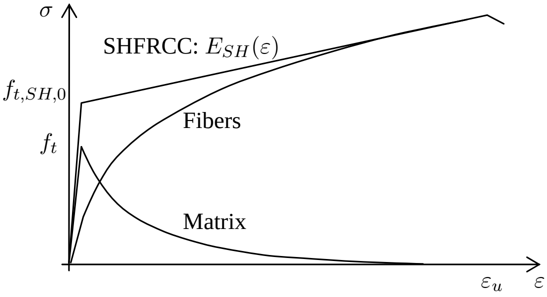

Figure 1: The normal stress in the composite, the normal stress in the matrix crack and the normal fiber-bridging stress plotted as a function of the normal strain.

The first crack is initiated as the first principal stress reaches the tensile strength of the composite, $f_{t,SH,0}$. At initiation, the normal for the crack surface is perpendicular to the first principal stress, and after crack initiation, the crack orientation remains fixed. As input, information about the number of cracks per length in the RVE, n as a function of the normal strain, is needed (see figure 2). This relationship constitutes a crack evolution law, that must be determined experimentally. The crack evolution law is assumed to be continuous to avoid numerical problems during computations. The chosen length of the RVE, l, should be sufficiently large to represent the behavior of the material. All cracks associated with one material point are assumed to have identical crack openings, $\boldsymbol{\delta}$.

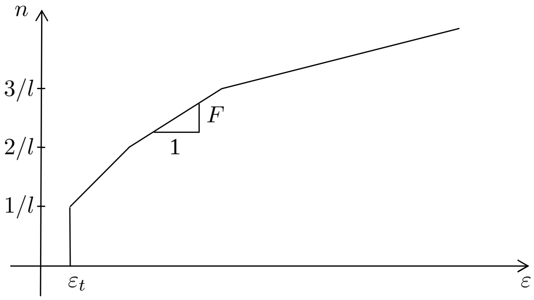

Figure 2: Crack evolution law: strain vs. crack number per length, n.

The matrix cracks are modeled using an elasto-plastic material model for damage initiation and propagation; this is a modified version of the model by Carol, Prat & López (1997) originally intended for unreinforced concrete. The model employs a closed Mohr-Coulomb yield surface and is able to capture the dilation effect during crack sliding. The model includes damage parameters and as the damage increases, the shape of the yield surface will gradually tend towards a point after which the matrix crack becomes traction-free.

The mode I fiber-bridging stiffness, e_b, was found through an inverse analysis based on information on of the global stiffness, E_{SH}, for a given normal strain (see figure 1), the initial E-modulus for plane stress, $E = E_0/(1-\nu^2)$, the number of parallel cracks per length, n, and the pure mode I stiffness for a given crack opening, $e^m_{nn,I}$. The shear stiffness of the fibers was modeled as randomly orientated elastic Timoshenko beams (Kabele 2002).

The constitutive equations for the model can be found in the companion paper (Part I) to this article. In the present part, the capability of the model will be demonstrated by comparing simulation results with corresponding results from experiments.

2 Four Point Bending Beam Simulation

2.1 Introduction

The model was implemented in a user supplied routine in the commercial FEM package 'DIANA'. A simulation of a four-point bending (FPB) beam was carried out as a test of the present model (see figure 3). Corresponding experimental results were found by Østergaard, Walter & Olesen (2006). In contrast to the simulation of the crack opening at the material point (in Part I), multiple cracking occurred in the beam. For the simulation, only half the beam was modeled due to symmetry, and here a 70-by-17 element mesh was employed. The elements employed were 8-node, quadrilateral isoparametric plane stress elements. The elements were based on quadratic interpolation and Gauss integration. The dimensions of the beam were: length 500 mm, height 60 mm and width 100 mm. The beam was simply supported and loaded as shown in the figure. Points A and B were used for measuring of vertical displacement, u, and point C was used to evaluate the state of the material.

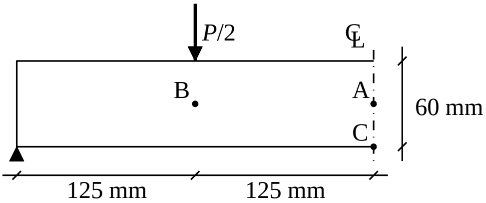

Figure 3: Four-point bending beam. Due to symmetry, only half the beam is modeled. Points A and B are used to measure a relative deflection, while point C is used to evaluate the state of the material.

Table 1: Mix proportions of SHFRCC by weight (Østergaard et al. 2006).

Cement	Sand	Quarts	Fly Ash (milled)	Fly Ash	Water	SP	Fibers
1.00	0.40	0.40	0.36	0.84	0.54	0.014	0.045

2.2 Model input

The material data was found from the FPB experiments and an inverse analysis (Østergaard et al. 2006) (the mix proportions are given in table 1): the tensile strength, $f_{t,SH,0}$ = 2.6 MPa, the initial E-modulus, E_0 = 33 GPa, the strain-hardening E-modulus, E_{SH} = 0.24 GPa and the ultimate strain before softening, ε_u = 0.007. Poisson's ratio, ν, was assumed to be 0.2.

To obtain information about crack opening and spacing from the simulation, information about the number of cracks per length, n, as a function of the total normal strain in the crack normal direction, ε_{nn}, is required (see figure 2). These data were not measured in the experiments, so some reasonable values were assumed. These additional input data only had little influence on global results like global stresses and the deflection of the beam, because the cracks mainly opened in mode I. The relationship between the number of cracks per length, n, and strain, ε_{nn}, was chosen as: (ε_{nn}; n [mm^{-1}]), (7.9$\cdot 10^{-5}$; 0.02), (1$\cdot 10^{-4}$; 0.04), (1$\cdot 10^{-3}$; 0.06), (3$\cdot 10^{-3}$; 0.08) and (6$\cdot 10^{-3}$; 0.1). Finally, the matrix properties related to the elasto-plastic matrix model were chosen as: the matrix tensile strength, $f_{t,0}$ = 2.0 MPa, the friction coefficient, c_0 = 6 MPa, the mode I fracture energy, $G_{F,I}$ = 30 N/m, the mode II fracture energy, $G_{F,II}$ = 30 N/m, the friction coefficients μ_f = 0.4, μ_0 = 0.2 and μ_g = 0.3, and the unloading constant b = 0.5.

2.3 Simulation results

Figure 4 plots the relative load-deflection curve from the simulation together with the upper and lower bounds from the experiments. In contrast to the experiments, a partial unloading was performed in the simulation to demonstrate the chosen unloading and reloading scheme. The load was applied in three steps: first the load was increased until a deflection of approximately 0.7 mm was reached at load point I, then a partial unloading was performed until load point II was reached, and finally the load was increased in the remaining part of the simulation. As shown in the figure, the model was able to reproduce the experimental results very well. The simulation was stopped as soon as the ultimate strain, ε_u, was reached, which corresponds to when localization of a crack would occur.

Figure 5 shows the relationship between the normal stress, s, at point C and the relative deflection. The total stress, s, reached a peak at a relative deflection of approximately 1.1 mm. After the peak point was reached, the SHFRCC material began to soften and the simulation was stopped. The unloading scheme worked as intended, leaving a permanent plastic deformation after unloading. At a deflection of 1 mm, the matrix had become stress-free and the crack was therefore only bridged by the fibers.

Figure 6 shows the crack pattern at a deflection of approximately 0.9 mm, before localiza-

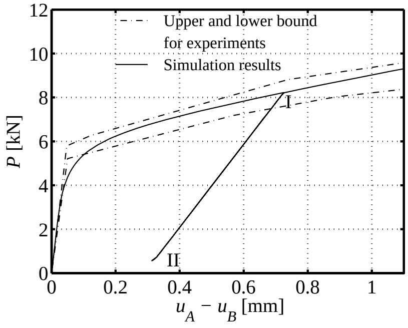

Figure 4: Relative load-deflection curve. Points A and B at which the deflection, u, was measured can be found in figure 3. Load points I and II indicate the beginning of the unload and reload branches respectively.

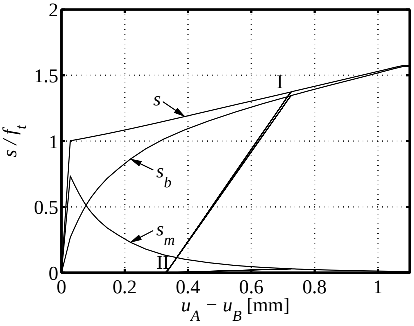

Figure 5: Total stress, s, fiber-bridging stress, s_b, and matrix normal stress, s_m, at point C vs. deflection.

tion takes place at the bottom of the beam. The thickness of the line corresponds to the crack opening. Cracks along the entire bottom in the middle section are about to localize, due to the constant moment in this section.

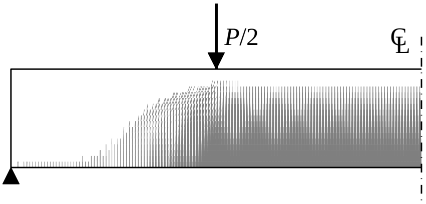

Figure 6: Crack pattern in the beam at a deflection of 0.9 mm. The line thickness corresponds to the crack opening.

Figure 7 shows the relationship between the relative deflection and the average normal crack opening, δ_{nn}, associated with point C. During unloading from load point I to II, the average crack opening associated with point C decreased linearly towards zero. At a relative deflection of 1.1 mm, the average crack opening associated with point C was 70 μm, which is a typical magnitude for SHFRCC specimen before localization takes place (Fischer et al. 2007).

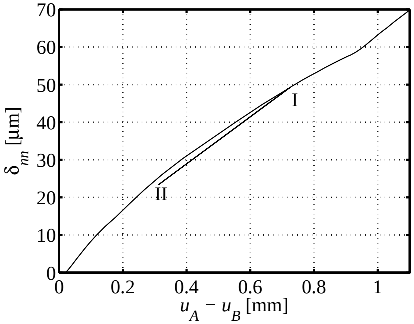

Figure 7: Average crack opening associated with point C vs. deflection.

The average crack spacing associated with point C was plotted as a function of the relative deflection in figure 8. After the first crack was initiated, the average crack-spacing was 50 mm. The spacing decreased until load point I was reached. During unloading from load point I to II, the deflection decreased, while the crack spacing remained constant as intended. After reloading to load point II, the crack spacing decreased until a spacing of 10 mm was reached, after which the spacing remained constant.

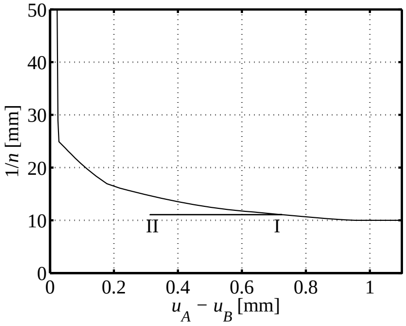

Figure 8: Average crack spacing associated with point C vs. deflection.

3 Infill Panels

3.1 Introduction

In the United States, steel moment-frames are a common structural system. However, brittle failure has been detected in beam-column welded connections during earthquakes (SB 1994). To avoid these brittle failures, it has been suggested by Kesner & Billington (2005) and Olsen & Billington (2007) that steel moment frames can be retrofitted by inserting ductile, precast concrete infill panels to increase the stiffness and energy dissipation of the frame during seismic loading (see figure 9). The infill panels are bolted into the steel frames with pretensioned bolt connections, which makes the system rapidly replaceable if damaged. The infill panels are made of SHFRCC; one proposed mix is shown in table 2 (Olsen & Billington 2007). The fibers are made of steel, have a length of 30 mm, a diameter of 0.38 mm, an minimum strength of 2300 MPa, and they have a twist at the end to improve pull-out behavior.

Table 2: Mix proportions of SHFRCC by weight (Olsen & Billington 2007).

Cement	Water	Sand	Fly Ash	Stones 13 mm	SP	Viscous Agent	High Strength Steel Fibers
1	0.6	1.7	0.5	1	0.003	0.0095	0.244

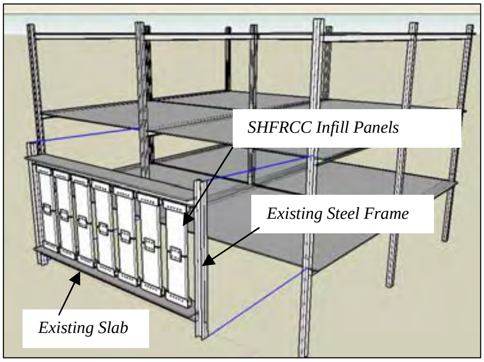

Figure 9: Retrofit schematic (Olsen & Billington 2007).

Experiments have been performed on single panels (Olsen & Billington 2007) with a test setup as shown in figure 10(a), in which the dimensions of the panel were 914 x 457 x 70 mm (36 x 18 x 2.75 inches). In the single panel tests, the panel was connected to a steel U-shaped channel, which was half of a HSS14x4x1/2 (h_1xh_2xt in inches) tube section with 25.4 mm-diameter pretensioned bolts. The U-profile was bolted to a steel beam (representing a floor beam) through a concrete slab. The U-profile was then filled with grout below and along the sides of the panel to facilitate a slip-critical connection with the pretensioned bolts. The panel contained a No. 3 reinforcing bar along the perimeter of the panel (diameter of 9.5mm) as well as welded wire fabric with a wire grid of 76 mm (3 inches) and a diameter of 3.3 mm as shown in figure 10(b). In the experiments the panel was loaded through a loading arrangement at the top of the panel, which dictated a horizontal displacement, u. The displacement was increased 8 times, starting with a displacement, u_{cycle}, of 0.92 mm and ending with a 27.4 mm displacement. The first three load steps (up to a displacement of 3.4 mm) consisted of three load cycles, while the last steps consisted of two cycles. In each step the load was reversed from positive to negative, $\pm u_{cycle}$.

A number of uniaxial tensile tests have also been carried out (Olsen & Billington 2007). The specimens in these tests were dog-bone shaped, where the narrow section was 203 mm long with a 51 x 25 mm cross section and the deformation was measured over a length of 175 mm.

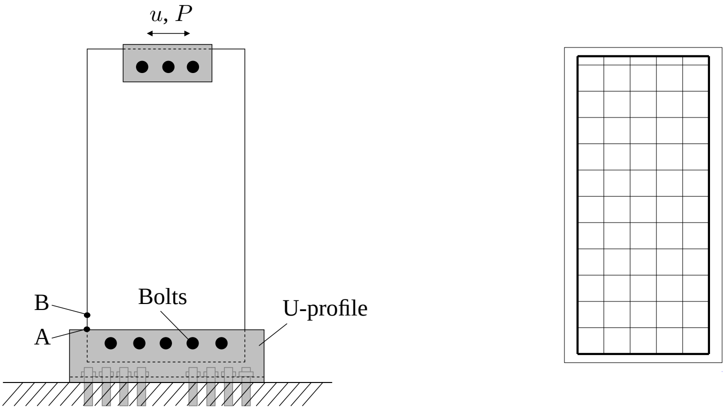

(a) Test setup for infill panel experiments. A and B were points from which the state of the material was analyzed. Point B is located 50 mm above point A.

(b) Reinforcement arrangement.

Figure 10: Infill panel: test-setup and reinforcement arrangement

Figure 11 shows the results from the uniaxial tensile tests. The same SHFRCC mix was used for all the tensile specimens and the large scatter is attributed to a variation in the distribution of fibers. The curve emphasized with the thick line was used as a reference curve in simulations of the panel behavior. This curve was chosen, because it is located in the lower part of the results. Since the dog-bone specimen was 25 mm thick and the length of the fibers was 30 mm, the fibers were mostly distributed in two dimensions. The panel being simulated was 70 mm thick, which results in a fiber distribution close to three dimensions. Three-dimensional fiber distribution results in a lower bridging stress than two-dimensional fiber distribution, as has been shown for example by Lin, Kanda & Li (1999). For this reason the lowerbound of tensile response was selected from the data in figure 11 to represent the tensile response of the SHFRCC in the panel simulations.

Figure 12 illustrates how the crack evolution law can be found from the uniaxial tensile curve. The crack evolution law gives the relationship between the normal strain, ε_{nn}, and the number of cracks per length, n. In this case the length, l, is the length over which the elongation was measured in the dog-bone specimen (175 mm). It is assumed that a crack is formed each time the stress in the tensile test drops by more than 1.5 percent. This assumed crack formation is indicated with vertical dashed lines in figure 12.

The material model presented in Part I is intended as a tool for the design engineer in the design phase. Once the material parameters are known/obtained from uniaxial experiments, information about the behavior of a structure and information about crack opening, orientation and spacing can also be obtained. It is also possible to investigate the effects of material modifications on the global (structural) response as well as on the local (material) response such as the cracking pattern. In the next section, a simulation of the infill panel with the reference

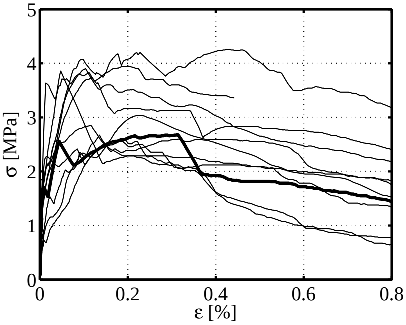

Figure 11: Uniaxial tensile stress-strain response of (Olsen & Billington 2007).

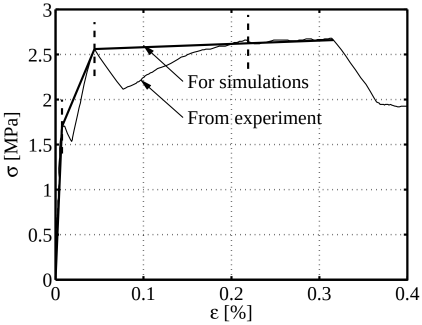

Figure 12: Uniaxial reference curve from the experiment and the corresponding smooth curve used in the simulation.

material parameters will be described along with a parameter study of the influence of matrix and fiber properties on simulated response. Since the yield surface cannot be reestablished once it has softened, it is not recommended to let the material undergo compression once the cracks are initiated. Therefore the simulations stop, when the cracks close.

3.2 FEM model

The FEM model employed is shown in figure 13. The elements in gray are the part of the panel that is fixed in the U-profile. The elements employed were 8-node, quadrilateral isoparametric plane stress elements, based on quadratic interpolation and Gauss integration. The reinforcement was modeled using embedded reinforcement elements positioned as shown in figure 10(b). Modeling the reinforcement as embedded implies that the reinforcement has perfect bond to the SHFRCC material. The simulations were performed using the commercial finite-element package, DIANA.

The bolts and the bottom of the U-profile act as springs along the lower support when loaded in tension. So four springs were employed to transfer the tensile stresses and a fixed support

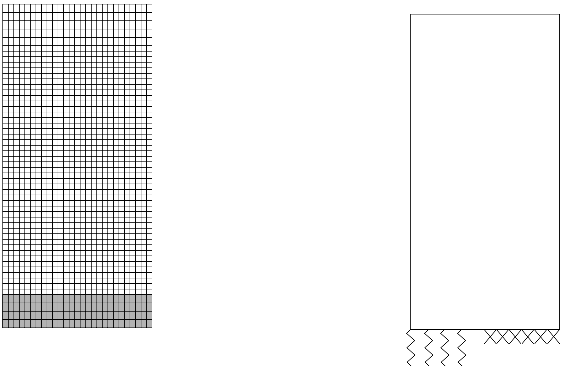

(a) Mesh applied for the FEM model.

(b) Supports applied for the FEM-model.

Figure 13: The mesh and supports applied for the FEM model of the infill panel.

was employed to transfer the compression stresses as shown in figure 13(b). The four springs were positioned with a spacing, b, of 51 mm (2 inches), which coincides with the distance from bolt center to bolt center. The bottom of the U-profile was modeled as a series of plates as shown in figure 14, where u and P_b are matching values of the midspan deflection and load transferred through a bolt. The vertical spring stiffness in the simulation, k, was then estimated (k = P_b / u) disregarding the bolt holes and the bolts:

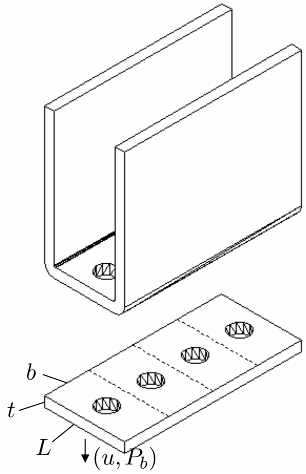

Figure 14: A section of the U-profile and an interpretation of how the bottom of the U-profile can be modeled as a series of parallel beams with the length, L width b and thickness t.

$$k = 192EI/L^3 = 16Ebt^3/L^3 = 300MN/m \tag{1}$$

where t is the thickness of the profile, L, the length of the beam and E is Young's modulus for steel. Due to the bolt holes, which reduce the cross-section and the axial stiffness of the bolts, the spring stiffness was set at 200 MN/m.

3.3 Material data

The tensile curve employed for the SHFRCC material is shown in figure 12, where the curve is simplified as a multi-linear strain-stress relationship. The tensile strength, $f_{t,SH,0}$, is 1.7 MPa, Young's modulus, E, is 23 GPa, the ultimate stress, σ_u, is 2.66 MPa, and Poission's ratio ν is set to 0.15. The relationship between normal strain, ε_{nn}, and the number of cracks per length, n, is shown in figure 15(b). The unloading parameter, b, is assumed to be 0.5.

The material data for the matrix were not measured in the experiments. To perform the simulations the reference material data for the matrix were assumed as follows: the tensile strength, $f_{t,0}$, is 1.6 MPa, the cohesion, c_0, is 5 MPa, the mode I and II fracture energy, $G_{F,I}$ and $G_{F,II}$, are 50 N/m, the friction coefficients, μ_f, μ_0 and μ_g, are 0.2, 0.4 and 0.3, the initial normal stress at the intersection between the Coulomb and the circular yield surface, s_c, is -20 MPa and the constant related to the rate at which the yield circle subtract, a, is -1.

A parameter study investigating the influence of fiber distribution, fiber amount and matrix properties was performed. In the parameter study three variations were made in relation to the reference material parameters. The strain-hardening and evolution curves employed are shown in figure 15. The material model is only valid up to the point where localization occurs, so only the part of the strain-hardening curves up to localization is shown. Figure 16 shows the relationships between the mode I crack opening and the normal bridging stress.

In variation 1, the reference fiber-bridging curve and matrix properties were kept unchanged (see figure 16), while the crack evolution law was modified. The modification gave rise to a larger number of cracks for a given normal strain. The change of crack evolution law could represent better fiber distribution. The larger number of cracks results in a larger normal strain at localization. The stress level of the strain-hardening curve remains unchanged compared with the reference parameters, because only the number of cracks is changed.

In variation 2 the tensile strength, $f_{t,SH,0}$, was increased from 1.7 MPa to 2.0 MPa and the ultimate stress, σ_u, was increased from 2.66 MPa to 5.32 MPa, while the crack evolution law and the matrix properties were kept constant compared with the reference material. These changes could represent an increased amount of fibers

In variation 3, the tensile strength, $f_{t,SH,0}$, and the matrix tensile strength, $f_{t,0}$, and fracture energy were all increased compared with the reference parameters, while the crack evolution law was kept unchanged. The fiber-bridging curve in variation 3 was very close to that used in variation 2 (see figure 16). The fracture energy of the matrix, G_F, was increased from 50 N/m to 75 N/m, the tensile strength, $f_{t,0}$, from 1.6 MPa to 3.2 MPa, and the resulting tensile strength from 1.7 MPa to 3.5 MPa.

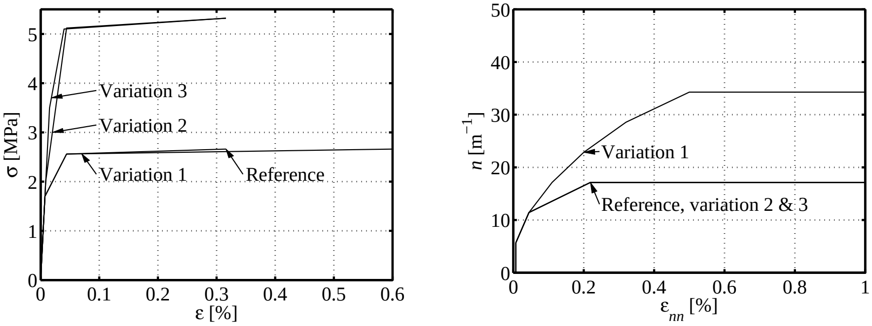

(a) Strain-hardening curves.

(b) Crack evolution laws: number of cracks per length, n as a function of the normal strain, ϵ_{nn}.

Figure 15: Material curves for the parameter study.

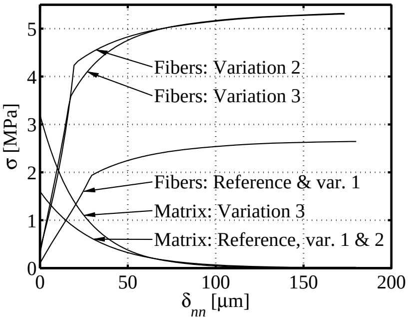

Figure 16: Stress separation curves for matrix and fiber-bridging curves.

3.4 Results and discussions

Figure 17 illustrates the crack pattern observed in the experiment during the different load stages, while the results from the simulation with the reference material are shown in figure 18 and 19. The simulation only covered a drift of 0.1 %, and at this drift, no visible cracks were observed in the experiment. As shown in figure 18(b) and 18(c), most crack openings in the simulation are less than 50 μm and therefore not visible for the naked eye. Furthermore the crack pattern observed in the simulation matches that found in the experiment in the final load step, where the localization occurs at the bottom left-hand corner. Also the load-displacement predicted by the simulation is very similar to that found in the experiment as shown in figure 18(a).

In figure 23(a) the normal stress is plotted as a function of the average crack opening associated with points A and B. The average crack opening at points A and B is 185 μm and 61 μm respectively at a horizontal displacement, u, of 0.92 mm. Figure 19(b) shows the average crack spacing associated with points A and B respectively for the simulation with the reference

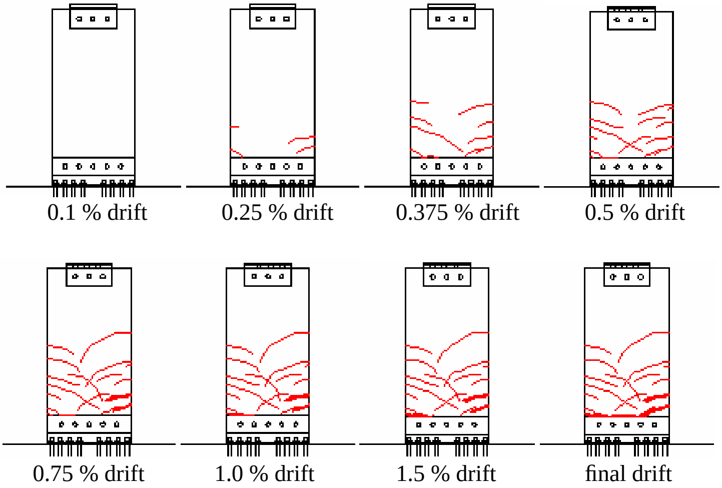
0.1 % drift 0.25 % drift 0.375 % drift 0.5 % drift

0.75 % drift 1.0 % drift 1.5 % drift final drift

Figure 17: Observed cracks in the experiment (Olsen & Billington 2007).

material. The crack evolution law shown in figure 15(b) for the reference material was derived using the data from the uniaxial tensile test for the dog-bone specimen (figure 12), where the elongation was measured over a length of 175 mm. At the instance when the tensile strength is reached in the panel, it is assumed that the average crack spacing is 175 mm. The crack spacing then decreases continuously as the normal strain (in a material point) increases, until a normal strain of 0.22 % is reached (see figure 12). When increasing the normal strain beyond 0.22 % the number of cracks associated with one material point remains constant. The simulation predicts that the number of cracks in the panel remains constant after a displacement, u, of 0.59 mm. At this displacement, the average crack spacing is 58 mm. In the experiments a crack spacing of approximately 30-50 mm was measured at the final drift. At point B in the

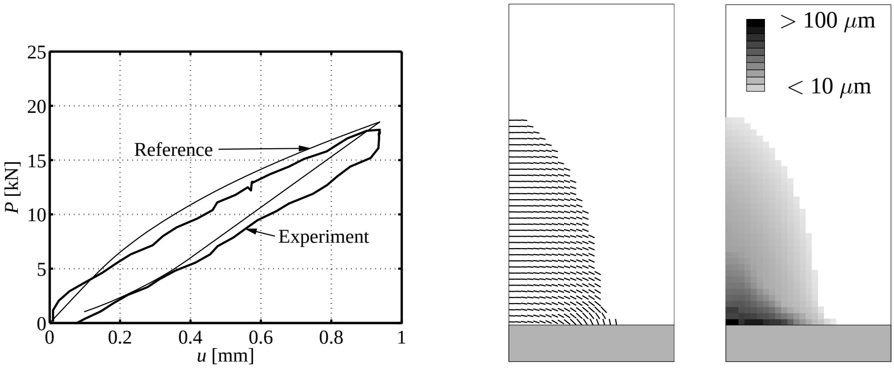

(a) Experimental and predicted loop. (b) Crack orientation. (c) Crack opening.

Figure 18: Results from the simulation of the reference infill panel.

simulation, the maximal number of cracks has not yet been reached at a displacement of 0.92 mm. The average crack distance at this point is 77 mm.

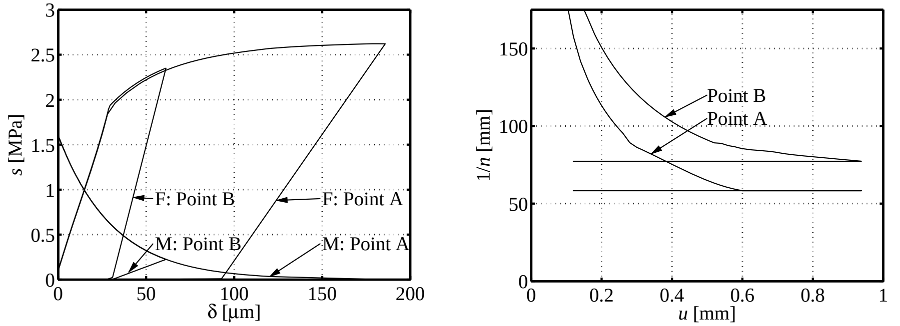

(a) Normal stresses as a function of the crack opening associated with point A and B in the matrix (M) and the fiber-bridging stresses (F).

(b) Average crack spacing associated with point A and B.

Figure 19: Results at point A and B from the simulation of the reference infill panel.

For the parameter study three extra simulations were performed, with the material variations presented in section 3.3. The load-deformation curves from the four simulations are shown in figure 20. The load-deformation curves from the reference material parameters and for material variation 1 are almost identical due to the very similar strain-hardening curves. Since the stress level is increased in the strain-hardening curves in variation 2 and 3 the load, P, is increased as well.

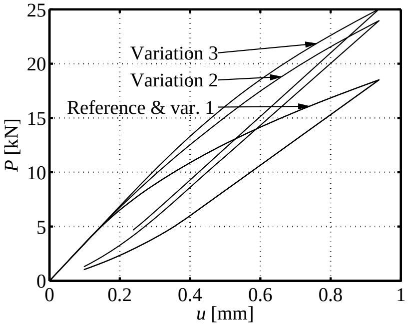

Figure 20: Comparison of one loop for the simulations.

Figure 21 shows the crack pattern for the four simulations, and figure 22 shows contour plots of the crack openings at a deformation, u, of 0.92 mm. Each element in the FEM models contains four integration points at which information about average crack opening, orientation and spacing was calculated. In the figures, only the crack with the largest opening in each element is plotted.

The crack pattern found in the simulation with material variation 1 resembles the pattern found with the reference material parameters. The size of the damaged area and the orientation of the cracks resemble the reference pattern, due to a similar stress level of the strain-hardening curve and a matching tensile strength, $f_{t,SH,0}$. The crack openings found for material variation 1 are smaller than those found for the reference material, due to the difference in the crack evolution law. Figure 21(c) shows the crack pattern for the simulation with material variation 2. The size of the damaged area here is a little larger than the reference. The increase in the stress level in the strain-hardening curve results in a larger crack opening at the bottom of the panel and smaller crack openings in the rest of the panel. Finally figure 21(d) shows the crack pattern for the panel employing material variation 3. Compared with the reference material parameters the tensile strength, $f_{t,SH,0}$, is increased from 1.7 MPa to 3.5 MPa. Due to this increase the size of the damaged area is considerably reduced. The crack openings in the damaged area are similar to those observed for variation 2, due to identical crack evolution laws and a similar stress level on the hardening branch.

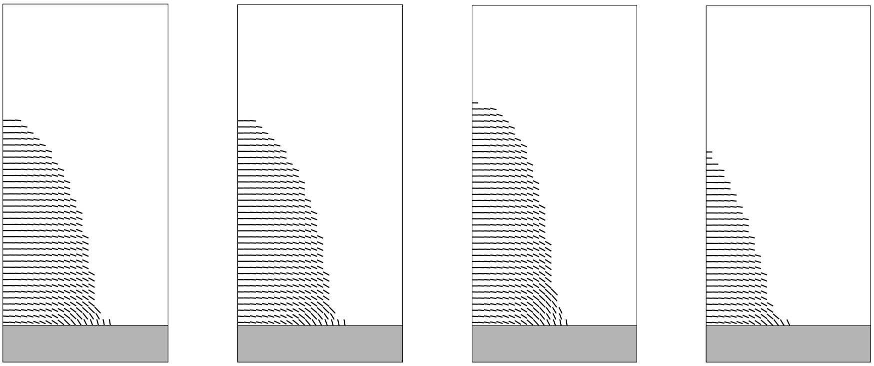
(a) Reference panel. (b) Variation 1. (c) Variation 2. (d) Variation 3.

Figure 21: Crack orientation in the simulations of the infill panels.

Figure 23 illustrates the normal stresses in the matrix and fibers as a function of the crack opening at points A and B respectively for the four simulations. Material variation 1 represents a material that has better fiber distribution than the reference material and thus more cracks within the same length. This results in less crack opening at point A and B (115 μm and 53 μm, respectively) compared with the simulation with the reference material (185 μm and 61 μ, respectively). A better distribution of fibers and therefore the appearance of more cracks, results in a larger strain capacity and less visible cracks. In variations 2 and 3, the impact of a fiber-volume ratio increase is modeled, which results in an increased stress level in the strain-hardening curve of the composite. The increased fiber volume ratio results in larger crack openings at point A, while the crack openings at point B are reduced by a factor of 2 compared with the results from the reference simulation. The crack openings are related to the strain level and the crack evolution law. The crack evolution laws are identical for the reference material and variation 2 and 3, but the higher stress level in the strain-hardening curve for the composite in variation 2 and 3, causes the crack to begin to localize at point A, resulting in a lower strain

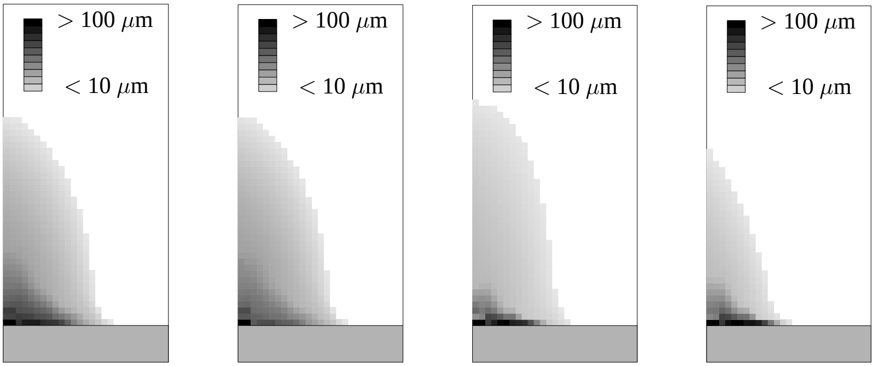

(a) Reference panel. (b) Variation 1. (c) Variation 2. (d) Variation 3.

Figure 22: Crack opening in the simulations of the infill panels.

and thereby crack opening at point B.

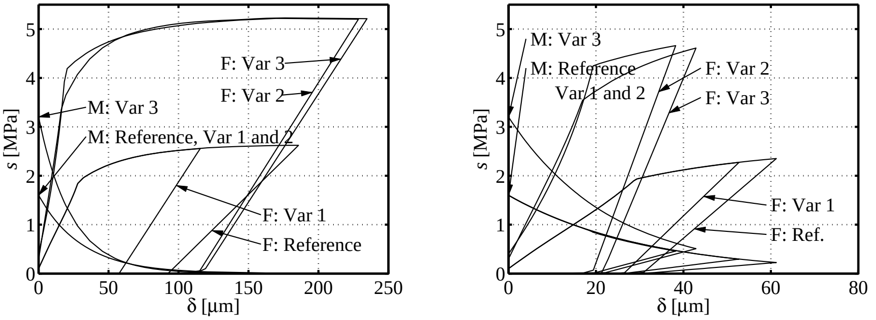

(a) Normal stresses at point A. (b) Normal stresses at point B.

Figure 23: Normal stresses in the matrix (M) and the fiber-bridging (F) stresses.

In figure 24, the average crack displacement associated with points A and B for the four simulations are shown, as a function of the displacement. In variation 1, the average crack distance is reduced from 58 mm to 34 mm at point A compared with the simulation for the reference material, and before unloading the number of cracks has not yet reached a constant level. This makes sense, because for a given normal strain the associated number of parallel cracks is highest for variation 1 (see figure 15(b)), and the normal strain at which localization occurs is twice as large in variation 1. In variation 2, the crack spacing is increased compared with the reference simulation. The reason for this is that the tensile strength, $f_{t,SH,0}$, is increased from 1.7 MPa to 2 MPa, which in turn increases the displacement, u, at which the first crack is initiated compared to the panel with the reference material parameters. At a displacement, u, of 0.62 mm, the number of cracks associated with one material point reaches a constant level at point A. In variation 3 the tensile strength, $f_{t,SH,0}$, is increased from 1.7 MPa to 3.5 MPa, which is why the first crack at point A is initiated at a displacement, u, of 0.22 mm compared to a displacement of 0.12 mm in the panel with the reference material parameters. The crack spacing reaches a level similar to that obtained for variation 2 and the reference case at a deformation, u, of 0.92 mm, due to identical crack evolution laws. Common for all the simulations is that the crack spacing has not yet become constant at point B before unloading, because the normal strain here is less than 0.22 % and 0.5 % for material variation 1, which is where the crack spacing spacing becomes constant (see figure 15(b)).

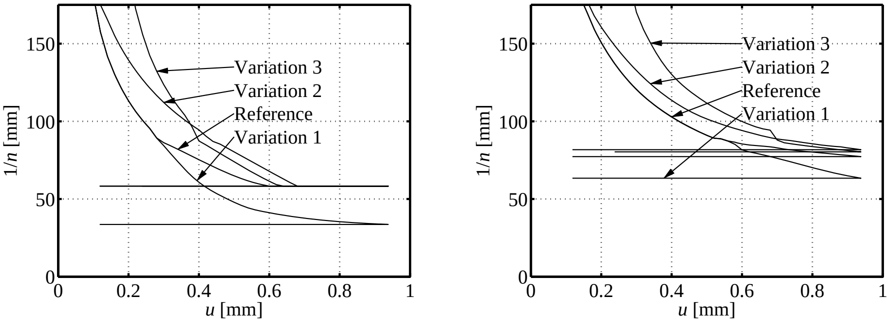

(a) Point A. (b) Point B.

Figure 24: Average displacement between cracks.

4 Conclusion

In Part I of this article a plasticity-based damage mechanics model was introduced. The model is characterized by the detailed information it can provide about crack openings and spacing. The model is meant as a tool for the design engineer to use in the design phase.

A demonstration of a plasticity-based damage mechanics model for Strain-Hardening Fiber-Reinforced Cementitious Composite (SHFRCC) has been performed by simulating the behavior of a four-point bending (FPB) beam and an precast infill panel both made of SHFRCC material.

The results obtained from the simulation of the FPB beam agree well with experimental results. In addition to global stresses and deformations, information about crack traction, opening, orientation and spacing was obtained. This simple example demonstrates the capability of the model.

In the simulation of the infill panel with the reference material parameters, good agreement between the simulation results and experimental observation was reached. A parameter study of the fiber and matrix properties showed that with relatively moderate changes it is possible to alter the crack pattern. Such changes are possible through altering the material mix design.

Thus this model could be used to assist in selecting a material (mix) design to achieve target cracking performance in a structure fabricated with SHFRCC material.

The present version of the model is limited to handling the initial crack system, where no cracks localize. Furthermore, the yield surface is not allowed to reestablish as the crack closes. This means that if a stress-free crack closes, then it is not able to transfer compression or friction stresses.

5 Acknowledgement

At special thanks to Cole Olsen from Stanford University for sharing his experimental results for the infill panel.

Notation

The following symbols are used in this paper:

E_0	E-modulus
E_{SH}	Strain-hardening modulus for the composite
F	Slope of the crack evolution law
$G_{F,I}$	Mode I fracture energy for the matrix
$G_{F,II}$	Mode II fracture energy for the matrix
b	Unloading constant
c_0	Cohesion in the matrix
e	Stiffness of crack
$f_{t,0}$	Tensile strength of the matrix
$f_{t,SH,0}$	Tensile strength of the composite
k	Spring stiffness
l	Side length of RVE
n	Number of cracks per length
$\boldsymbol{s}$	Local stress in a crack
t	Thickness
u	Displacement
$\boldsymbol{\delta}$	Crack opening
$\boldsymbol{\varepsilon}$	Strain
ε_t	Normal strain at first crack initiation
ε_u	Ultimate strain (before localization)
$\boldsymbol{\sigma}$	Stress
$\boldsymbol{\sigma}_u$	Ultimate stress
μ_0	Friction coefficients for the yield surface
μ_f	Friction coefficients for the yield surface
$\mu_{g,0}$	Friction coefficients for the plastic potential
ν	Poisson's ratio

References

Asferg, J. L., Poulsen, P. N. & Nielsen, L. O. (2007), ‘A direct XFEM formulation for modeling of cohesive crack growth in concrete’, *Computers and Concrete* **4**(2), 83–100.

Bazant, Z. P. & Oh, B. H. (1983), ‘Crack band theory for fracture of concrete’, *Materials and Structures* **16**(93), 155–177.

Belytschko, T. & Black, T. (1999), ‘Elastic crack growth in finite elements with minimal remeshing’, *International Journal for Numerical Methods in Engineering* **45**(5), 601–620.

Carol, I., Prat, P. C. & López, C. M. (1997), ‘Normal/shear cracking model: Application to discrete crack analysis’, *Journal of Engineering Mechanics* **123**(8), 765–773.

Dick-Nielsen, L., Poulsen, P. N., Stang, H. & Olesen, J. F. (2004), Semi-analytical cohesive crack model for the analysis of first crack strength of mortar, *in* A. Eriksson, J. Månsson & G. Tibert, eds, ‘Proc. of the 17^{th} Nordic Seminar on Computational Mechanics’, pp. 183–186.

Dick-Nielsen, L., Stang, H. & Poulsen, P. N. (2005), Micro-mechanical analysis of fiber reinforced cementitious composites using cohesive crack modeling, *in* O. M. Jensen, M. Geiker & H. Stang, eds, ‘Knud Hojgaard Conference on Advanced Cement-Based Materials’, pp. 277–292.

Dick-Nielsen, L., Stang, H. & Poulsen, P. N. (2006), Condition for strain-hardening in ECC uniaxial test specimen, *in* M. S. Konsta-Gdoutos, ed., ‘Measuring, Monitoring and Modeling Concrete Properties’, Springer, Alexandroupolis, Greece, pp. 41–47.

Fischer, G., Stang, H. & Dick-Nielsen, L. (2007), Initiation and development of cracking in ECC materials: Experimental observations and modeling, *in* G. F. A. Carpinteri, P. Gambarova & G. P. (eds), eds, ‘High Performance Concrete, Brick-Masonry and Environmental Aspects’, Vol. 3, Ia-FraMCos, Taylor & Francis, pp. 1517–1522.

Han, T. S., Feenstra, P. H. & Billington, S. L. (2003), ‘Simulation of highly ductile fiber-reinforced cement-based composite components under cyclic loading’, *ACI Structural Journal* **100**(6), 749–757.

Hillerborg, A., Modeer, M. & Petersson, P. E. (1976), ‘Analysis of crack formation and crack growth in concrete by means of fracture mechanics and finite elements’, *Cem. Concr. Res.* (6), 773–782.

Kabele, P. (2002), ‘Equivalent continuum model of multiple cracking’, *Engineering Mechanics (Association for Engineering Mechanics, Czech Republic)* **9 (1/2)**, 75–90.

Kachanov, L. M. (1958), ‘Time of the rupture process under creep conditions’, *Izvestija Akademii Nauk SSR, Otdelenie Techniceskich Nauk* **8**, 26–31.

Kesner, K. E. & Billington, S. L. (2005), ‘Investigation of infill panels made from engineered cementitious composites for seismic strengthening and retrofit’, *Journal of Structural Engineering - ASCE* **131**(11), 1712–1720.

Li, V. C. (2003), ‘On engineered cementitious composites (ECC) - a review of the material and its applications’, *Journal of Advanced Concrete Technology* **1**(3), 215–230.

Liao, W.-C., Chao, S.-H., Park, S.-Y. & Naaman, A. E. (2006), Self-consolidating high performance fiber reinforced concrete (SCHPFRC) - preliminary investigation, Cvis, 1576, 1057, Department of Civil and Environmental Engineering, University of Michigan, Ann Arbor, USA.

Lin, Z., Kanda, T. & Li, V. C. (1999), 'On interface property characterization and performance of fiber-reinforced cementitious composites', *Concrete Science and Engineering* **1**, 173–184.

Naaman, A. E. & Reinhardt, H. W. (1996), Characterization of high performance fiber reinforced cement composites, *in* A. Naaman & H. Reinhardt, eds, 'High Performance Fiber Reinforced Cement Composites 2 (HPFRCC 2)', The Second International RILEM Workshop, E and FN Spon, pp. 1–24.

Olsen, C. E. & Billington, S. L. (2007), Energy-absorbent infill panels for seismic retrofit of steel frame buildings using self-compacting, high-performance fiber-reinforced cementitious composites - phase 1: Single panel cyclic experiments, Technical Report 158, John E. Blume Center for Earthquake Engineering, Stanford University.

Østergaard, L., Walter, R. & Olesen, J. F. (2006), Method for determination of tensile properties for ECC II: Inverse analysis and experimental results, *in* G. Fisher & V. C. Li, eds, 'International Rilem Workshop on High Performance Fiber-Reinforced Cementitious Composites (HPFRCC) in Structural Applications', RILEM Publications S.A.R.L., pp. 57–64.

Rashid, Y. R. (1968), 'Ultimate strength analysis of prestressed concrete pressure vessels', *Nuclear Engineering and Design* **7**, 334–344.

SB (1994), 'Sb 1953 hospital facilities seismic safety Act, chapter 740, statues of 1994', *California Legislature* .

Stang, H. (1992), Evaluation of properties of cementitious fiber composite materials - In high performance fiber reinforced cement composites, *in* H. Reinhardt & A. Naaman, eds, 'High Performance Fiber Reinforced Cement Composites', The International RILEM/ACI Workshop, E and FN Spon, pp. 388–406.

Stang, H., Olesen, J. F., Poulsen, P. N. & Dick-Nielsen, L. (2007), 'On the application of cohesive crack modeling in cementitious materials', *Materials and Structures* **40**, 365–374.

Walter, R., Olesen, J. F., Stang, H. & Vejrum, T. (2007), 'Analysis of an orthotropic deck stiffened with a cement-based overlay', *Journal of Bridge Engineering* **12**(3), 350–363.

Report no BYG R-169
ISSN 1601-2917
ISBN 978-87-7877-243-5